

**UNIVERSITÄT
BAYREUTH**

Lehrstuhl für Kristallographie

Synthesis, Superstructure, Vacancy-Ordering of Intercalated Transition Metal Dichalcogenides

Von der Universität Bayreuth
zur Erlangung des akademischen Grades eines
Doktors der Naturwissenschaften (Dr. rer. nat.)
genehmigte Abhandlung

vorgelegt von
Sk Imran Ali
aus Kolaghat, Indien

1. Gutachter: Prof. dr. Sander van Smaalen
2. Gutachter: Prof. Dr. Hans F. Braun

Tag der Einreichung: 09. 07. 2014
Tag des Kolloquiums: 28. 10. 2014

Dedicated To...

*My beloved Family, Teachers and some
exceptional persons whom I Admire.*

Contents

1	Introduction	1
2	Transition metal dichalcogenides (TMDCs) and their intercalation	5
2.1	Transition metal dichalcogenides (TMDCs)	5
2.2	Intercalated transition metal dichalcogenides	8
2.3	Superstructures and vacancy ordering	15
3	Experimental methods and techniques	23
3.1	Synthesis of TMDCs and their intercalated compounds	23
3.1.1	Preparation of polycrystalline samples	23
3.1.2	Chemical vapor transport method	23
3.2	Single-crystal X-ray diffraction	27
3.2.1	Experiments on a MAR345 dtb and Mach3 diffractometer	28
3.2.2	Experiments at Synchrotron center using CCD detector	31
3.2.3	Data collection strategy at D3 and F1	33
3.3	Bond valence sum method	34
4	Self intercalation and vacancy ordering in $6\text{R-Cu}_x\text{Ta}_{1+y}\text{S}_2$ ($x \approx 0.23$, $y = 0, 0.06$)	37
4.1	Abstract	37
4.2	Introduction	38
4.3	Experimental	39
4.3.1	Synthesis	39
4.3.2	X-ray diffraction	39
4.3.3	Crystal structure refinements	43
4.4	Discussion	45
4.5	Conclusions	52

5	Synthesis, Superstructure and Vacancy-Ordering in 2H-Cu_xTa_{1+y}Se₂ (MoS₂-type and NbS₂-type)	55
5.1	Abstract	55
5.2	Introduction	56
5.3	Experimental	57
5.3.1	Synthesis and crystal growth	57
5.3.2	X-ray diffraction	58
5.3.3	Crystal structure of crystal A of batch I	59
5.3.4	Crystal structure of crystal B of batch II	62
5.4	Discussion	63
5.5	Conclusions	67
6	Synthesis, single crystal X-ray structure of Cu₃TaSe₄ and comparative studies with other Cu₃MX₄ (M = V, Nb, Ta; X = S, Se, Te)	69
6.1	Abstract	69
6.2	Introduction	70
6.3	Experimental Section	71
6.3.1	Preparation of polycrystalline sample	71
6.3.2	Crystal growth	71
6.3.3	X-ray diffraction experiment	72
6.4	Results and discussion	72
6.5	Conclusion	77
7	Summary	79
8	Zusammenfassung	81
A	Supplementary materials: 6R-Cu_xTa_{1+y}S₂	83
B	Supplementary materials: 2H-Cu_{0.52}TaSe₂ and 2H-Cu_{0.16}Ta_{1.08}Se₂	91
C	Supplementary materials: Cu₃MX₄	95
	Bibliography	99
	Acknowledgements	109

CONTENTS

v

Erklärung

111

Chapter 1

Introduction

Materials with layered structures remain an extensively investigated topic in the field of physics and chemistry. Graphite and their intercalated compounds have been known for a long time whereas transition metal dichalcogenides (TMDCs) and their intercalated compounds have attracted interest for the past several decades due to their low-dimensional electronic properties leading to the development of charge density waves (CDW), superconductivity and many other physical properties such as electrical resistivity, thermal expansion and optical properties (Monceau (2012); Wilson et al. (1975)). Different kinds of polytypes have been found for TMDCs and their intercalated compounds (Bjerkelund and Kjekshus (1967); Bohnen (1995)). Although different types of synthetic procedures, such as atom deposition in ultra high vacuum (UHV), sintering, electrochemical intercalation and chemical vapor transport (CVT) method, are known for these compounds, the CVT method is the best method for producing single crystals (Binnewies et al. (2012)).

In the CVT method, the process of crystal growth occurs through chemical reactions in which polycrystalline solid reacts with a transporting agent, like iodine, bromine or chlorine, at the source zone to form vapor-phase products. A temperature gradient is maintained in a two-zone furnace for the transport of material from the source zone to the growth zone of the ampoule, where the gaseous compound decomposes and crystals grow. The temperature of the source and growth zones depend on the thermodynamics of the chemical reactions. Crystal growth of sulfides and selenides of binary and ternary compounds has been done using this method for last few decades (Binnewies et al. (2013)). The CVT method allows the direct growth of bulk crystals of intercalated compounds, by the choice of an appropriate composition of the source material. However, it is difficult to synthesize a single

polytype, because of the close proximity of the free energies of the polytypes. It occurs very often that different polytypes are found in one batch of synthesized products.

Superstructures may be found as the result of partial ordering of the intercalated atoms over the available sites within the Van der Waals gaps ("vacancy ordering") and distortions of the structures. The appearance of superlattice or satellite reflections in X-ray diffraction indicates the existence of superstructures. Chemical compositions can be determined by electron microprobe (EMP) experiments. The physical and chemical properties of the intercalated compounds may differ from the host compound (TMDCs), depending on the nature and amount of guest species. Low-temperature studies as well as temperature-dependent studies are useful for these types of compounds to find out possible charge density wave (CDW) phase transitions and other properties. The goal of this thesis is to obtain optimal conditions for the synthesis of different phases of intercalated transition metal dichalcogenides, specifically for the copper intercalated TMDCs and then structural studies to find out the existence of superstructures, vacancy-ordering and CDW phase transitions at low temperatures.

Chapter 2 of this thesis is focussed on the fundamentals of transition metal dichalcogenides (TMDCs) and their intercalated compounds. Structures, examples and schematic diagrams of different types of polytypes for both TMDCs and intercalated TMDCs are presented in this chapter. The mechanisms of the formation of intercalated compounds and formation of superstructures are also discussed. The phase diagram of TaSe₂, including reaction conditions and lattice parameters of different polytypes as well as their intercalated compounds is presented.

Chapter 3 is focussed on the experimental methods and techniques, that I have used for the synthesis and characterization. A brief overview of synthesis of TMDCs and their intercalated compounds and mechanism of the chemical vapor transport method are presented. Then methodological aspects of single-crystal X-ray experiments are discussed. Different types of X-ray sources, experimental setup and data collection strategy are discussed. The bond valence sum (BVS) method is discussed briefly.

In Chapter 4, the eightfold ($2a_0 \times 2b_0 \times 2c_0$) superstructures of 6R-Cu_xTa_{1+y}S₂ ($x \approx 0.23$, $y = 0, 0.06$) are presented. The superstructure is found to be the result of vacancy ordering within the Van der Waals gaps. No CDW phase transition has been found from the temperature-dependent studies down to a temperature of 14K.

In Chapter 5, synthesis, superstructure and vacancy-ordering of 2H-Cu_xTa_{1+y}Se₂

are discussed. Chemical vapor transport (CVT) has been employed to grow single crystals of 2H-Cu_xTa_{1+y}Se₂ for $(x, y) = (0.52, 0)$ and $(0.16, 0.08)$. A fourfold ($2a_0 \times 2b_0 \times c_0$) superstructure has been found for 2H-Cu_{0.52}TaSe₂, as the result of vacancy ordering in the intercalated plane within the Van der Waals gaps, whereas 2H-Cu_{0.16}Ta_{1.08}Se₂ does not form a superstructure.

Chapter 6 describes the synthesis and single-crystal X-ray diffraction study of Cu₃TaSe₄ and further comparative studies with other Cu₃MX₄ (M = V, Nb, Ta; X = S, Se, Te) compounds. Cubic-shaped, orange-yellow-colored single-crystalline Cu₃TaSe₄ was found from synthesis and single-crystal X-ray diffraction study is done for the first time. Anisotropic ADPs refinement in our studies shows better description of structure model. Computed valences of atoms in Cu₃MX₄ using bond valence sum (BVS) method are in good agreement with formal valences with slightly over-bonded and under-bonded of the atoms.

Chapter 2

Transition metal dichalcogenides (TMDCs) and their intercalation

2.1 Transition metal dichalcogenides (TMDCs)

Transition metal dichalcogenides, in short TMDCs [MX_2 , M=transition metal of the groups IVb, Vb, VIb and X=chalcogen], are of considerable interest due to their exotic electronic states, like charge-density waves (CDWs) and superconductivity (Li et al. (2013); Mulazzi et al. (2010); Sipos et al. (2008); Castro Neto (2001); Du et al. (2000); Wilson et al. (1975)). TMDCs possess layered structures. The layers consist of two close-packed chalcogen planes between which reside the metal ions. Metal ions can be found in sites of trigonal prismatic or octahedral coordination by six chalcogen atoms (Fig 2.1). The preferred coordination is determined by the ionicity of the metal chalcogen bond. Octahedral coordination (ZrS_2 , ReS_2) is preferred in case of more ionic bonding since it maximizes the distances between negatively charged chalcogens. On the other hand trigonal prismatic (MoS_2 , NbS_2) coordination is preferred in case of covalent bonding (Kertesz and Hoffmann (1984)). The TMDC layers are connected to each other by weak interlayer bonding. These weak interactions are denoted as van der Waals interactions. Due to these weak interlayer interactions different types of slab stacking have been found and as a result of that polytypes and polymorphs are generated (Katzke et al. (2004)). Examples of polytypes found for TMDCs are shown in Table 2.1. The unit cells of TMDCs are defined with the c-axis perpendicular to the layers, and the a and b axes along the minimal chalcogen-chalcogen distance. The stacking sequence of these type of compounds is denoted by letters related to the notation of close-packed structures

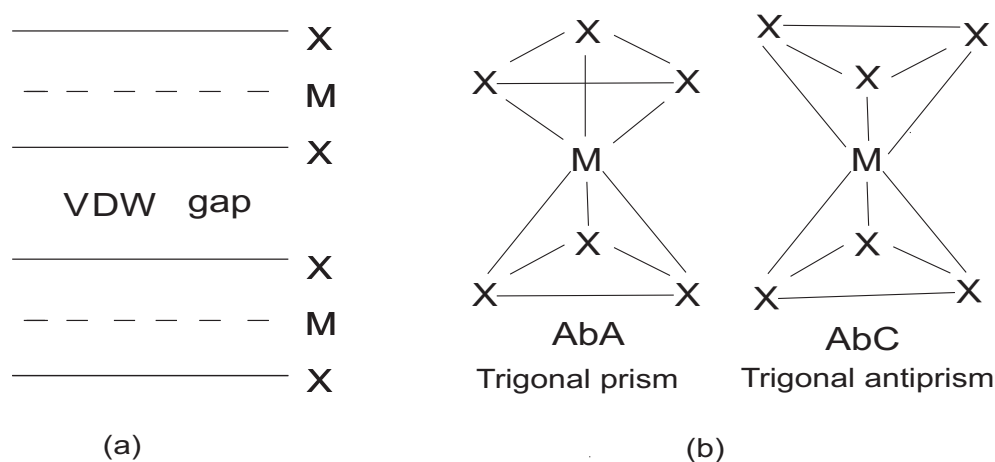


Figure 2.1: (a) The sandwich-like structure of layered chalcogenides. [VDW gap stands for van der Waals gap] (b) The two coordination polyhedrons for the transition metal in layered chalcogenides. [A and C stands for the chalcogen plane and b for the transition metal plane.

(Pandey and Krishna (2006); Verma and Krishna (1966)). Capital letters A, B, C denote the chalcogen atom planes; small letters a, b and c denote transition metals (Whittingham and Jacobson (1982)). According to this notation AbA indicates trigonal prismatic coordination, while AbC indicates octahedral coordination (Fig 2.1). The formation of various types of stacking polytypes is discussed in the following paragraphs.

A rational way of nomenclature is considered to identify different types of polytypes and polymorphs (Brown and Beerntsen (1965)). It uses a number and letters. The number indicates how many layers are included in the conventional unit cell and the capital letter indicates the point symmetry. Small letter next to capital letter distinguishes between different polytypes with the same lattice. For example, 1T-TaSe₂ has trigonal symmetry with one layer in the unit cell. 2H-TaSe₂ represents hexagonal symmetry with two layers in one unit cell. Similarly, 3R-TaS₂ represents rhombohedral symmetry with three layers in the hexagonal unit cell.

Stacking sequences of different phases can be obtained by constructing the possible combinations of layers. For a compound with one layer per unit cell, one type of stacking sequence is possible i.e., AbC for octahedral coordination. Compounds with two layers per unit cell with trigonal prismatic coordination of transition metal can have the following stacking sequences: (1) AcA BcB, (2) AbA BaB, (3) AbA

Table 2.1: Examples of different polytypes found in TMDCs, Oh = Octahedral; TP = Trigonal prismatic; (Brown and Beerntsen (1965); Kalikhman and Umanskii (1973))

Phase	Space group	metal coordination	Stacking sequence	structure type
1T	P-3m1	Oh	AbC	1T-TaSe ₂
2H _a	P6 ₃ /mmc	TP	BcB AcA	2H-NbS ₂
2H _b	P-6m2	TP	BcB AbA	2H _b -Nb _{1+x} Se ₂
2H _c	P6 ₃ /mmc	TP	BaB AbA	2H-MoS ₂
3R	R3m	TP	BcB CaC AbA	3R-MoS ₂
4H	P-6m2	TP	BcB AcA BcB CaC	4H _a -TaS ₂
4H _b	P6 ₃ /mmc	Oh & TP	BcB CaB CaC BaC	4H _b -TaS ₂
4H _c	P6 ₃ mc	TP	BcB AcA BaB CaC	4H _c -TaS ₂
6R	R3m	Oh & TP	BcB CaB CaC AbC AbA BcA	6R-TaS ₂
6H	P6 ₃ /mmc	Oh & TP	AbA CbC BcB AcA CaC BaB	6H-Ta _{1+x} S ₂

BcB. Type 1 is the NbS₂ type of structure with equal cationic environments in both layers. Type 2 is the MoS₂ type of structure, also with equal cationic environments in each layer (Jellinek et al. (1960)). Type 3 is the combination of type 1 and type 2 structure types, resulting in coordinations of the metal ions that differ from each other in the second coordination sphere (Fig 2.2) (Brown and Beerntsen (1965)). In some cases mixed stacking sequences may stabilize the structure by lowering the symmetry with respect to the symmetry in the pure state. The lowering of symmetry may happen to allow distortions which results in the formation of superstructure.

In a similar way one can find two different polytypes for the 3R phase having trigonal prismatic coordination of transition metal. The three layers in the 3R phase are generated from one layer due to centering translations of the rhombohedral symmetry. The two possible stacking sequences for the 3R phase are AbA BcB CaC and AcA BaB CbC. In general, with the increase of the number of layers in the unit cell, the number of different stacking sequences increases. This type of layer construction is satisfactory when number of layers are few. It becomes complex and prone towards stacking faults when number of possibilities increases.

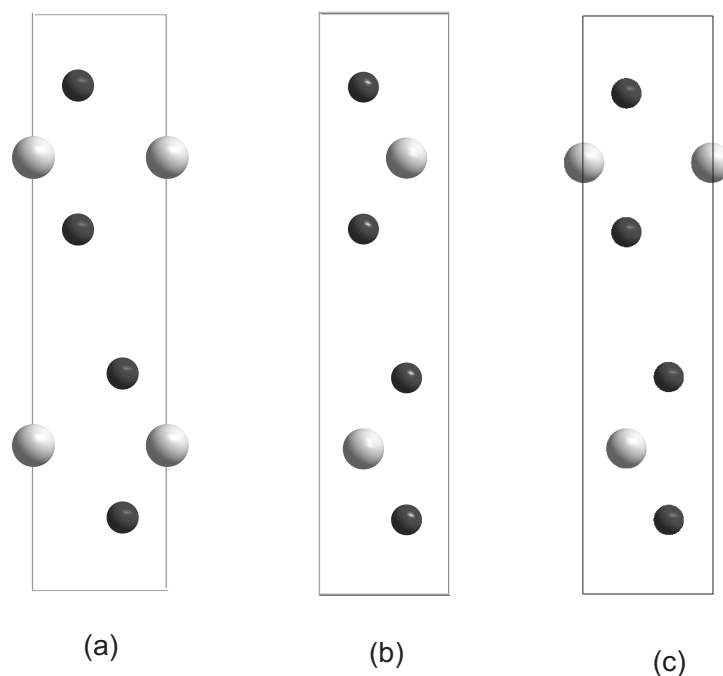


Figure 2.2: Different types of polymorphs of the 2H phase. Stacking sequences: (a) AcA BcB, (b) AbA BaB, (c) AbA BcB; Grey large circles stand for transition metal and black small circles indicate chalcogen atoms. Projections of the structures are given along \mathbf{b}^* .

2.2 Intercalated transition metal dichalcogenides

Intercalated transition metal dichalcogenide (TMDC) compounds are intensively studied due to their interesting physical and chemical properties and also their potential applications (Moroson et al. (2006); Yoffe (1990); Inoue et al. (1989); Wieggers (1980); Friend and Yoffe (1987)). The layered TMDCs structures allow the intercalation of molecules and atoms or ions into the Van der Waals gaps between the layers (Crawack and Pettenkofer (2001); Ali et al. (2012); Figueroa et al. (1996); Pervov et al. (1996); Whittingham (1978); Yang et al. (1999)). Compositions of intercalants may vary between zero to a maximum filling of one and give rise to stoichiometric or nonstoichiometric compounds. Preferred locations for the intercalated atoms are the octahedral sites which are the largest void and tetrahedral sites which are the second largest void in the Van der Waals gaps. The sizes of the octahedral and tetrahedral sites depends on the nature of layers MX_2 and the interactions between

Table 2.2: An overview of intercalated $\text{Cu}_x\text{Ta}_{1+y}\text{S}_2$ compounds of different compositions

Phase	Homogeneity range	Lattice parameters (Å)	Space group	References
1T-TaS ₂	$x = 0$	$a = 3.365, c = 5.897$	$P\bar{3}m1$	Spijkerman et al. (1997)
1T-Cu _x TaS ₂	$x \approx 0.01$	$a = 3.365, c = 5.898$	$P\bar{3}m1$	Bohnen (1995)
2H-Cu _x TaS ₂ (NbS ₂ type)	$0.01 < x < 0.20$	When $x = 0.11,$ $a = 3.316, c = 12.143$	$P6_3/mmc$	Wagner et al. (2008)
6R-Cu _x TaS ₂	$0.21 < x < 0.24$	When $x = 0.23,$ $a = 3.322, c = 37.557$	$R\bar{3}m$	Bohnen (1995)
2H-Cu _x TaS ₂ (MoS ₂ type)	$0.28 \leq x \leq 0.67$	When $x = 0.67,$ $a = 3.34, c = 13.14$	$P6_3/mmc$	Ali et al. (2012)
3R-Ta _{1+y} S ₂	$x = 0, y = 0.08$	$a = 3.317, c = 18.014$	$R3m$	Bohnen (1995)
2T-Cu _x Ta _{1+y} S ₂	$x \approx 0.11$ $y \approx 0.08$	$a = 3.319, c = 12.308$	$P3m1$	Gotoh et al. (1998)
9R-Cu _x Ta _{1+y} S ₂	$x \approx 0.16$ $y \approx 0.04$	$a = 3.319, c = 55.132$	$R3m$	Bohnen (1995)
4H _a -Cu _x Ta _{1+y} S ₂	$0.19 \leq x < 0.30$ $0.08 \leq y \leq 0.10$	$a = 3.317, c = 24.885$	$P6_3mc$	Bohnen (1995)
6H-Cu _x Ta _{1+y} S ₂	$0.14 \leq x \leq 0.20$ $0.10 \leq y \leq 0.15$	When $x = 0.16, y = 0.10$ $a = 3.318, c = 36.878$	$P6_3/mmc$	Bohnen (1995)
6R-Cu _x Ta _{1+y} S ₂	$0.14 \leq x \leq 0.35$ $0.18 \leq y \leq 0.20$	When $x = 0.26, y = 0.19$ $a = 3.304, c = 38.495$	$R\bar{3}m$	Harbrecht and Kreiner (1989)

them. An overview of copper-intercalated TaS₂ compounds is given in the Table 2.2. Depending on the nature and amount of guest species, the physical and chemical properties of the intercalated compounds generally differ from those of the host compound. With the increase of the the concentration of the guest species the interlayer gaps increases accordingly which is observed by diffraction techniques. However in some cases of rhombohedral symmetry, a decrement of the c axis is found with increasing amount of intercalants.

Homogeneity ranges of self intercalated Ta_{1+x}Se₂ compound of different phases have been shown by Bjerkelund and Kjekshus (Bjerkelund and Kjekshus (1967)). The concentration dependencies of the unit cell parameters for 2H and 3R phase are presented in the Table 2.3. The changes of $a(=b)$ are not significant for both phases, whereas increment of c axis have been found for 2H phase and decrement for 3R phase with the increase of concentration of intercalant. There are several methods to

Table 2.3: Unit cell dimension of the Ta_{1+x}Se₂ phase at room temperature (Bjerkelund and Kjekshus (1967))

Polytype	Chemical formula	a (Å)	c (Å)	V (Å ³)
3R	TaSe ₂	3.428	19.100	194.37
2H _b	TaSe ₂	3.431	12.737	129.85
3R	Ta _{1.03} Se ₂	3.437	19.05	194.88
	Ta _{1.11} Se ₂	3.442	18.98	194.69
	Ta _{1.14} Se ₂	3.443	18.93	194.24
	Ta _{1.18} Se ₂	3.444	18.91	194.18
	Ta _{1.21} Se ₂	3.444	18.88	193.98
2H _b	Ta _{1.33} Se ₂	3.434	12.87	131.46
	Ta _{1.38} Se ₂	3.433	12.89	131.52
	Ta _{1.43} Se ₂	3.432	12.92	131.71
	Ta _{1.54} Se ₂	3.429	12.97	132.04
	Ta _{1.60} Se ₂	3.430	13.00	132.41

prepare intercalated TX₂ compounds, such as ultra high vacuum methods (UHV), electrochemical methods, sintering methods and chemical vapor transport (CVT) method. However, chemical vapor transport (CVT) method is the best method for synthesizing and growing single crystals of pure intercalated compounds. In this method, intercalation happens in the bulk phase of the compound. It may be possi-

ble to get different phases from one batch of synthesis. This is probably due to the close structural relationship between the polytypes of intercalated MX_2 . Different kinds of polytypes have been found with the change of reaction conditions (reaction temperature, reaction time, temperature gradient) and compositions (Figure 2.3). An overview of the copper-intercalated TaS_2 system has been given by Bohnen (1995) (See Table 2.2 and Fig. 2.3). Schematic diagram of different polymorphs of intercalated compounds is shown in Figure 2.4. Literature review of different phases of intercalated TaSe_2 have been presented in Table 2.4, 2.5, 2.6, 2.7, 2.8, 2.9.

If x mol of G is intercalated in 1 mol MX_2 the reaction can be written as:



Where G stands for the guest species. If intercalation does occur, one might expect at first that the van der Waals gap region will fill uniformly with intercalants up-to maximum mole fractions. However, this is not always the case and at this point the phenomenon of staging may appear. The maximum stoichiometry achievable for guest atom is $x = 1.0$ in the $G_x\text{MX}_2$ compound. x varies from zero to one, depending on the size of the octahedral and tetrahedral site and the intercalant size. Depending on the insertion of the guest atoms into the Van der Waals gap different staging of intercalated compounds are possible even though both host and guest atoms are same (Figure 2.5). In stage 1 compounds, host layers and guest layers alternate and in stage 2 compounds, two consecutive host layers with no guest material in between alternate with one guest layer. In stage 3 compounds, three consecutive host layers with no guest material in between alternate with a guest layer and in stage 4 compounds, four consecutive host layers with no guest material in between alternate with a guest layer. The mechanism of the formation of intercalated compounds and different types of staging are illustrated in the Figure 2.5. From the above discussions, we can say stage 2, stage 3 and stage 4 compounds have half, one-third and one-fourth times of intercalated atoms with respect to stage 1. Potassium intercalated graphite KC_8 , KC_{24} , KC_{36} and KC_{48} show stage 1, stage 2, stage 3 and stage 4 type respectively (Böhm et al. (1996); Mori et al. (1983)). In an another example lithium intercalated graphite C_6Li and C_{12}Li also show stage 1 and stage 2 type of staging (Henderson and White (2011)). Thus, depending on the concentration of the intercalants different types of staging may arise as discussed. With the lowering of concentration of potassium and lithium the staging of intercalated graphite increases.

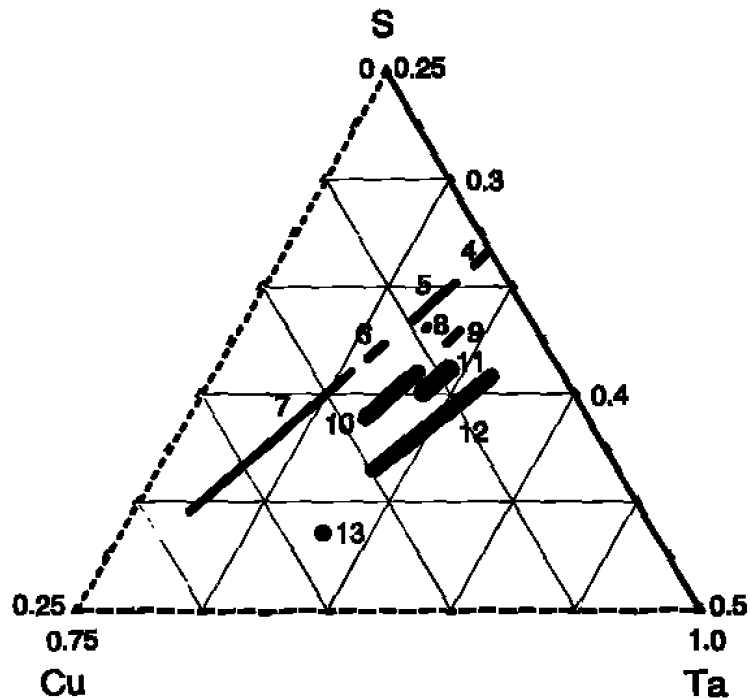


Figure 2.3: Phase diagram of the Cu-Ta-S system according to Bohnen (1995). A triangular section of the complete phase diagram of the Cu-Ta-S system is shown here. The composition $\text{Cu}_u\text{Ta}_t\text{S}_s$ on the axis marked "S-Cu" has $t = 0.25$ with the numbers providing the fraction u of Cu, and with $s = 1-t-u$. The axis marked "Cu-Ta" has $s = 0.5$ with the numbers providing $(1-u)$. The axis "Ta-S" represents $u = 0$ with the numbers providing t as well as $(1-s)$. The points and lines correspond to the following compositions: 4. $1\text{T-Cu}_x\text{TaS}_2$, 5. $2\text{H-Cu}_x\text{TaS}_2$ (NbS_2 type), 6. $6\text{R-Cu}_x\text{TaS}_2$, 7. $2\text{H-Cu}_x\text{TaS}_2$ (MoS_2 type) 8. $9\text{R-Cu}_x\text{TaS}_2$, 9. $2\text{T-Cu}_{0.11}\text{Ta}_{1.08}\text{S}_2$, 10. $4\text{H-Cu}_x\text{Ta}_{1+y}\text{S}_2$, 11. $6\text{H-Cu}_x\text{Ta}_{1+y}\text{S}_2$, 12. $6\text{R-Cu}_x\text{Ta}_{1+y}\text{S}_2$, 13. $\text{Cu}_2\text{Ta}_5\text{S}_8$, "Cu:" $\text{Cu}_{0.25}\text{Ta}_{0.25}\text{S}_{0.5}$, "Ta:" $\text{Ta}_{0.5}\text{S}_{0.5}$, and "S:" $\text{Ta}_{0.25}\text{S}_{0.75}$. Figure reproduced from Fig. 4.1 of Bohnen (1995).

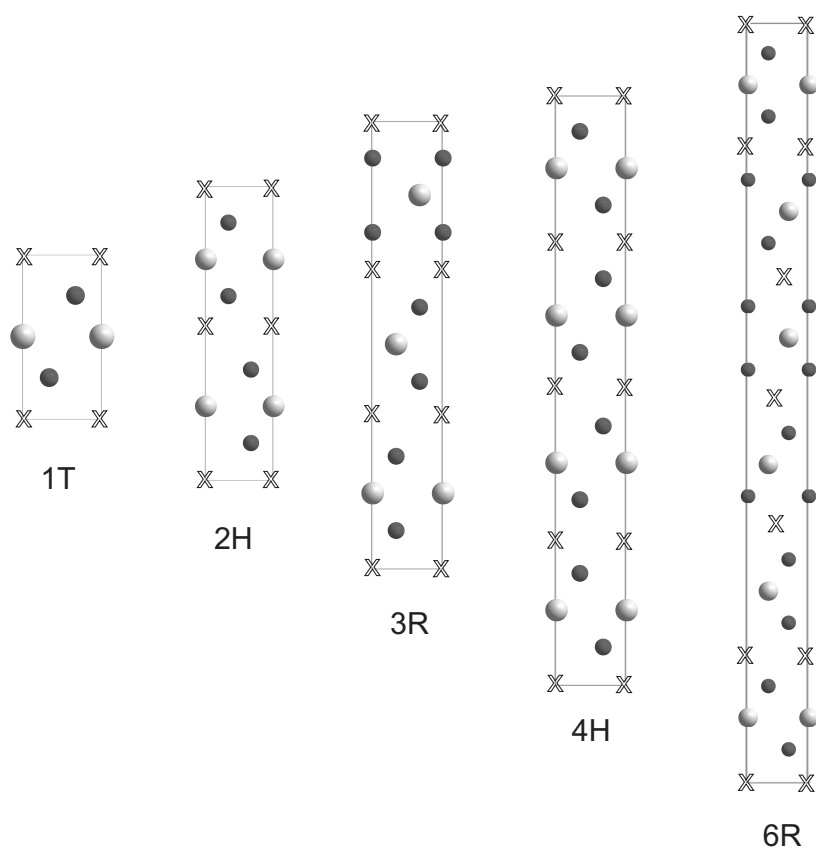


Figure 2.4: Schematic diagram of different polymorphs of TMDCs. Black small ball represents chalcogen atoms, Grey large ball represent transition metal and crosses represent positions where intercalants or guest atom can be found.

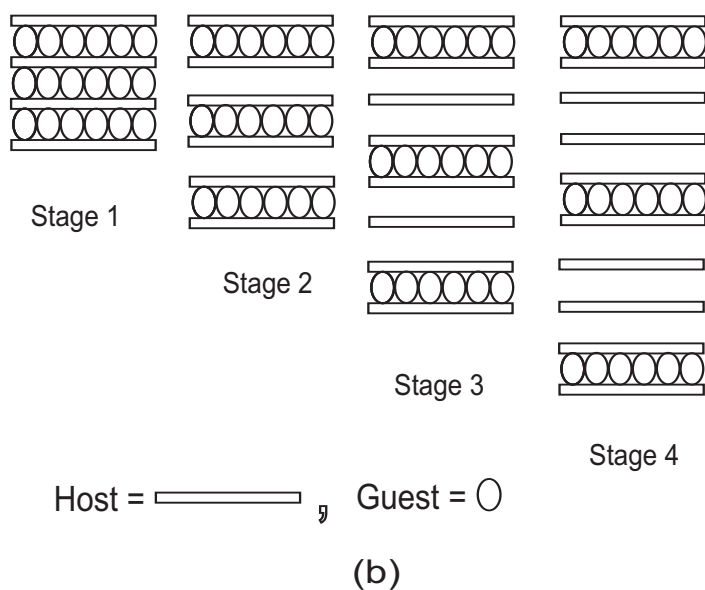
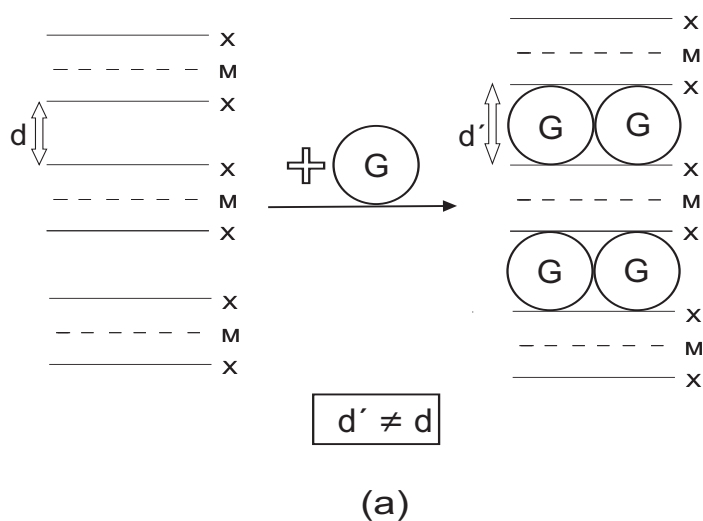


Figure 2.5: (a) Illustration of the mechanism of formation of layered intercalation compounds. (b) Schematic diagram of different types of staging of intercalated system

2.3 Superstructures and vacancy ordering

Many of the TMDCs and their intercalated compounds are known for exhibiting phase transitions associated with superlattice formation (Wilson et al. (1975)). Formation of the superstructures is the indication of the ordering of some ions or atoms in the lattice. Ordering is very much associated with the heat effects in the lattice. Two types of superstructures may arise due to the structural changes at different temperatures. One is commensurately multiple with the basic lattice and another one is incommensurately modulated, where the superlattice does not possess the same periodicity as basic lattice (van Smaalen (2007)). The extent of commensurability and incommensurability of a lattice can be determined by temperature-dependent studies using different types of diffraction techniques. Displacements of atoms can happen as a result of superstructure formation, however, such displacements are generally small, only a few percent of interatomic distances. Metastable MoS₂ forms twofold ($2a_0 \times b_0 \times c_0$) and fourfold ($2a_0 \times 2b_0 \times c_0$) superstructures due to the distortions in the MoS₆ octahedral units (Benavente et al. (2002)). Nearly commensurate (NC) 39-fold superstructure ($\sqrt{13}a_0 \times \sqrt{13}b_0 \times 3c_0$) has been found for 1T-TaS₂ at 300K (Spijkerman et al. (1997)). A commensurate 13-fold ($\sqrt{13}a_0 \times \sqrt{13}b_0 \times c_0$) superstructure for 4H_b-TaSe₂ was found at 75K to 410K and incommensurate superstructure at 410K to 600K (Lüdecke et al. (1999); Wilson et al. (1975)). These superstructures are the result of the strong modulation of Ta atoms and Se atoms in the TaSe₂ layers. In another example ordering or vacancy ordering of intercalants (Co) have been found for the threefold ($\sqrt{3}a_0 \times \sqrt{3}b_0 \times c_0$) superstructure of 2H-Co_{*x*}NbS₂ ($x = 1/3$) (Nakayama et al. (2006)). Similarly, 2H-Pb_{*x*}TaS₂ and 2H-Sn_{*x*}NbS₂ ($x = 1/3$) also show threefold ($\sqrt{3}a_0 \times \sqrt{3}b_0 \times c_0$) superstructure as a result of ordering or vacancy ordering in the intercalated plane (Fang et al. (1996)). Intercalated atoms occupy one-third of the octahedral sites between the TaS₂ and NbS₂ sandwiches in the Van der Waals gap. 2H-Fe_{*x*}TaS₂ ($x = 1/4$) shows fourfold ($2a_0 \times 2b_0 \times c_0$) superstructures and half of the octahedral sites are partially occupied by the Fe atoms in the van der Waals gap (Morosan et al. (2007)). Figure 2.6 shows how ordering or vacancy ordering affect the intercalated plane for the formation of superstructure from basic structure. An incommensurate superstructure has also been found due to the ordering of Ag ion in 2H-Ag_{0.6}NbS₂ below $T_c = 124$ K (van der Lee et al. (1991)).

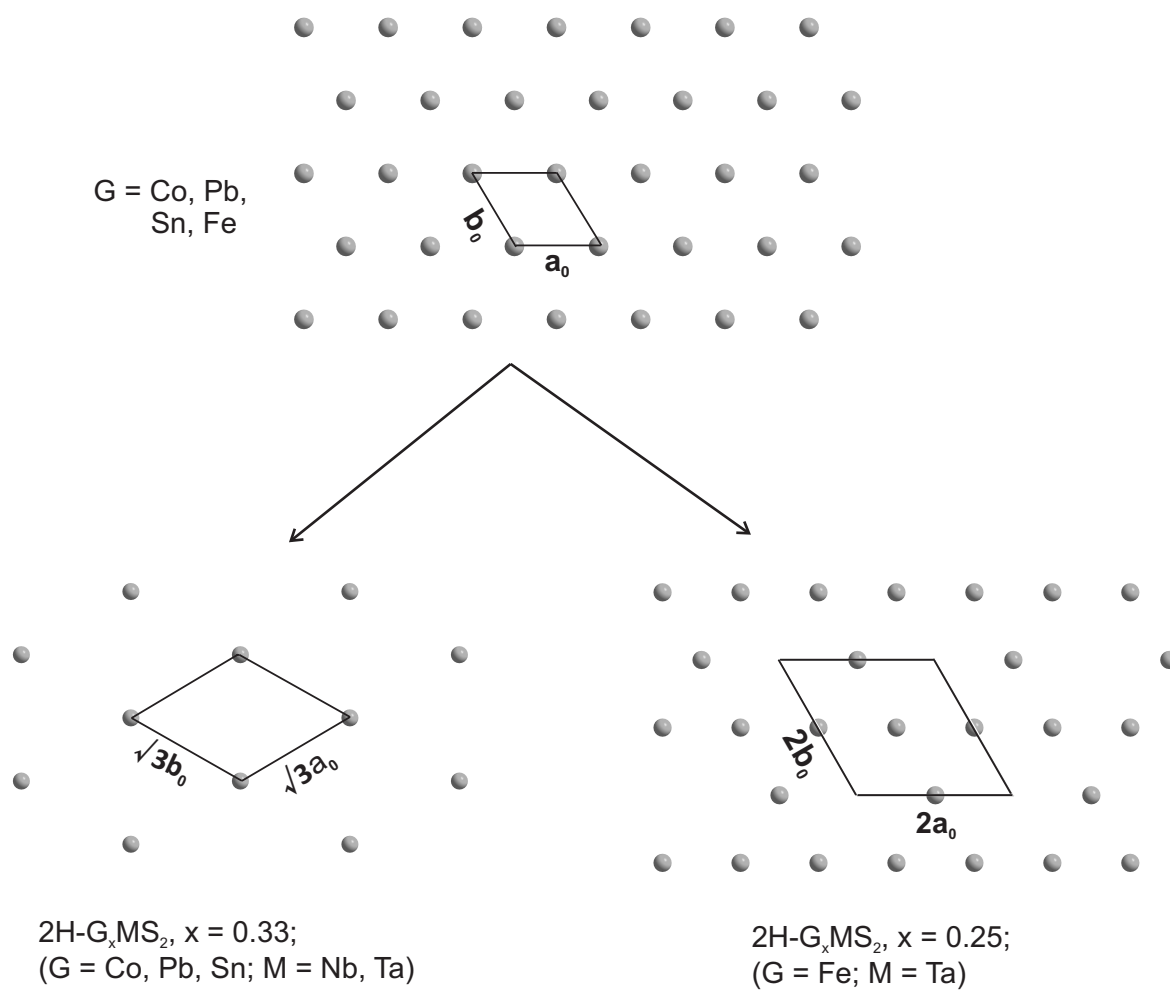


Figure 2.6: Vacancy ordering in the intercalated plane between MS₂ layers in 2H-G_xMS₂ superstructures. [References of the intercalated compounds are following: 2H-Co_{0.33}NbS₂ (Nakayama et al. (2006)); 2H-Pb_{0.33}TaS₂ and 2H-Sn_{0.33}NbS₂ (Fang et al. (1996)); 2H-Fe_xTaS₂ (Morosan et al. (2007))]

Table 2.4: 1T-TaSe₂ and its intercalated compounds

Compound	Lattice parameters(Å)	Reaction temperatures for synthesis and notes	References
1T-TaSe ₂	$a = 3.4769$ $c = 6.2722$	a. 900°C for 14 days b. reannealed between 200°C and 900°C	Bjerkelund and Kjekshus (1967)
1T-TaSe ₂	$a = 3.48$ $c = 6.27$	a. 950°C b. 950°C / 1025°C	Salvo et al. (1974)
1T-TaSe ₂	$a = 3.478$ $c = 6.263$	950°C / 1040°C	Brouwer and Jellinek (1980)
1T-TaSe ₂	$a = 3.4733$ $c = 6.2715$	950°C / 1040°C	Wiegiers et al. (2001)
1T-ATaSe ₂ (A = Li, Na, Cs)		UHV method "A" deposited on (0001) surface of 1T-TaSe ₂	Tonti et al. (1998)
1T-ATaSe ₂ (A = Li, Cu, Cs)		"A" deposited on (0001) surface of 1T-TaSe ₂	Crawack and Pettenkofer (2001)
1T-RbTaSe ₂		Rb deposited on (0001) surface of 1T-TaSe ₂	Stoltz et al. (2003)
1T-CuTaSe ₂		Cu deposited on (0001) surface of 1T-TaSe ₂	Gunst et al. (2000)

Table 2.5: 2H-TaSe₂ and its intercalated compounds

Compound	Lattice parameters(Å)	Reaction temperatures for synthesis and notes	References
2H-TaSe ₂	a = 3.437 c=12.72	900°C - 1200°C	Kadijk et al. (1964)
2H-TaSe ₂ (NbS ₂ -type)	a=3.436 c=12.696	a. 900°C for 14 days b. reannealed between 200°C and 900°C	Bjerkelund and Kjekshus (1967)
2H-TaSe ₂ (MoS ₂ -type)	a=3.431 c=12.737	a. 600°C - 700°C for 10-15 hr. 1000°C - 1200°C for 10-15 hr. b. 900°C - 700°C for 10-15 hr. 750°C	Brixner (1962)
2H-TaSe ₂	a = 3.43 c=12.71		Brown and Beerntsen (1965)
2H-TaSe ₂	a=3.434 c=12.698		Sharma et al. (2000)
2H-Ta _{1+x} Se ₂ 0.25 < x < 0.64	When x = 0.33, a = 3.434 c = 12.87	a. 900°C for 14 days b. reannealed between 200°C and 900°C	Bjerkelund and Kjekshus (1967)

Table 2.6: 2H-TaSe₂ and its intercalated compounds

Compound	Lattice parameters(Å)	Reaction temperatures for synthesis and notes	References
2H-CuTaSe ₂		UHV method	Kordyuk et al. (2010)
2H-ATaSe ₂ (A = Na, Cs)		UHV method	Brauer et al. (2001)
2H-InTaSe ₂		Diffusion of Indium on TaSe ₂ surface	Rajora (2006)
2H-Fe _{1+x} TaSe ₂		Sintering process	Dai et al. (1993)
0.20 < x < 0.33			
2H-Fe _{0.5} TaSe ₂		Electrochemical method	Chen et al. (1992)
2H-KTaSe ₂		UHV method	König et al. (2012)
2H-ATaSe ₂ (A = Na, Cl ₂)		UHV method	Papageorgopoulos et al. (1998)
2H-(EDA)TaSe ₂	a = 3.44, c = 20.44	2H-TaSe ₂ crystal with liquid EDA kept at 150°C for 2-4 weeks	Tsang and Shafer (1978)
2H-Ni _{0.02} TaSe ₂	a = 3.434, c = 12.733	a. 900°C for 4 days b. reannealed at 900°C for 5 days c. 950°C / 830°C for 8 days	Li et al. (2010)
2H-Li _x TaSe ₂ x = 0.92, 0.20		650°C for 7-10 days, Preparing large excess of Li _x TaSe ₂ stoichiometrically	Zahurak and Murphy (1987)

Table 2.7: 3R-TaSe₂ and its intercalated compounds

Compound	Lattice parameters(Å)	Reaction temperatures for synthesis and notes	References
3R-TaSe ₂	$a = 3.4348$ $c = 19.177$	a. 900°C for 14 days b. reannealed between 200°C and 900°C	Bjerkelund and Kjekshus (1967)
3R-TaSe ₂	$a = 3.428$ $c = 19.100$	a. 600°C - 700°C for 10-15 hr. 1000°C - 1200°C for 10-15 hr. b. 900°C - 700°C for 10-15 hr. Polycrystalline materials	Brixner (1962)
3R-TaSe ₂	$a = 3.437$ $c = 19.21$	500 or 600°C	Kadijk et al. (1964)
3R-TaSe ₂		3R-TaSe ₂ nanobelt quasi-arrays were grown on a Ta foil by a surface-assisted CVT	Wu et al. (2011)
3R-Ta _{1+x} Se ₂ 0.03 < x < 0.21	When $x = 0.21$, $a = 3.444$ $c = 18.88$	a. 900°C for 14 days b. reannealed between 200°C and 900°C	Bjerkelund and Kjekshus (1967)
3R-Ta _{1+x} Se ₂	When $x = 0.05$, $a = 3.437$ $c = 19.06$ When $x = 0.10$, $a = 3.442$ $c = 18.91$	a. 600 - 1150°C b. annealed between 200 - 900°C for 2 days	Huisman et al. (1970)

Table 2.8: 4H-TaSe₂ and its intercalated compounds

Compound	Lattice parameters (Å)	Reaction temperatures for synthesis and notes	References
4H _b -TaSe ₂	$a = 3.43$ $c = 25.5$	600°C to 900°C	Kadijk et al. (1964)
4H _b -TaSe ₂	$a = 3.4575$ $c = 25.143$	a. 900°C for 14 days b. reannealed between 200°C and 900°C	Bjerkelund and Kjekshus (1967)
4H _a -TaSe ₂	$a = 3.4362$ $c = 25.399$	a. 900°C for 14 days b. reannealed between 200°C and 900°C	Bjerkelund and Kjekshus (1967)
4H _b -TaSe ₂	$a = 3.46$ $c = 25.18$	950°C	Brown and Beerntsen (1965)
4H _b -TaSe ₂	$a = 3.4552$ $c = 25.1495$		Lüdecke et al. (1999)
4H _b -TaSe ₂	$a = 3.455$ $c = 25.16$	850°C / 800°C	Nakashizu et al. (1986) Moret and Tronc (1980)
4H _b -Fe _x TaSe ₂		950°C for 5 days	Hillenius et al. (1979)

Table 2.9: 6R-TaSe₂ and its intercalated compounds

Compound	Lattice parameters(Å)	Reaction temperatures for synthesis and notes	References
6R-TaSe ₂	a = 3.4558 c=37.826	a. 900°C for 14 days b. reannealed between 200°C and 900°C	Bjerkelund and Kjekshus (1967)
6R-TaSe ₂	a=3.455 c=37.77	600°C to 900°C	Kadijk et al. (1964)
6R-TaSe ₂	a=3.46 c=37.9	Cell parameters determined and structure type assigned from powder data	Aslanov et al. (1963)
6R-TaSe ₂		CDW transitions in 6R-TaSe ₂	Fung et al. (1980)

Chapter 3

Experimental methods and techniques

3.1 Synthesis of TMDCs and their intercalated compounds

3.1.1 Preparation of polycrystalline samples

The method for the preparation of TMDCs and their intercalated compounds starts with mixing high-purity elements stoichiometrically in a quartz-glass ampoule. The ampoule is evacuated and purged by argon gas till the vacuum reaches 8×10^{-3} mbar. Then the ampoule is placed in a furnace. Both ends of the ampoule are heated for several hours or days at a certain temperature until the reaction is completed. Finally, Polycrystalline solid sample of TMDCs or intercalated TMDCs is produced (Patel et al. (2009)).

3.1.2 Chemical vapor transport method

The method of Chemical vapor transport (CVT) is a standard method for synthesis and purification of solid materials in the form of single crystals (Binnewies et al. (2013; 2012)). The growth of single crystalline materials is of particular interest as it allows the crystal structure determination by diffraction methods and measurement of anisotropy of various physical properties. Although this method was first recognized by Bunsen 150 years ago (Bunsen (1852)), Van Arkel and de Boer were the first scientists who used iodine as a transporting agent in some specific reactions

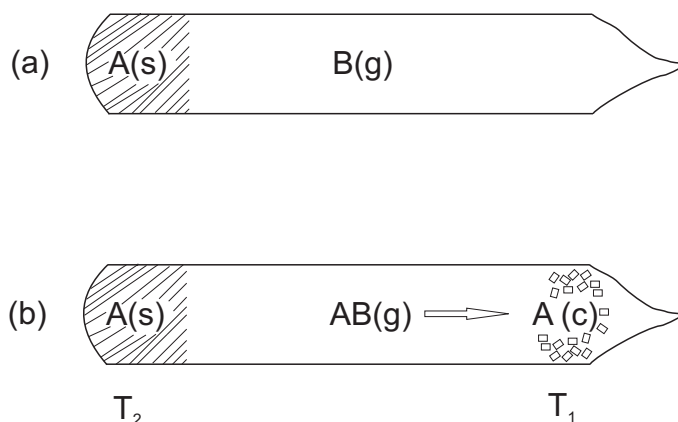


Figure 3.1: Schematic representation of the vapor transport method

(van Arkel and de Boer (1925)). Later on, Harald Schäfer developed a quantitative understanding and description of chemical transport reactions (Weil (1962)). This method has become most indispensable method for different type of transport reactions such as for metals, metalloids, intermetallic phases as well as halogens, chalcogen halides, chalcogens and many others (Binnewies et al. (2013)). The use of the CVT method for the crystal growth of sulfides and selenides of binary and ternary compounds was first introduced by Nitsche and Wild (Nitsche and Wild (1967)).

Figure 3.1 gives a schematic representation of the vapor transport reaction. Here A, a polycrystalline solid as a reactant reacts with transporting agent B at high temperature and forms unstable and volatile derivative AB. The volatile derivative migrates through the sealed, evacuated ampoule in a heated furnace. Due to the temperature gradient produced at two zones of the furnace, the volatile unstable derivative decomposes to A in crystalline form and the transporting agent is released as it is. The formation of crystal A can happen at either the hot zone or the colder zone of the ampoule, depending on the thermodynamics of the chemical reaction between the solid and the transporting agent. The reaction between A and B is as follows:



The equilibrium constant (K) of the reaction depends on the temperature, and they are interrelated by the following equation:

$$K = \exp(-\Delta G^0/RT) \quad (3.2)$$

ΔG^0 can be written as:

$$\Delta G^0 = \Delta H^0 - T\Delta S^0 \quad (3.3)$$

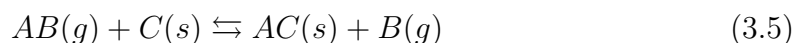
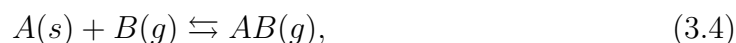
ΔG^0 , ΔH^0 and ΔS^0 are the standard Gibbs free energy, standard enthalpy and standard molar entropy respectively, for the formation of AB from A and B. For a reaction with negative reaction enthalpy, the equilibrium constant (K) will increase with the decrease of temperature (T).

Thus, AB (g) can be formed at the colder end of the ampoule and it decomposes to A(s) and B(g) at the hot end.

Similarly, for a reaction with positive reaction enthalpy, the equilibrium constant (K) will increase with the increase of temperature. Thus, AB (g) can be formed at the hot end of the ampoule and it decomposes to A(s) and B(g) at the cold end.

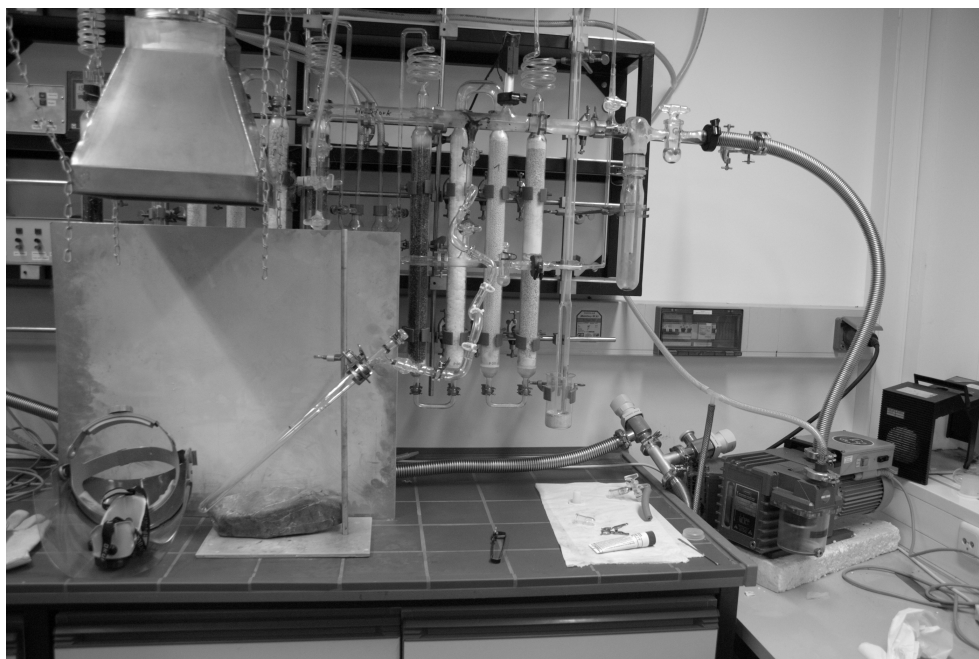
Here, the CVT method has been used for synthesizing and growing single crystals of homogeneous phase of TMDC and their intercalated compounds. The ampoule with polycrystalline sample (section 3.1.1) was placed in a two-zone furnace for the crystal growth. Here one can take small amount of polycrystalline sample to another ampoule with slight excess of chalcogen and suitable transporting agent or one can continue with the old ampoule as it is. Then the ampoule is introduced into a furnace with a temperature gradient T and T+ Δ T. Finally the ampoules are quenched to get homogeneous phase of polytype of TMDCs and their intercalated compounds. Different types of MX₂ polytypes can be synthesized depending on the heating conditions, temperature gradients, reaction time, etc. MX₂ compounds are usually stable in air and moisture but highly reactive towards strong acids and alkalis.

By using vapor transport method binary, ternary and quaternary compounds can be prepared. The reaction mechanism proceeds in the following way:



The experimental setup for vapor transport method has been shown in the figure 3.2. Here, it is interesting to see various important aspects of CVT method such as (a) Crystal growth for X-ray diffraction experiments (b) Crystal growth for studies regarding physical properties (c) Synthesis of novel (metastable) compounds and (d) Study of phase relationships by Binnewies et al. (2013).

Synthesis of copper intercalated TaSe₂ by vapor transport method and its investigation by means of single crystal X-ray diffraction study are discussed in this



(a)

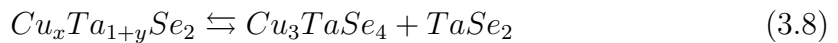
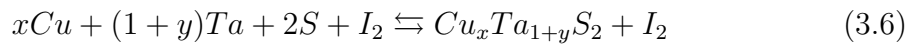


(b)

Figure 3.2: (a) Setup for vapor transport method (b) Ampoule after welding and before introducing in the furnace (At the laboratory of crystallography, university of Bayreuth).

thesis. To our knowledge, there are no such reports on crystal formation and structural investigation of $\text{Cu}_x\text{Ta}_{1+y}\text{Se}_2$ till date. Probably, it is difficult to synthesize $\text{Cu}_x\text{Ta}_{1+y}\text{Se}_2$ compounds due to the high dissociative properties of TaSe_2 than melting at higher temperature (Brixner (1962)). We have developed optimal conditions to get single crystals of $\text{Cu}_x\text{Ta}_{1+y}\text{Se}_2$ (Equation 3.7) compounds of different compositions which will be discussed in the following chapter. In addition, we have synthesized and characterized a ternary compound of Cu_3TaSe_4 (Equation 3.8) and also presented comparative study of structural parameters of Cu_3MX_4 ($\text{M} = \text{V}, \text{Nb}, \text{Ta}$; $\text{X} = \text{S}, \text{Se}, \text{Te}$) against our single crystal X-ray diffraction data. In this regard, we found that small scale synthesis is better than the large scale synthesis. The synthesis of these types of compounds has been done with the assistance of Alfred Suttner (Dipl.Ing.) at the Laboratory of Crystallography, University of Bayreuth. The characterization of these compounds was done by means of single crystal X-ray diffraction study at different temperatures.

The reactions of these compounds are the following:



3.2 Single-crystal X-ray diffraction

Single-crystal X-ray diffraction (XRD) has developed into a powerful technique that is commonly used to determine the structures of new materials. It provides a higher resolution and much better signal-to-noise ratio than powder diffraction. However, the technique is limited to the nearly perfect crystals that are suitable for diffraction. Testing of single crystals was carried out using MAR345 dtb diffractometer and MACH3 diffractometer. Data collections were performed at beamlines F1 and D3 of Hasylab (DESY, Hamburg) using synchrotron radiation with a CCD detector and also using an inhouse MAR345 dtb diffractometer with a rotating anode generator with $\text{Mo-K}\alpha$ and $\text{Ag-K}\alpha$ radiation. The experimental procedures involving different tools are described in the following sections.

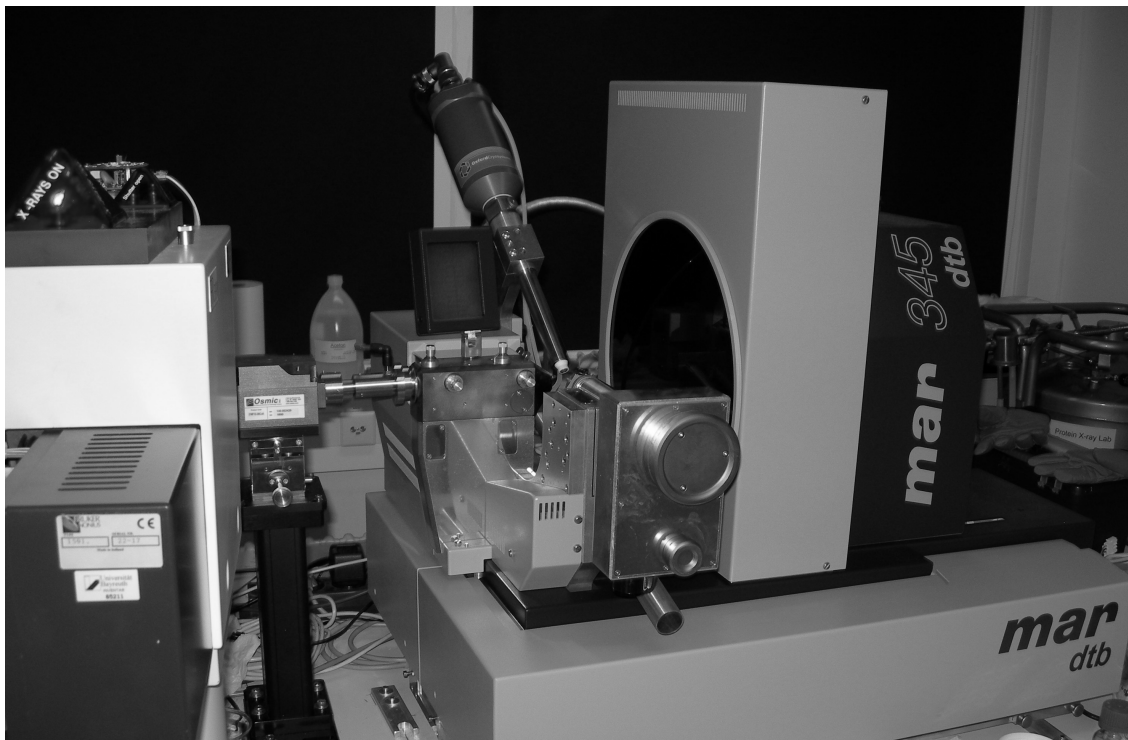


Figure 3.3: Setup of a mar345 dtb imageplate diffractometer (installed at the laboratory of crystallography, university of Bayreuth).

3.2.1 Experiments on a MAR345 dtb and Mach3 diffractometer

Mar345 dtb diffractometer consists of mar345 image plate detector and a mardtb goniometer system (Figure 3.3). The X-ray radiation is generated by a rotating anode generator with either Mo or Cu or Ag source depending on the purpose of experiment. Generally, we start with testing the quality of crystal. Crystals testing is much faster in Mar345 dtb diffractometer than the MACH3 diffractometer. After selecting good crystal one can start data collection. Data collection can be automatically carried out using the MAR345 dtb software after defining the experimental parameters for each run. Each run consists of information about the goniometer settings (2θ offset, detector distance, starting and ending ϕ value), exposure settings (exposure time, $\Delta\phi$ range, number of frames) and collimator and beam settings (beam stop distance and slit width). Data collection procedure is extensively described in the section 3.2.3.

The Nonius Mach3 diffractometer is a four-circle diffractometer having κ -geometry. The X-ray radiation is generated from Mo-rotating anode using a beam current of 75 mA and an acceleration voltage of 55 kV. Fig. 3.4 shows the MACH3 single-crystal diffractometer which is available at the Laboratory of Crystallography in Bayreuth. Generally, experiment begins with testing crystal. Crystal quality can be

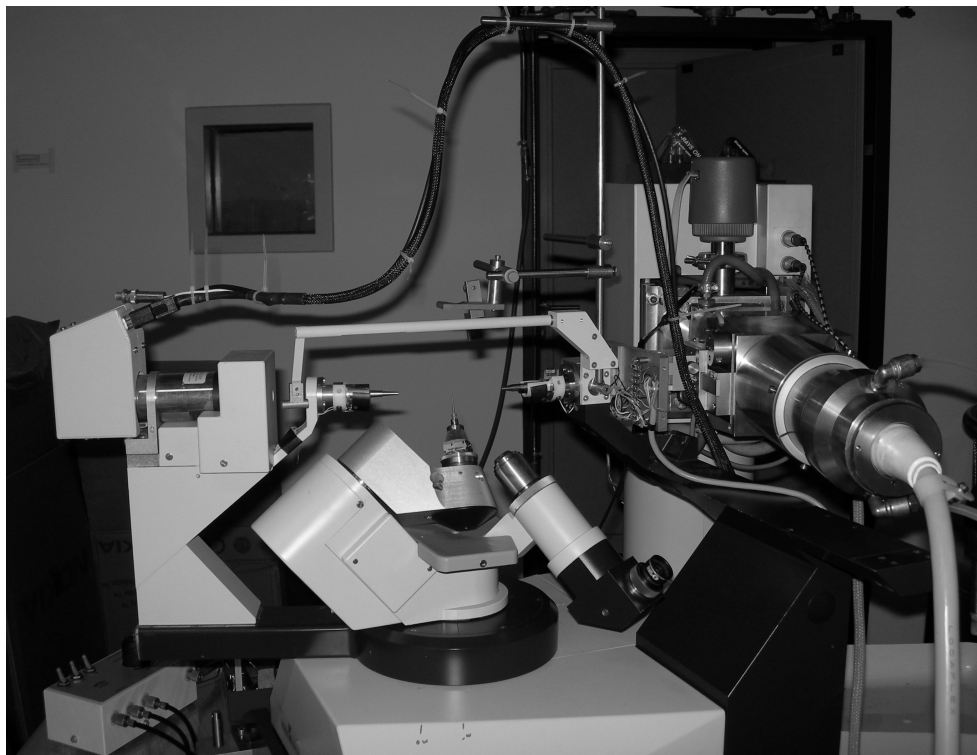


Figure 3.4: Setup of a Mach3 diffractometer using the κ -geometry (installed at the laboratory of crystallography, university of Bayreuth).

determined by doing ω -scans of some strong reflections distributed over the three lattice directions. ω -scans can be done by tilting the crystal slightly, keeping detector and X-ray source fixed. Good quality crystals normally exhibit sharp reflection profiles [Full width half maximum (FWHM) $< 0.2^\circ$] and have a similar character for different values of ϕ . The width of the peak can arise due to intrinsic width and anisotropy of the crystalline material. Materials having high mosaicity will show a broadening of the peak. The shape of the peak profiles and the FWHM of the reflections determine the material crystalline quality. Crystals which gave rise to strong reflections with peak widths (FWHM) substantially larger than the lowest

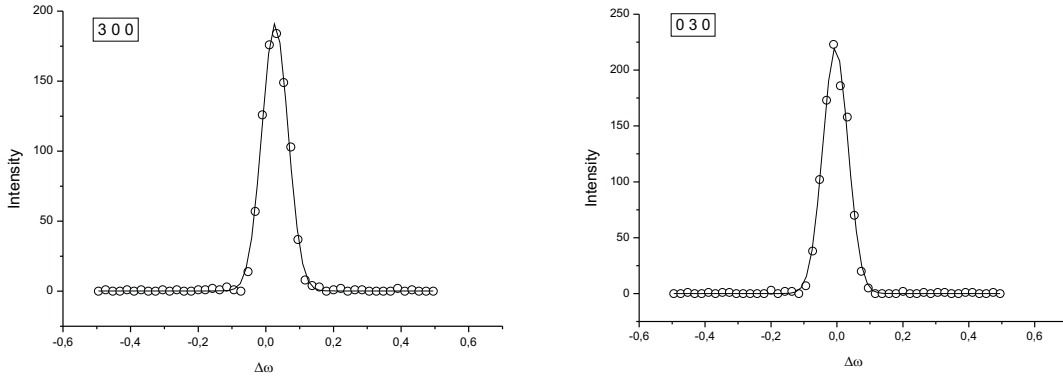


Figure 3.5: Omega scans for the reflections (a) 3 0 0 [FWHM = 0.077(1) deg] (b) 0 3 0 [FWHM = 0.076(1) deg] of 6R-Cu_xTa_{1+y}S₂ crystal. Circle represents the experimental points and these points are fitted with Gaussian function (Solid lines).

experimentally reachable value of $\sim 0.08^\circ$ were not used for synchrotron experiments. The ω -scans were measured in a continuous rotation mode rotating over angles of 1° or 2° with various scan speeds. For a higher accuracy the peak widths were determined by a curve fitting applying gaussian fit functions. An example for ω -scans of a good quality crystal of Cu_xTa_{1+y}S₂ is shown in Figure 3.5. After finding good-quality crystals, data collection can be done. However, it is not useful to measure data for those crystals having high mosaicity and large unit cell. Due to weak superlattice reflections and larger volume of the unit cell, it will take several weeks to obtain a complete dataset. After getting intensities from data collection, one needs to correct the measured reflection intensities for the effects of absorption and for that crystal shape needs to be determined. It can be determined by doing ψ -scans of some selected reflections. ψ -scans can be performed by measuring each single reflection in orientations which are equivalent to orientations resulting from rotations about the scattering vector.

The ψ -scans can be performed by measuring the intensities of reflections using ω - 2θ scans and rotating the crystal about the ψ -angle in increments of 10° . Refinement of the crystal shape against ψ -scans and/or intensity data for equivalent reflections is done by the computer program HABITUS (Herrendorf and Bärnighausen (1997)). The refinement starts by optimizing a starting model for the crystal, consisting of a high symmetric form possessing many faces e.g. by using an icosahedron. Then

the program optimizes the crystal shape by changing the distances of the faces to the center and also by changing the tilting of the faces. Finally, by looking on the goodness of the refinement in terms of R (REND) one can decide how good the model is. A reasonable crystal shape should lead to R-values below 10%. It would be good idea to compare the model found from HABITUS and the real crystal shape observed in an optical microscope. Now, at this moment absorption correction of the intensities of the reflections can be performed by using the integration program SADABS (Sheldrick (2008)) or refinement program Jana2006 (Petricek, V. and Dusek, M. and Palatinus, L. (2006)). Finally structure solution can be done by the program superflip (Palatinus and Chapuis (2007)) and refinement of the structure solution by program Jana2006 (Petricek, V. and Dusek, M. and Palatinus, L. (2006)).

Temperature-dependent experiments can also be done using MACH3 diffractometer. After refining orientation matrix of supercell, some superlattice reflections and main reflections of comparable scattering vector are selected. These experiments require a stable cooling system for getting stable temperature. In our experiments, crystal temperatures were established using Oxford cryostream cooling device. In this device, the crystal temperatures is controlled by nitrogen gas stream which steadily blows on to the crystal. The nitrogen gas is produced by vaporization of liquid nitrogen with the rate of 5 ml/min. Data collection of selected superlattice and main reflections can be done at each temperature. Also it is important to refine the orientation matrix in each step to get accurate lattice constants at that temperature. Now the integrated intensities of reflections can be plotted with respect to the temperature so that one can easily notice if there exists any phase transition.

3.2.2 Experiments at Synchrotron center using CCD detector

Synchrotron radiation is a source for X-ray radiation, which occurs when charged particles (electrons or positrons) are accelerated through a magnetic field in a curved path. The radiation is not only very intense, it also possesses a low divergence, a high spectral brilliance and it is almost completely polarized in the horizontal plane. The important advantage of synchrotron radiation is the tunability of the wavelength, as a result one can minimize the X-ray absorption by the crystal. X-ray absorption is dependent on the crystal size and absorption coefficient. The absorption coefficient is dependent on the photon energy of the radiation. The energy of the radiation can be

fixed by fixing the wavelength of the radiation, accordingly to the minimum energy required to avoid maximum absorption by the crystal. The softwares XOP and JANA2006 (Del Rio and Dejeus (1998); Petricek, V. and Dusek, M. and Palatinus, L. (2006)) have been used to compute the absorption coefficient as a function of the wavelength of the radiation for each compound.

In our experiments, CCD (charge coupled device) detectors have been used at both beamlines F1 and D3 of HASYLAB at the Deutsches Elektronen Synchrotron (DESY) in Hamburg, Germany. The F1 beamline has a Huber 4-circle diffractometer with κ -geometry and is equipped with a MARCCD system (Fig. 3.6), whereas

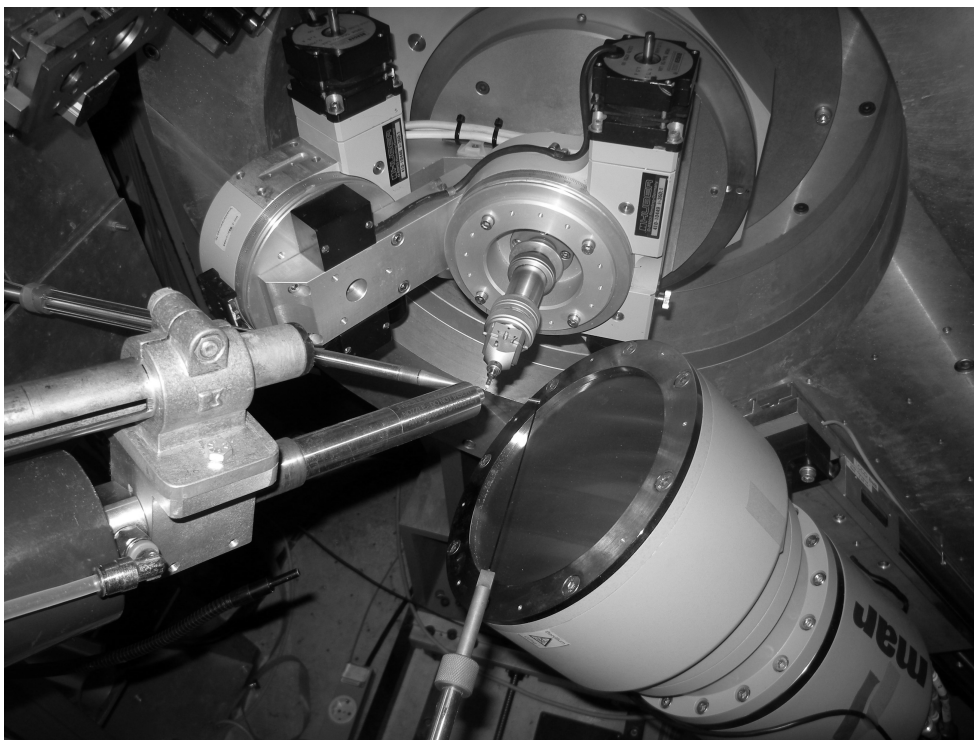


Figure 3.6: Experimental setup of beamline F1 (DESY, Hamburg) used for the data collection.

D3 beamline has 4-circle diffractometer with Euler geometry (Fig. 3.7). In both euler and κ -geometry, the ω -axis is oriented parallel to the 2θ -axis which represents the rotation of the detector. In euler geometry, ϕ - axis represents the rotation axis around the goniometer head (where the crystal is mounted), χ axis allows the crystal to move around the closed circle, and ω -axis allows the complete goniometer to rotate around a horizontal axis. This geometry is very useful for closed cycle low

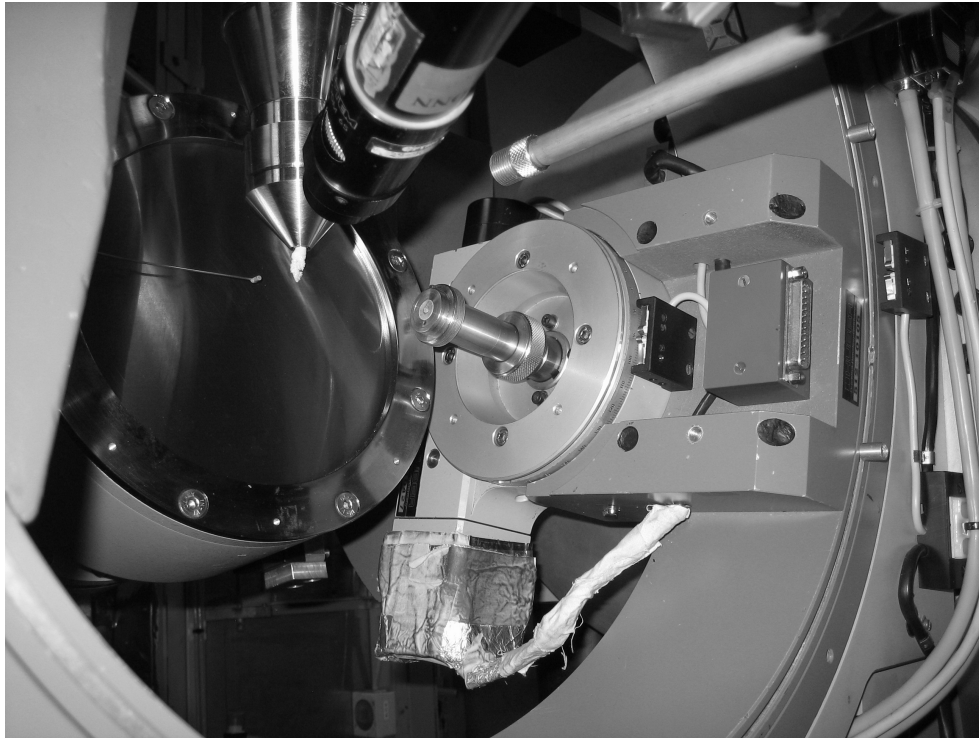


Figure 3.7: Experimental setup of beamline D3 using mar-CCD detector (DESY, Hamburg) used for the data collection.

temperature study (due to a high mechanical stability) but has some restrictions for external devices (for instance, low or high temperature devices) due to bulky Euler-cradle.

In the κ -geometry which does not have an equivalent to the closed χ circle but it can be fulfilled by κ and ω axes. The main advantage of the Kappa geometry is the wide accessibility of the crystal. Also goniometer in this type of geometry can be used for the open gas flow measurement as rotation about the omega axis is not hindered by the bulky Euler-cradle.

3.2.3 Data collection strategy at D3 and F1

Data collection in both D3 and F1 are operated by Online software, which is basically developed by beamline scientist of Desy, Hamburg (Kracht (2013)). The software reads the user-defined sequences of runs which contain types of scans (ϕ , ω), scan width, angular setting of the detector and goniometer, exposure time and number of

frames to be measured. The wavelength of the radiation can be set in such a way so that we can optimize absorption which occurs by the crystal. In our experiments, a wavelength of 0.56 Å has been used. Before starting data collection one has to choose the distance between crystal and detector, in such a way so that two closely spaced reflections can be resolved. Overlap of reflections gives wrong intensities during data reduction. Generally, one needs to choose long crystal-to-detector distances for those structures have long cell axes that means it has short reciprocal axes. Crystal-to-detector distance of 200 mm has been maintained due to long c-axis of approximately 76 Å for the $\text{Cu}_x\text{Ta}_{1+y}\text{S}_2$ compound. The next step is to decide scan step in such a way that two peaks are resolved between two consecutive frames. Generally, a step scan of 0.5° or 1.0° has been used and in some special cases other values are used. At this moment one can start the experiment to find out correct exposure time. The experiment is started with minimum exposure time then scale it in such a way so that maximum intensity will be ~ 35000 to 40000 cps to avoid overexposed peaks. In this regard, one has to consider the beam intensity. Now one can start data collection with phi scan at 2θ -offset of zero for 180 frames. It is also useful to collect one more dataset with higher exposure time to get the weak satellite reflections. Now, at this moment phi scan can be started at different offset values with higher exposure time. The choice of exposure time depends on the 2θ -offset values of the detector. With 2θ -offset needs higher exposure time to reveal weak satellite reflections at higher Bragg angles. After finishing phi scan, omega scan can be started at at different phi values to get the reflections which cannot be measured by phi scan. It increases the completeness of the dataset.

3.3 Bond valence sum method

The bond valence method or bond valence sum (BVS) is a technique used in coordination chemistry to find out the oxidation states or valence states of atoms (Brown (2009); Brown and Altermatt (1985); Brown and Shannon (1973)) in compounds. This method is very much useful as a measure of the strength of the bond. It is frequently used to validate newly determined crystal structures though it has many other uses in the analysis and modeling of crystal structures.

The bond valence method comes from the idea of Pauling long time back (Pauling (1929)). The basic idea is that the valence V_i of an atom is the same, irrespective of the compound in which the atom is located. And it can be written as the sum of

the individual bond valences (v_{ij}) of the surrounding atoms.

$$V_i = \sum_{j=1}^n (v_{ij}) \quad (3.9)$$

v_{ij} is the valence of a bond between cation i and the anion j . j vary from 1 to a finite value of n . It can be obtained from the crystal structure by:

$$v_{ij} = \exp[(R_o - R_{ij})/b] \quad (3.10)$$

$$V_i = \sum_{j=1}^n \exp[(R_o - R_{ij})/b] \quad (3.11)$$

R_{ij} is the observed length of a bond between cation and anion, R_o is the empirical parameters, obtained by a fit to known crystal structures (O'Keeffe and Brese (1992); Brown and Altermatt (1985)). All values in the equation (3.11) are in Ångström units. b is an empirical constant, typically 0.37 Å. R_o and b are dependent to each other, and using a different value of b necessarily means a different value of R_o . The parameters also depend on the maximum distance that can be considered to be a bond. In most cases this distance can be taken as around 3Å. For wide range of distances in a bond such as O-H, N-H, etc. one needs to put different values of parameters to get accurate bond valence. Finally, V_i represents the valence of atom i . In this thesis, BVS method has been used for Cu_3MX_4 ($\text{M} = \text{V}, \text{Nb}, \text{Ta}$; $\text{X} = \text{S}, \text{Se}, \text{Te}$) type of ternary compounds.

Chapter 4

Self intercalation and vacancy ordering in 6R-Cu_xTa_{1+y}S₂ ($x \approx 0.23$, $y = 0, 0.06$)¹

4.1 Abstract

The eightfold $2a_0 \times 2b_0 \times 2c_0$ superstructures of 6R-Cu_xTa_{1+y}S₂ are reported for crystal A with $x = 0.237$ and $y = 0$, and crystal B with $x = 0.23$ and $y = 0.06$. Compelling evidence is presented for the self-intercalation of Ta onto octahedral sites, based on the diffraction data and crystal chemical arguments. The eightfold superstructure is formed by partial vacancy ordering within planes of intercalated atoms, while the stacking of TaS₂ layers remains that of the 6R polytype. Temperature-dependent X-ray diffraction experiments show that the superstructure exists between $T = 14$ K and at least 370 K. Intercalated atoms enter the compound at octahedral and tetrahedral sites in alternating Van der Waals gaps. Intercalation is inhomogeneous, with average occupancies varying between 0.11 for octahedral sites within one Van der Waals gap and 0.23 for the tetrahedral sites within another Van der Waals gap. It is proposed that partial vacancy ordering is governed by the principle of maximum separation between intercalated atoms.

¹This Chapter has been published as Self intercalation and vacancy ordering in 6R-Cu_xTa_{1+y}S₂ ($x \approx 0.23$, $y = 0, 0.06$). S. I. Ali, S. Mondal, S. J. Prathapa, S. Van Smaalen, S. Zörb, B. Harbrecht. *Z. Anorg. Allg. Chem.*, **638**, 2625-2631, (2012).

4.2 Introduction

Transition metal dichalcogenides are known for their polytypism related to various stackings of layers of composition MX_2 ($\text{M} = \text{Ta}, \text{Nb}, \text{Ti}, \text{V}, \text{Mo}$; $\text{X} = \text{S}, \text{Se}, \text{Te}$) (Jellinek (1962); Wilson et al. (1975)). Their pronounced anisotropy is responsible for exotic electronic states, like charge-density waves (CDWs) and superconductivity, which may appear depending on the composition and crystal structure (Wilson et al. (1975); Sipos et al. (2008)). The layered structures allow the intercalation of molecules and atoms into the Van der Waals gaps between the layers (Friend and Yoffe (1987)). Intercalated atoms ionize by donating valence electrons to the quasi-two-dimensional (2D) d-band of the transition metal atoms. This process affects the electronic properties, often leading to a suppression of the CDW transition and sometimes being responsible for the development of superconductivity at low temperatures (Moroson et al. (2006); Zhu et al. (2009)).

Intercalated transition metal dichalcogenides A_xMX_2 ($\text{A} = \text{alkali metal}, \text{Cu}, \text{Ag}$) form for compositions x between zero and a maximum filling that is usually less than one. Preferred locations for the intercalated atoms are the octahedral and tetrahedral sites in the closed-packed arrangement of X atoms. Partial filling of the Van der Waals gaps imply fractional occupancies of these sites or the formation of superstructures due to vacancy ordering. For example, for $\text{Co}_{1/3}\text{NbS}_2$ it was proposed that one third of the octahedral sites are occupied by cobalt ions, resulting in $\sqrt{3}a_0 \times \sqrt{3}b_0 \times c_0$ superstructure of the 2H-NbS₂ polytype (Nakayama et al. (2006)). Vacancy ordering can be more complicated, as in the incommensurate superstructure of $\text{Ag}_{0.6}\text{NbS}_2$, which is again based on the 2H-NbS₂ polytype (van der Lee et al. (1991)).

Another phenomenon is that of self-intercalation, i.e. the formation of M_{1+y}X_2 compounds with an amount y of M atoms located within the Van der Waals gaps. Self-intercalation ($y \neq 0$) has been considered essential for the stabilization of 1T- $\text{Ti}_{1+y}\text{S}_2$ (Inoue et al. (1989)). Self-intercalation has also been found in 3R- $\text{Ta}_{1+y}\text{S}_2$ with $y = 0.08$ (Gotoh et al. (1998)). $\text{Cu}_x\text{Ta}_{1+y}\text{S}_2$ with $x < 0.3$ and $y < 0.2$ have been synthesized by Harbrecht and Kreiner (Harbrecht and Kreiner (1989)). The crystal structures are based on 6R-TaS₂ with alternating Van der Waals gaps containing a statistical distribution of Cu atoms on tetrahedral sites and a statistical distribution of intercalated Ta atoms on octahedral sites, respectively (Harbrecht and Kreiner (1989)). Cu_xTaS_2 ($x = 0.23$; $y = 0$; 6R polytype) has been found to contain a statistical distribution of copper atoms over both octahedral and tetrahedral sites

(Bohnen (1995)).

Ordering of the intercalated atoms over the available sites as well as CDWs or superconductivity may appear in intercalated transition metal dichalcogenides as the result of phase transitions. Here we present the results of a temperature-dependent X-ray diffraction study on $\text{Cu}_x\text{Ta}_{1+y}\text{S}_2$ ($x \approx 0.23$, $y = 0, 0.06$). Partial vacancy order is already present at room temperature, expressed by vacant sites and sites with fractional occupancies by intercalated atoms. We show that the $2a_0 \times 2b_0 \times 2c_0$ superstructure with three crystallographically independent Van der Waals gaps, contains two types of planes of intercalated metal atoms, which occur both with atoms occupying octahedral sites and with atoms occupying tetrahedral sites. Vacancy ordering is explained on the basis of effective repulsive interactions between intercalated atoms. Low-temperature X-ray diffraction does not exhibit additional superlattice reflections, neither those pertaining to a possible further ordering of the intercalated atoms nor those pertaining to possible CDWs.

4.3 Experimental

4.3.1 Synthesis

Single crystals of $6\text{R-Cu}_x\text{Ta}_{1+y}\text{S}_2$ were synthesized in previously out-gassed, evacuated, sealed quartz-glass ampoules from reactions of the elemental components (approximately 1 g in total) allocated in the ratio $\text{Cu}_{0.20}\text{Ta}_{1.10}\text{S}_2$ together with 2.5 mg iodine as transporting agent (Bohnen (1995)). The reaction was initiated by heating the ampoule with a burner. Hereafter, the ampoule was exposed to a temperature gradient of 1293-1308 K for four days and finally quenched in cold water.

4.3.2 X-ray diffraction

Three crystals were selected from a single batch of synthesis, and glued on glass fibers for X-ray diffraction experiments. Crystal A of dimensions $0.15 \times 0.1 \times 0.05 \text{ mm}^3$ was used for a diffraction experiment at $T = 100 \text{ K}$ using synchrotron radiation at beamline F1 of Hasylab (DESY, Hamburg) under cold nitrogen gas flow. Slight broadening of Bragg reflections indicated a sub-optimal quality of crystal A. Therefore, crystal B of dimensions $0.13 \times 0.1 \times 0.05 \text{ mm}^3$ was selected for another low-temperature experiment, now at beamline D3 of Hasylab. The sample temperature was set to $T = 14 \text{ K}$ employing an open-flow helium cryostat. For both

experiments MAR-CCD detectors were used for measuring the scattered radiation. A large crystal-to-detector distance of 200 mm was chosen in order to resolve closely spaced Bragg reflections. Diffraction data were collected by ϕ scans and ω scans with a step width of 0.5° per image. Several values were chosen for the off-sets of the detector and crystal orientation, in order to obtain data sets of high resolution. Each run was repeated with different exposure times, as to measure weak (superlattice) reflections, while strong main reflections are overexposed in the runs with long exposure time. Crystal B was lost after having completed the data collection up to $[\sin(\theta)/\lambda]_{max} = 0.8 \text{ \AA}^{-1}$.

Indexing and data integration with EVAL15 (Schreurs et al. (2010)) resulted in lattices that can be considered as eightfold ($2a_0 \times 2b_0 \times 2c_0$) superlattices of the basic structure described by Bohnen (Bohnen (1995)). Here, reflections (hkl) with all indices even are main reflections and other combinations of indices describe relatively weaker superlattice reflections. Absorption correction was applied by the computer program SADABS (Sheldrick (2008)). Reflection conditions and Laue symmetry indicated rhombohedral symmetry with space group $R\bar{3}m$ for the superstructure. Consideration of only main reflections resulted in the same space group for the basic structure, in accordance with Bohnen (Bohnen (1995)). Experimental data and crystallographic information for both crystals are summarized in Table 4.1.

Crystal C of dimensions $0.13 \times 0.1 \times 0.04 \text{ mm}^3$ was selected for a temperature-dependent experiment under nitrogen gas flow on a NONIUS MACH3 diffractometer using Mo-K α radiation of wavelength 0.71073 \AA . Lattice parameters at $T = 100 \text{ K}$ were determined as $a = 6.6613 (13) \text{ \AA}$ and $c = 75.202 (12) \text{ \AA}$ with $V = 2889.9 (11) \text{ \AA}^3$, which indicate similar compositions of crystals A and C. The lattice parameters of crystal C were also found to be in good agreement with those determined from a powder X-ray diffraction pattern (Philips MPD diffractometer, PIXcel detector PANalytical, Cu-K α radiation) by a Rietveld refinement (program X'Pert, Philips) based on the positional parameters of the single-crystal structure refinement: $a = 6.6386 (7) \text{ (\AA)}$, $c = 75.267 (7) \text{ (\AA)}$ and $V = 2872.7 (7) \text{ \AA}^3$. Superlattice reflections corresponding to a $2a_0 \times 2b_0 \times 2c_0$ superstructure were not visible in the powder diffraction, but a few weak additional reflections pointed to the presence of a second, not yet identified phase.

Integrated intensities of six strong superlattice reflections and six main reflections of comparable scattering vectors have been measured at 13 selected temperatures between 90 K and 370 K. The intensities of all reflections exhibit similar temperature dependencies. A typical result is given in Fig. 4.1.

Table 4.1: Crystallographic data of crystals A and B.

	Crystal A	Crystal B
Chemical formula	$\text{Cu}_{0.237}\text{TaS}_2$	$\text{Cu}_{0.23}\text{Ta}_{1.06}\text{S}_2$
Formula weight /g.mol ⁻¹	259.68	263.34
temperature /K	100	14
Crystal system	Trigonal	Trigonal
Space group	$R\bar{3}m$	$R\bar{3}m$
a /Å	6.6655 (8)	6.6083 (3)
c /Å	75.3016 (81)	74.6166 (85)
V /Å ³	2897.3	2821.9
Z	48	48
Crystal size /mm ³	$0.15 \times 0.1 \times 0.05$	$0.13 \times 0.1 \times 0.05$
Radiation	Synchrotron	Synchrotron
Wave length /Å	0.5600	0.5600
indices range	$-12 \leq h \leq 12$ $-15 \leq k \leq 15$ $-136 \leq l \leq 141$	$-10 \leq h \leq 10$ $-9 \leq k \leq 9$ $-118 \leq l \leq 94$
Θ -range /deg	1.92-30.27	1.94-26.47
No. observed reflections [$I > 3\sigma(I)$]	1628	1213
R_{int}	0.055	0.036
$(\sin\theta/\lambda)_{max}$ /Å ⁻¹	0.9	0.8
R_F / wR_F [$F > 3\sigma(F)$]	5.77 / 7.71	4.59 / 7.03
R_F / wR_F [$F > 3\sigma(F)$]	5.17 / 6.49	3.94 / 6.09
main reflections		
R_F / wR_F [$F > 3\sigma(F)$]	7.92 / 9.07	6.80 / 7.74
superlattice reflections		
GoF (all)	2.12	1.93
twinvol1 / twinvol2	0.545 / 0.455	0.33 / 0.67

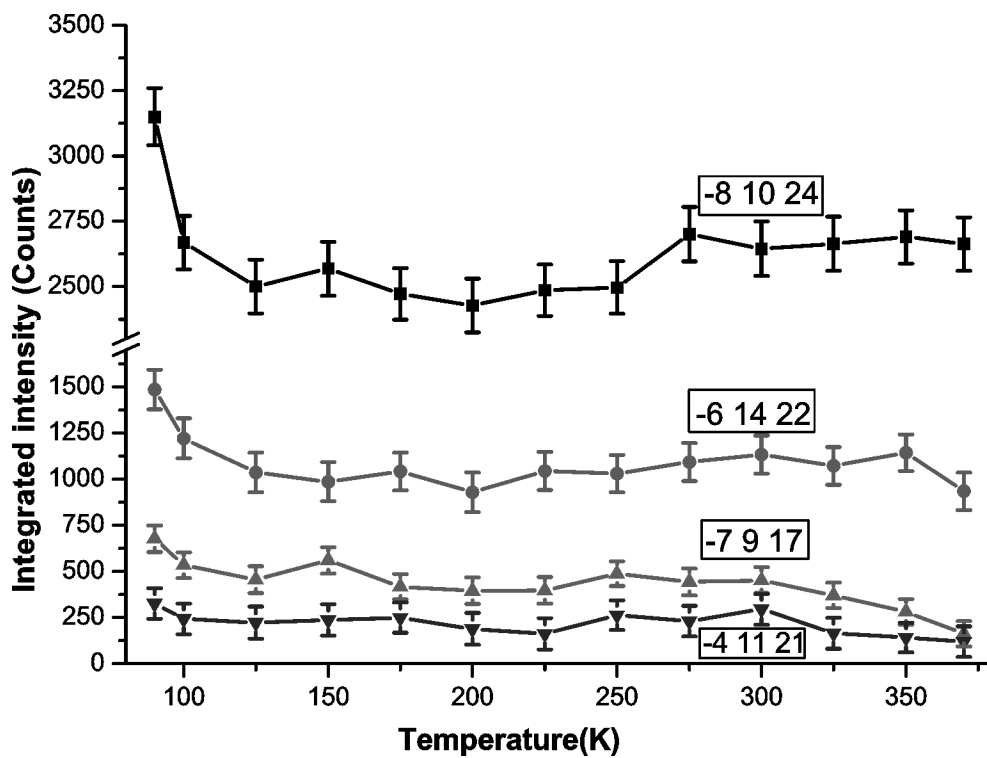


Figure 4.1: Temperature dependence of the integrated intensities of selected superlattice reflections and main reflections of crystal C.

Table 4.2: Structural parameters of the basic structure of 6R-Cu_{0.23}TaS₂ (crystal A) at T = 100 K. ($x_0 = y_0 = 0$; Occ. = occupation factor)

Atom	Wyckoff site	z_0	$U_{equiv}/\text{\AA}^2$	Occ.
Ta	6c 3m	0.080484 (7)	0.0034 (1)	1
Cu1	3a $\bar{3}m$	0	0.0046 (24)	0.18 (2)
Cu2	6c 3m	0.15534 (30)	0.0042 (19)	0.15 (1)
S1	6c 3m	0.21099 (7)	0.0042 (4)	1
S2	6c 3m	0.29422 (6)	0.0031 (3)	1

4.3.3 Crystal structure refinements

The basic structure of the 6R-Cu_{0.23}TaS₂ has been described by Bohnen (Bohnen (1995)). This structure was confirmed by refinement against the main reflections of the present data (Table 4.2). All structure refinements were done with JANA2006 (Petricek, V. and Dusek, M. and Palatinus, L. (2006)). The model for basic structure of 6R-Cu_{0.23}TaS₂ was transferred to the supercell by taking into account the loss of translational and rotational symmetry. Each of the five independent atoms in the basic structure gives rise to four crystallographically independent atoms in the supercell, which were enumerated by adding one letter a-d to the atomic names, respectively. Thus, the superstructure contains twenty crystallographic independent atoms (Fig. 4.2). The superstructure was solved by refinement of all parameters allowed by symmetry, starting with their values in the basic structure. A smooth convergence to a good fit to the data was found for both data sets. Fractional occupancies of the eight copper sites were varied in the refinements. Small negative occupancies were found for two sites, which were then set to zero for the final refinements. Partial R values were computed for the subset of main reflections and for the subset of superlattice reflections. Low values for both types of partial R values indicate that the superstructures have been solved. The superstructure model for crystal A (T = 100 K) contains reasonable values for ADPs, and the chemical composition Cu_{0.23}TaS₂ as computed from the refined occupancy parameters of the copper sites falls within the reported stability range ($0.21 < x < 0.24$) of the intercalated 6R phase, as previously determined (Bohnen (1995)).

The model for the superstructure of crystal B (T = 14 K) was not satisfactory, despite reasonably low R values (Table 4.3). It contained non-positive-definite ADPs for two copper atoms and the refined composition Cu_{0.23}TaS₂ was beyond the

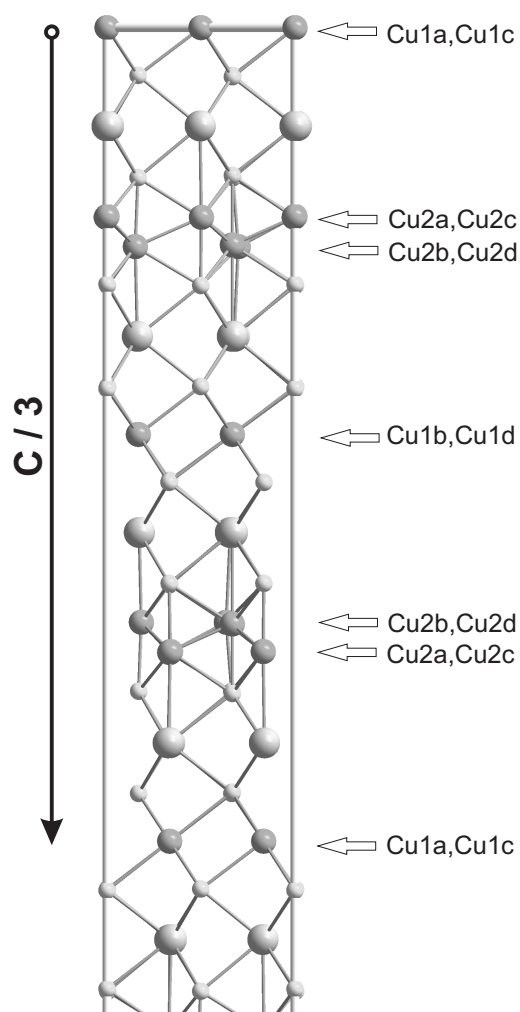


Figure 4.2: Projection of the crystal structure of $6R\text{-Cu}_{0.237}\text{TaS}_2$ (crystal A) onto the mirror plane $(\bar{2}10)$. The origin is in the left upper corner on the (empty) site Cu1a. The horizontal axis is $(a/2) + b$. Large circles indicate Ta, intermediate size Cu, and small circles stand for S.

Table 4.3: R values of different models for 6R-Cu_{0.23}Ta_{1.06}S₂ (Crystal B)

Model	R _F (obs)	wR _F (obs)	R _F (all)	wR _F (all)	Chemical formula and notable result
I (Ta, Cu1, Cu2, S1, S2)	5.33	7.99	9.12	8.69	Cu _{0.37} TaS ₂ with negative U _{equiv} for Cu1b, Cu1d
II (Ta1, Ta2, Cu2, S1, S2)	4.59	7.03	8.15	7.66	Cu _{0.23} Ta _{1.06} S ₂
III (Ta1, Cu1, Ta2, S1, S2)	5.93	8.27	9.61	9.05	Cu _{0.15} Ta _{1.14} S ₂ with negative U _{equiv} for S1a, S1b, S1d

published stability range (Bohnen (1995)). Therefore, two other structure models were tried, in which Cu1 or Cu2 were replaced by Ta, respectively. A considerably improved fit to the diffraction data was obtained for Ta2a-d replacing Cu1a-d. This model also solved the problem of non-positive-definite ADPs and lead to a refined chemical composition Cu_{0.23}Ta_{1.06}S₂ in accordance with the stability range. Replacing Cu2a-d by tantalum atoms resulted in an increase of R values and again a model with non-positive-definite ADPs (Table 4.3). Replacing Cu1a-d by Ta in the model for crystal A worsened the fit to the diffraction data at 100 K toward R_F = 6.57 % (compare to Table 4.1), while ADPs of Cu2a-d became non-positive-definite.

Together, these results demonstrate the sensitivity of single-crystal diffraction to the presence of Cu vs. Ta at the intercalation sites. The results show that an intercalation model with Cu on tetrahedral and Ta on octahedral sites is the only model in agreement with the X-ray diffraction data of crystal B, while intercalation of exclusively Cu is the only model in agreement with the X-ray diffraction data of crystal A.

4.4 Discussion

The eightfold superstructure of 6R-Cu_xTa_{1+y}S₂ ($x \approx 0.23$, $y = 0, 0.06$) is found to be the result of partial ordering of the intercalated atoms over the available sites within the Van der Waals gaps ("vacancy ordering"). The absence of a temperature dependence of the ratio of intensities of superlattice and main reflections shows that the vacancy ordering is already present at room temperature (Fig. 4.1). This finding is in agreement with the observed intercalation in crystal B of tantalum atoms, which

are believed to be immobile at low temperatures (Harbrecht and Kreiner (1989)). Phase transitions down to 14 K have not been observed.

Strong evidence has been obtained for the presence of intercalated tantalum atoms in crystal B. The fit to the diffraction data is much better for the correct model than for a model with Cu replacing Ta, while the chemical composition and ADP parameters attain reasonable values only in case of Ta as intercalant (Table 4.3). It is noticed that Ta goes onto the intercalation sites with octahedral coordination by sulfur, which is the preferred coordination of tantalum, and not on the tetrahedral intercalation sites; the latter model again gives a substantially worse fit to the diffraction data (Table 4.3). On the basis of the observed larger filling with intercalated atoms, one would expect a unit-cell volume that is larger for crystal B than for crystal A. Observed is the opposite. We do not have an explanation for this effect, except that possibly the synchrotron radiation did have a different wave length than intended. The present results show that the batch of synthesis has produced single crystals of inhomogeneous composition, which is not an unusual phenomenon. The temperature at which crystals have been grown in the present experiment is lower than the temperature for stabilization of $\text{Cu}_x\text{Ta}_{1+y}\text{S}_2$ previously reported (Harbrecht and Kreiner (1989)). A possible explanation is that the presence of copper might have promoted the intercalation of tantalum. In this respect it is interesting that recently $3R\text{-Ta}_{1+y}\text{S}_2$ has been obtained at similar temperatures, when attempting synthesis of $[\text{GdS}]_{1.2}[\text{TaS}_2]$ (Gotoh et al. (1998)).

The crystal structures of $6R\text{-Cu}_x\text{Ta}_{1+y}\text{S}_2$ ($x \approx 0.23$, $y = 0, 0.06$) are built of layers TaS_2 with Ta in trigonal prismatic coordination by sulfur. The stacking sequence is (a)CaC(a,c)AcA.(c)BcB(c,b)CbC.(b)AbA(b,a)BaB(a) where each letter stands for a plane of atoms with the structure of closest packing of spheres. Capital letters indicate planes of sulfur atoms, small letters indicate the Ta sites within the TaS_2 layers, and letters in brackets indicate the intercalation sites with (a), (c) and (b) being octahedral sites and (a,c), (c,b) and (b,a) indicating pairs of tetrahedral sites (compare to Fig. 4.2). Centering translations of the rhombohedral lattice imply that one hexagonal unit cell contains three translational units along c (separated by a dot in the sequence above). Therefore, the $6R$ structure contains two crystallographically independent Van der Waals gaps, of which one contains intercalated atoms on octahedral sites and the other contains intercalated atoms on tetrahedral sites. Doubling of the unit cell axes in the directions of a and b allows for vacancy ordering as denoted in Figure 4.3 and Figure 4.4. Doubling of the c axis is the result of complementary ordering in consecutive octahedral layers, and

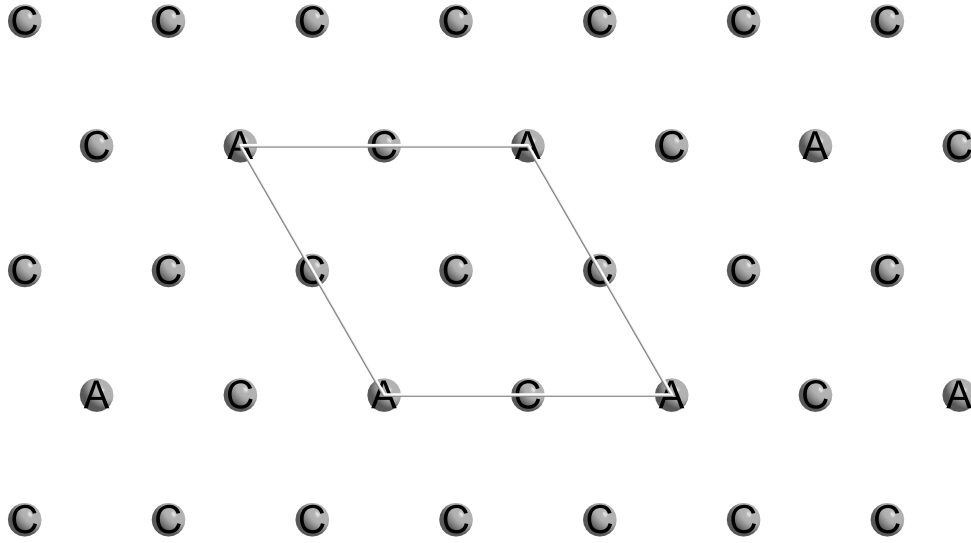


Figure 4.3: Plane of intercalation sites Cu1/Ta2 at $z = 0$. (A = Cu1a/Ta2a; C = Cu1c/Ta2c). An identical pattern is found at $z = 1/2$ for A = D = Cu1d/Ta2d and C = B = Cu1b/Ta2b.

ordering within consecutive tetrahedral Van der Waals gaps that are related to each other by inversion symmetry (Fig. 4.2). Superstructure formation does not affect the stacking of TaS₂ layers, which remains of 6R type.

Each plane of intercalated atoms exhibits the same pattern with four sites per $2a_0 \times 2b_0$ unit cell split into one atom from a crystallographically independent site with threefold multiplicity (A and D in Figure 4.3 and Figure 4.4) and three atoms of a second independent site of ninefold multiplicity (C and B in Figure 4.3 and Figure 4.4). The other symmetry-equivalent atoms of these sites are located in other Van der Waals gaps as related by the centering translations to the first Van der Waals gap. In case of tetrahedral sites the multiplicity is double of that mentioned above, but the additional atoms occur in again other Van der Waals gaps, now related to the first one by inversion symmetry (Figure 4.2). Only two fundamental types of vacancy ordering are found. In one type of plane, the threefold (sixfold for tetrahedral) site is a vacancy or at least has very low occupancy (sites Cu1a / Ta2a, Cu2a), while in the other type of plane the ninefold (18-fold for tetrahedral) site has low occupancy (Table 4.4).

The shortest distance between intercalation sites is between tetrahedral sites of different planes within a single Van der Waals gap (pairs AB, CB and CD in

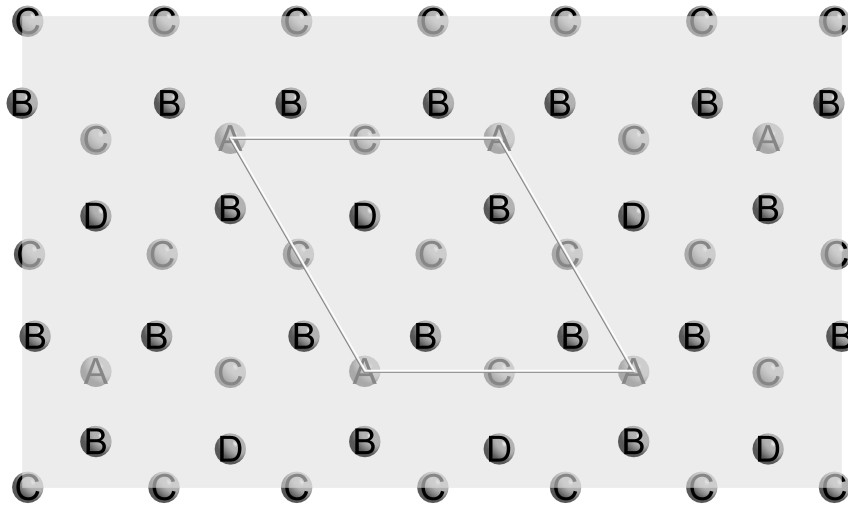


Figure 4.4: Double plane of intercalation sites Cu_2 at $z \approx 1/12$. $A = \text{Cu}_{2a}$ and $C = \text{Cu}_{2c}$ are in one plane at $z \approx 0.078$; $B = \text{Cu}_{2b}$ and $D = \text{Cu}_{2d}$ form the second plane at $z \approx 0.090$. An inverted filling is found at $z \approx 3/12 = 1/4$ with $B = \text{Cu}_{2b}$ and $D = \text{Cu}_{2d}$ at $z \approx 0.240$, and $A = \text{Cu}_{2a}$ and $C = \text{Cu}_{2c}$ at $z \approx 0.255$

Figure 4.4). This distance (average value 2.128 Å for crystal A and 2.110 Å for crystal B) is much shorter than the Cu-Cu distance of 2.56 Å in elemental copper, so that simultaneous occupation is impossible for both sites of these pairs. With this boundary condition, we can fill all sites in one of the two planes of tetrahedral sites (e.g. A and C in Figure 4.4) while the other plane then must remain empty, resulting in an average occupancy of 1/2 of the sites in the tetrahedral Van der Waals gap. Together with full occupancy of the octahedral sites, this leads to a theoretical maximum occupancy of $x + y = 1$.

Equal occupancies of the two planes of tetrahedral sites allow full occupation of sites A and D, resulting in a maximum average occupancy of 1/4 of tetrahedral sites. Alternatively, with half the D sites occupied, half of the C sites and one third of the B sites could accommodate atoms, such that simultaneous occupation of nearby C and D sites as well as nearby C and B sites is avoided by short-range order. The observed vacancy order fulfils this condition (Table 4.4).

The experimental average filling of Van der Waals gaps equal $x + y$, and are well below the theoretical limit of one as computed above. The pattern of vacancies can be rationalized by the notion that a maximum separation of intercalated atoms provides the most favorable arrangement. The fully ordered crystal structure of $\text{Co}_{1/3}\text{NbS}_2$ on a $\sqrt{3}a_0 \times \sqrt{3}b_0$ supercell shows that an occupancy of 1/3 is the maximum filling of octahedral sites at which each atom has vacancy sites as its nearest neighbors (Nakayama et al. (2006))(c.f. Fig. 4.3). We take this property as second criterion, which, however, is less strict than the first criterion, because the distance of $(a/2) = 3.33\text{Å}$ between sites in single planes is substantially larger than the Cu-Cu distance of 2.56Å in elemental copper. For the observed $2a_0 \times 2b_0$ supercell, this second criterion can be fulfilled by full occupation of the A sites, while C must remain empty. Alternatively, simultaneous occupation of neighboring sites can be avoided by short-range order for a statistical occupation of C sites of up to 1/3, provided A sites are empty. In both situations the maximum average occupancy of octahedral sites is 1/4 instead of 1/3 for the $\sqrt{3}a_0 \times \sqrt{3}b_0$ supercell. The experimental occupancies of octahedral planes fulfil these criteria, where the occupancy of Cu1a,c sites in crystal A is close to this limit (Table 4.4). The ordered occupation of one third of the sites in a tetrahedral plane would require the other tetrahedral plane to be empty by the criterion of avoiding distances of 2.1Å, so that filling of tetrahedral Van der Waals gaps would also be restricted to a maximum value of 1/3. The observed $2a_0 \times 2b_0$ supercell, Figure 4 shows that full occupation of sites A and D gives a structure that fulfils both criteria, then leading to the

Table 4.4: Occupancy fraction (Occ.) of intercalation sites of crystal A (100 K) and crystal B (14 K). Solid lines separate Van der Waals gaps; dashed lines separate different plane within one Van der Waals gap. The z coordinate increases from $z = 0$ at the top to $z = 1/3$ at the bottom.

Intercalant (multiplicity)	Coordination	Occ. crystal A	Occ. crystal B
Cu1a (3) / Ta2a (3)	Octahedral	0	0
Cu1c (9) / Ta2c (9)		0.300	0.14
Cu2a (6)	Tetrahedral	0	0
Cu2c (18)		0.22	0.30
Cu2b (6)	Tetrahedral	0.035	0.16
Cu2d (18)		0.404	0.47
Cu1b (9) / Ta2b (9)	Octahedral	0.019	0.09
Cu1d (3) / Ta2d (3)		0.475	0.27
Cu2b (6)	Tetrahedral	0.035	0.16
Cu2d (18)		0.404	0.47
Cu2a (6)	Tetrahedral	0	0
Cu2c (18)		0.22	0.30
Cu1a (3) / Ta2a (3)	Octahedral	0	0
Cu1c (9) / Ta2c (9)		0.300	0.14

Table 4.5: Average occupancy fraction (Occ.) of intercalation sites in independent Van der Waals gaps for crystal A (100K) and crystal B (14K). Solid lines separate Van der Waals gaps; dashed lines separate different plane within one Van der Waals gap. The z coordinate increases from top to bottom.

Intercalants	Coordination	Occ. crystal A	Occ. crystal B
Cu1a,c / Ta2a,c	Octahedral	0.225	0.105
Cu2a,c	Tetrahedral	0.165	0.225
Cu2b,d	Tetrahedral	0.127	0.238
Cu1b,d / Ta2b,d	Octahedral	0.133	0.135

theoretical maximum filling of $1/2$ of the tetrahedral Van der Waals gaps. The maximum average filling for the $2a_0 \times 2b_0$ supercell then becomes $(1/4+1/2)/2 = 0.375$, which is higher than $1/3$ for the $\sqrt{3}a_0 \times \sqrt{3}b_0$ supercell. The experimental filling of $0.225 + 0.238 = 0.463$ of the tetrahedral Van der Waals gap in crystal B is close to this limit of $1/2$ (Table 4.5). However, the symmetry of the $2a_0 \times 2b_0$ supercell imposes additional restrictions on the short-range order. For empty A sites and half of the D sites occupied, fulfilment of both criteria leads to a maximum occupancy of $1/6$ of the C sites and $1/6$ of the B sites (again leading to a maximum filling of $1/2$). It is thus found (Table 4.4) that the second, weaker criterion is not completely fulfilled for the tetrahedral intercalation sites in crystal B, thus leading to a small fraction of the atoms being involved in 3.3 \AA intermetallic contacts.

The octahedral sites (Cu1 or Ta2) have positions fixed by symmetry. The tetrahedral sites are $(0, 0, z)$ for Cu2a,d or $(x, 2x, z)$ for Cu2b,c. The refinable coordinates allow for distortions of the triangular pattern of intercalation sites, as is observed indeed (Table 4.6). Only a small distortion is found for crystal B with composition $\text{Cu}_{0.23}\text{Ta}_{1.06}\text{S}_2$. For crystal A with composition $\text{Cu}_{0.237}\text{TaS}_2$ and a concentration of intercalated atoms in the tetrahedral planes below the theoretical limit, the shortest distance is found to occur between the two sites with lowest occupancy factors. The structure shows that occupied C sites can push atoms at nearby B sites towards empty A sites without penalty, while shifts of the C site would bring an occupied C site close to another occupied site (B or D), thus explaining the observed pattern of distortions (Table 4.6).

Table 4.6: Distances /Å between intercalation sites

Intercalant-intercalant	Crystal A	Crystal B
Cu1a–Cu1c / Ta2a–Ta2c	3.3328 (4)	3.3042 (2)
Cu1c–Cu1c / Ta2c–Ta2c	3.3328 (4)	3.3042 (2)
Cu1b–Cu1d / Ta2b–Ta2d	3.3328 (4)	3.3042 (2)
Cu1b–Cu1b / Ta2b–Ta2b	3.3328 (4)	3.3042 (2)
Cu2a–Cu2c	3.333 (6)	3.304 (7)
	3.376 (7)	3.303 (7)
Cu2c–Cu2c	3.289 (7)	3.306 (7)
	3.376 (7)	3.303 (7)
Cu2b–Cu2d	3.34 (3)	3.304 (8)
Cu2b–Cu2b	3.65 (5)	3.304 (8)
		3.01 (5)
Cu2a–Cu2b	1.97 (4)	2.108 (13)
Cu2b–Cu2c	2.23 (5)	2.078 (14)
Cu2c–Cu2d	2.081 (6)	2.090 (5)

4.5 Conclusions

$6R\text{-Cu}_x\text{Ta}_{1+y}\text{S}_2$ forms an eightfold $2a_0 \times 2b_0 \times 2c_0$ superstructure by partial vacancy ordering within planes of intercalated atoms, while the stacking of TaS_2 layers remains that of the 6R polytype. Intercalation atoms enter the compound at octahedral and tetrahedral sites in alternating Van der Waals gaps between locally closest packed planes of sulfur atoms. Intercalation is inhomogeneous, with average occupancies varying between 0.11 for octahedral sites within one Van der Waals gap and 0.23 for the tetrahedral sites within another Van der Waals gap.

The theoretical maximum concentration of intercalated atoms is $x + y = 1$ for occupation of either octahedral or tetrahedral sites. The experimental filling is much smaller. Partial vacancy order is shown to be governed by the principle of maximum separation between intercalated atoms.

Requiring atoms on octahedral sites to be surrounded by vacant sites leads to a theoretical maximum filling of octahedral Van der Waals gaps equal to $x + y = 1/3$ as found for the $\sqrt{3}a_0 \times \sqrt{3}b_0$ supercell of $\text{Co}_{1/3}\text{NbS}_2$ (Nakayama et al. (2006)). Notably, the maximum of $x + y = 1/2$ for filling of tetrahedral sites is obtained

for the $2a_0 \times 2b_0$ supercell. For $6R\text{-Cu}_x\text{Ta}_{1+y}\text{S}_2$, with alternation of octahedral and tetrahedral Van der Waals gaps, the observed $2a_0 \times 2b_0 \times 2c_0$ supercell allows an average maximum filling of $x + y = 0.375$, slightly higher than the filling of $1/3$ as allowed by the $\sqrt{3}a_0 \times \sqrt{3}b_0$ supercell.

Acknowledgements

Financial support by the Deutsche Forschungsgemeinschaft (DFG) in their priority program SPP1415 is gratefully acknowledged.

Chapter 5

Synthesis, Superstructure and Vacancy-Ordering in $2\text{H-Cu}_x\text{Ta}_{1+y}\text{Se}_2$ (MoS_2 -type and NbS_2 -type)¹

5.1 Abstract

Single crystals of $\text{Cu}_x\text{Ta}_{1+y}\text{Se}_2$ have been grown by chemical vapor transport. Single crystals of different compositions have been obtained at slightly different reaction conditions from mixtures of the reactants of the same nominal composition. It is suggested that different diameters of the ampoules imply different contributions of convection and diffusion to the mass transport, and thus are responsible for different ratios of the amount of Cu, Ta and Se transported. $2\text{H-Cu}_{0.52}\text{TaSe}_2$ ($x = 0.52$, $y = 0$) is formed in the narrower ampoule (diameter 15 mm). The crystal structure is based on the MoS_2 type of stacking of TaSe_2 layers. Partial ordering of Cu over the tetrahedral sites is responsible for a $2a_0 \times 2b_0 \times c_0$ superstructure with hexagonal $P\bar{6}m2$ symmetry ($a_0 = 3.468(1) \text{ \AA}$, $c_0 = 13.568(3) \text{ \AA}$). $2\text{H-Cu}_{0.16}\text{Ta}_{1.08}\text{Se}_2$ ($x = 0.16$, $y = 0.08$) is formed in the wider ampoule (diameter 18 mm). It possesses a NbS_2 -type of stacking. A superstructure is not formed, but the presence of Cu and intercalated Ta in alternating Van der Waals gaps is responsible for the reduction of

¹This Chapter will be submitted as Synthesis, Superstructure and Vacancy-Ordering in $2\text{H-Cu}_x\text{Ta}_{1+y}\text{Se}_2$ (MoS_2 -type and NbS_2 -type). S. I. Ali, S. Mondal, S. Van Smaalen. *Z. Anorg. Allg. Chem.*, (2014).

symmetry from $P6_3/mmc$ to $P\bar{3}m1$ ($a_0 = b_0 = 3.439(2)$ Å, $c_0 = 12.870(2)$ Å). Single crystal are formed towards the hotter side of the ampoules up to a temperature of 895 K in both reactions.

5.2 Introduction

Layered transition metal dichalcogenides are known for their low-dimensional electronic properties, as they may develop charge-density waves (CDWs) and superconductivity at low temperatures (Castro Neto (2001)). Examples of materials that, on cooling, first go through a CDW transition and then become superconducting are $2H\text{-NbSe}_2$, $2H\text{-TaSe}_2$, $2H\text{-TaS}_2$ and $1T\text{-TaS}_2$ (Wilson et al. (1975); Malliakas and Kanatzidis (2013); Du et al. (2000); Kumakura et al. (1996); Li et al. (2013)). Intercalation of ions and neutral molecules into the gap between the layers may enhance the two-dimensional character of the electronic states (Marseglia (1983); Friend and Yoffe (1987); Figueroa et al. (1996)). Intercalation by atoms more directly influences the electronic structure through donation of electrons from these atoms into the valence band on the transition metal atoms. Intercalation by more than a few percent often suppresses the CDW, but it may enhance or even induce the formation of a superconducting state at low temperatures (Moroson et al. (2006); Wagner et al. (2008); Zhu et al. (2009)).

Intercalation has been reported of alkali and transition metal atoms into the Van der Waals gap between the transition-metal-dichalcogenide slabs. The intercalated atoms usually occupy the octahedral or tetrahedral sites between the close-packed layers of chalcogenide atoms, resulting in a maximum filling of one intercalated atom for each metal atom of the slab. Often only partial filling can be achieved, which then opens the possibility of vacancy ordering on the sublattice of intercalated atoms. Examples include $2H\text{-Co}_x\text{NbS}_2$ ($x = 1/3$) that exhibits complete order of the Co atoms on a threefold $\sqrt{3}a_0 \times \sqrt{3}b_0 \times c_0$ superstructure of the $2H\text{-NbS}_2$ polymorph (Nakayama et al. (2006)), $2H\text{-Ag}_{0.6}\text{NbS}_2$ that assumes an incommensurate superstructure by vacancy ordering below $T_c = 124$ K (van der Lee et al. (1991)), and $\beta\text{-Ag}_{0.79}\text{VS}_2$ (1H stacking) with partial vacancy ordering (Ali et al. (2013)). Self-intercalation is another possibility, like the formation of $2H\text{-Ta}_x\text{TaS}_2$ and $2H\text{-Ta}_x\text{TaSe}_2$ (Jellinek (1962); Kadijk et al. (1964); Harbrecht and Kreiner (1989); Huisman et al. (1970)).

Transition metal dichalcogenides feature polymorphism with between one and

four slabs within one period of translation (Wilson et al. (1975); Jellinek (1962)). Different polymorphs are the stable phase at different temperatures, but most polymorphs can be quenched to room temperature (Jellinek (1962)). Intercalation may influence the type of polymorphs that is formed. For example, 2H-Cu_xTaS₂ has been reported to crystallize in NbS₂-type of stacking for small x , while it assumes the MoS₂-type of stacking for larger x (Van Arkel and Crevecoeur (1963); Bohnen (1995)).

Intercalation of 2H-TaSe₂ has been achieved by several methods. Exposure of single crystals of 2H-TaSe₂ to metal vapor in vacuum has resulted in intercalated crystals containing Na, Cs, K, Cl₂, In and Cu (Brauer et al. (2001); König et al. (2012); Papageorgopoulos et al. (1998); Rajora (2006); Kordyuk et al. (2010)). Iron has been intercalated by electrochemical methods and by sintering of Fe with 2H-TaSe₂ (Chen et al. (1992); Dai et al. (1993)). Finally, chemical vapor transport (CVT) in vacuum (Binnewies et al. (2013)) after direct reaction of the elements has produced single crystals of Ni-intercalated and Li-intercalated compounds (Li et al. (2010); Zahurak and Murphy (1987))

Here, we report for the first time the synthesis of copper-intercalated 2H-TaSe₂. Chemical vapor transport is employed to grow single crystals of 2H-Cu_xTa_{1+y}Se₂ for $(x, y) = (0.52, 0)$ and $(0.16, 0.08)$. The two intercalation compounds differ in the amount of intercalated copper but also in their crystal structures, which involve the MoS₂ type of stacking for 2H-Cu_{0.52}TaSe₂ and the NbS₂ type of stacking for 2H-Cu_{0.16}Ta_{1.08}Se₂. Ordering of Cu ions is found on a fourfold $2a_0 \times 2b_0 \times c_0$ superlattice of the 2H-TaSe₂ basic structure.

5.3 Experimental

5.3.1 Synthesis and crystal growth

Cu_xTa_{1+y}Se₂ was synthesized by heating a mixture of the elements corresponding to the composition $x = 0.25$ and $y = 0.20$. Copper (99.99%; Alfa), tantalum (99.97%; Alfa), selenium (99.99%; Alfa) and 3 mg iodine as transport agent were placed in quartz-glass ampoules. The ampoules were purged by argon gas and evacuated until a pressure of 8×10^{-3} mbar.

One ampoule of length 200 mm and diameter 15 mm was heated at 620 °C for 64 hours, yielding a black homogeneous polycrystalline material after cooling. Without opening, this ampoule was placed in a two-zone furnace. Initially both zones were

kept at 990 °C for 154 hours. Subsequently, the temperature of the educt side was reduced to 840 °C. After 19 hours, the ampoule was quenched to room temperature in cold water. Single crystals were found in one-third along of the ampoule towards the hotter zone (batch I). Another ampoule of length 205 mm and diameter 18 mm was heated at 600 °C for 38 hours, yielding a homogeneous polycrystalline material of grey color after cooling. Without opening, this ampoule was heated at 990 °C for 158 hours. Subsequently, the temperature of the educt side was reduced to 800 °C. After 27 hours, the ampoule was quenched to room temperature in an oil bath. Single crystals were found in half of the ampoule towards the hotter zone (batch II).

Inspection under an optical microscope revealed single crystals of hexagonal platelet shape. They were smaller in the first batch than in the second batch, commensurate with the longer growth time for the latter.

Chemical compositions have been determined by electron microprobe experiments with an JEOL JXA-8200 instrument, employing the pure elements as reference materials. For the first batch seven crystals were measured, resulting in compositions with x varying between 0.586(2) and 0.670(2), and with y between 0.015(3) and 0.031(4). For the second batch five crystals were measured, resulting in compositions 0.118(3) to 0.153(1) for x and 0.112(2) to 0.126(2) for y .

5.3.2 X-ray diffraction

Single crystals were selected from both batches and glued to thin glass fibers mounted on copper pins. X-ray diffraction of a crystal of batch I (crystal A) was measured on an Mar345 Imaging plate diffractometer equipped with a rotating anode generator. Diffraction data were collected by ϕ scans of step width of 1.0 deg per image. Different exposure times were used, in order to measure both weak superlattice reflections and strong main reflections. For a detector setting of $2\theta_{\text{offset}} = 0$ deg, 180 images each were measured with exposure times per image of 12 and 96 seconds. For a detector setting of $2\theta_{\text{offset}} = 30$ deg, 360 images each were measured with exposure time of 600 seconds.

X-ray diffraction of a crystal of batch II (crystal B) was measured at beamline F1 of HasyLab (DESY, Hamburg), employing a four-circle kappa diffractometer and a MAR-CCD detector. Diffraction data were collected by ϕ scans and ω scans of step width of 1.0 deg per image for detector settings of $2\theta_{\text{offset}} = 0$ and 30 deg, and employing different off-sets for the crystal orientation. Exposure times of 2 second and 16 second were chosen for the $2\theta_{\text{offset}} = 0$ and 30 deg, respectively.

Indexing and the determination of the integrated intensities of Bragg reflections, including a correction for oblique incidence, were done with the software EVAL15 (Schreurs et al. (2010)). Absorption correction was applied by SADABS (Sheldrick (2008)). Structure refinements were done by JANA2006 (Petricek, V. and Dusek, M. and Palatinus, L. (2006)). Experimental details are given in Table 5.1.

5.3.3 Crystal structure of crystal A of batch I

2H-TaSe₂ of MoS₂ structure type has lattice parameters $a = 3.431 \text{ \AA}$ and $c = 12.737 \text{ \AA}$, with space group of $P6_3/mmc$ (Brixner (1962)). Bragg reflections of crystal A can be separated into a set of main reflections that are indexed with the hexagonal unit cell $a_0 = b_0 = 3.468(1) \text{ \AA}$ and $c_0 = 13.568(3) \text{ \AA}$, and a set of superlattice reflections that define a fourfold, $2a_0 \times 2b_0 \times c_0$ supercell. Structure solution by charge flipping (Palatinus and Chapuis (2007)) applied to the main reflections resulted in coordinates of Ta and Se atoms, that were in agreement with the MoS₂ structure type (Bohnen (1995); Jellinek et al. (1960)) The average structure is well described by the MoS₂ structure type together with a fractional occupancy of the tetrahedral sites in the Van der Waals gaps by Cu. The fit to the diffraction data is given by $R_F(\text{obs}) = 0.0368$, $wR_F(\text{obs}) = 0.1377$ and goodness-of-fit $\text{GoF}(\text{all}) = 9.34$ for the symmetry $P6_3/mmc$. A better fit to the main reflections is obtained by lowering the symmetry to $P\bar{6}m2$. The refinement converged at $R_F(\text{obs}) = 0.0353$, $wR_F(\text{obs}) = 0.0685$ and $\text{GoF}(\text{all}) = 4.09$. Main difference with respect to the higher-symmetric structure is the unequal occupancy of the two crystallographically independent intercalation sites, which would be equivalent by symmetry in $P6_3/mmc$ (Table 5.2). Introduction of intercalants at octahedral sites resulted zero occupation and confirms intercalation exclusively at the tetrahedral sites.

The basic structure has a translationsgleiche subgroup of $P6_3/mmc$ of index 2. The fourfold superstructure has the same isomorphic subgroup $P\bar{6}m2$ as the basic structure, i.e. it is an isomorphic subgroup of index 4 (Wondratschek and Müller (1991)). Each of the six independent atoms in the basic structure gives rise to two crystallographically independent atoms in the supercell, which have been enumerated by appending a letter a or b to the atomic symbol of Table 5.2 (Fig. 5.1). The superstructure was solved by refinement of all independent parameters of twelve crystallographically independent atoms against all reflections. A smooth convergence towards a good fit to the data was found, resulting in $R_F(\text{obs}) = 0.0328$, $wR_F(\text{obs}) = 0.0489$ and $\text{GoF}(\text{all}) = 2.58$. The occupancy of the Cu2a site attained

Table 5.1: Crystallographic data

	Crystal A	Crystal B
Chemical formula	$\text{Cu}_{0.52}\text{TaSe}_2$	$\text{Cu}_{0.16}\text{Ta}_{1.08}\text{Se}_2$
Formula weight (g.mol ⁻¹)	371.78	363.38
Temperature (K)	293	298
Structure type	MoS ₂ -type	NbS ₂ -type
Crystal system	Hexagonal	Trigonal
Space group	$P\bar{6}m2$	$P\bar{3}m1$
a (Å)	6.9353 (14)	3.4394 (16)
c (Å)	13.5681 (32)	12.8697 (20)
V (Å ³)	565.2	131.8
ρ_{calc} (g cm ⁻³)	8.74	9.15
Z	8	2
Crystal size (mm ³)	0.08 × 0.07 × 0.03	0.44 × 0.25 × 0.10
Radiation type	Mo-K α	Synchrotron
Wavelength (Å)	0.71069	0.55999
$[\sin(\theta)/\lambda]_{max}$ (Å ⁻¹)	0.86	1.02
Ranges of indices	$-11 \leq h \leq 11$ $-11 \leq k \leq 11$ $-23 \leq l \leq 23$	$-6 \leq h \leq 6$ $-6 \leq k \leq 3$ $-26 \leq l \leq 26$
Number of reflections		
Measured / unique	16282 / 1251	4276 / 507
Observed [$I > 3\sigma(I)$]	1180	470
R_{int}	0.0521	0.0510
R_F / wR_F [$F > 3\sigma(F)$]		
All reflections	0.0328 / 0.0489	0.0578 / 0.0651
Main reflections	0.0332 / 0.0585	-
Superlattice reflections	0.0322 / 0.0431	-
GoF (all)	2.58	3.81

Table 5.2: Basic structure of $\text{Cu}_{0.52}\text{TaSe}_2$ (crystal A). Coordinates are given with respect to the basic-structure unit cell with $a_0 = 3.468(1)$ and $c_0 = 13.568(3)$ Å and space group $P\bar{6}m2$. Occ denotes the site occupation fraction. Standard uncertainties are given in parentheses.

Atom	x	y	z	U_{iso}^{eq}	Occ
Ta1	0.0	0.0	1/2	0.0092 (2)	1
Ta2	2/3	1/3	0	0.0096 (2)	1
Se1	2/3	1/3	0.3762 (1)	0.0121 (3)	1
Se2	0.0	0.0	0.1205 (1)	0.0088 (3)	1
Cu1	2/3	1/3	0.2124 (8)	0.0222 (20)	0.345 (17)
Cu2	0	0	0.2845 (7)	0.0217 (24)	0.204 (17)

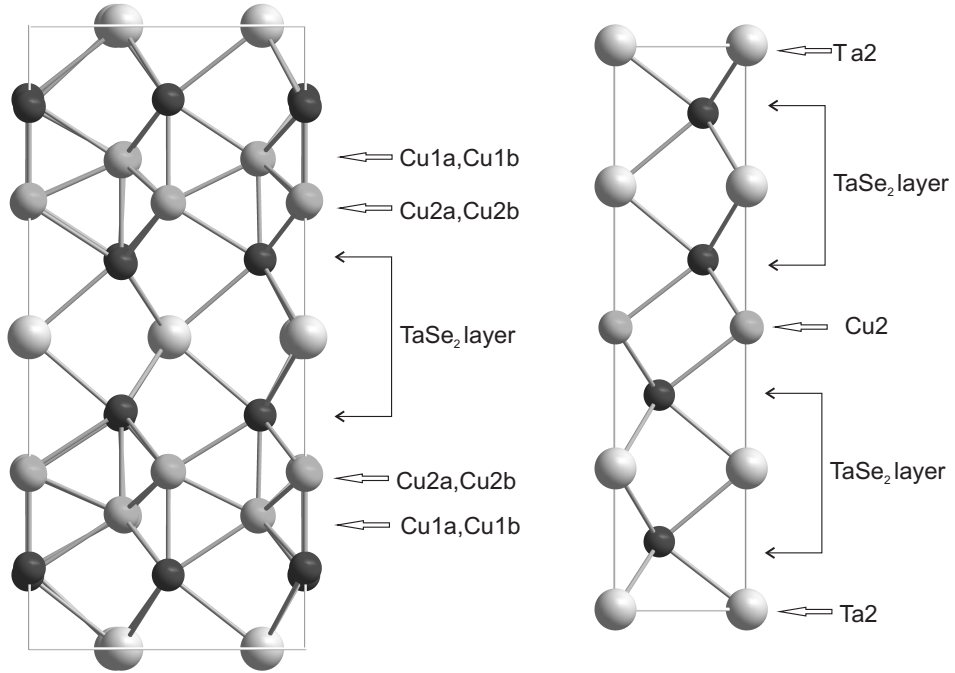


Figure 5.1: Projections along \mathbf{b}^* of the crystal structures of (a) $2\text{H-Cu}_{0.52}\text{TaSe}_2$ (MoS₂-type) and (b) $2\text{H-Cu}_{0.16}\text{Ta}_{1.08}\text{Se}_2$ (NbS₂-type).

Table 5.3: Occupation fraction (Occ) and average occupancy (Avg. Occ) of the Cu sites of 2H-Cu_{0.52}TaSe₂. Solid lines separate Van der Waals gaps; dashed lines separate different planes of tetrahedral sites within one Van der Waals gap.

Site (multiplicity)	Coordination	Occ	Avg. Occ
Cu1a (2)		0.597 (13)	
	Tetrahedral		0.296 (12)
Cu1b (6)		0.196 (12)	
Cu2a (2)		0	
	Tetrahedral		0.222 (6)
Cu2b (6)		0.296 (8)	
Cu2a (2)		0	
	Tetrahedral		0.222 (6)
Cu2b (6)		0.296 (8)	
Cu1a (6)		0.597 (13)	
	Tetrahedral		0.296 (12)
Cu1b (2)		0.196 (12)	

a small negative value in this structure model. Therefore, this occupancy was set to zero for the final refinement. An excellent fit to the diffraction data was then obtained (Table 5.1). In particular, the fit to the main reflections is better than the fit provided by the basic structure. (Compare the partial R_F value for main reflections of 0.0332 with $R_F(\text{obs}) = 0.0353$ obtained for the refinement of the basic structure.)

The fractional occupancies of the Cu sites in the final structure model have been used for the computation of the chemical composition as Cu_{0.52}TaSe₂ (Table 5.3). Full details of the superstructure are provided in the supplementary material.

5.3.4 Crystal structure of crystal B of batch II

2H-TaSe₂ of NbS₂ structure type has lattice parameters $a = 3.424 \text{ \AA}$ and $c = 12.685 \text{ \AA}$, with space group $P6_3/mmc$ (Patel et al. (2009); Bjerkelund and Kjekshus (1967)). All Bragg reflections of crystal B could be indexed on a lattice with $a = 3.439(2)$ and $c = 12.870(2) \text{ \AA}$. Superlattice reflections were not observed. Structure solution using superflip (Palatinus and Chapuis (2007)) gives the positions of Ta and Se.

Table 5.4: Basic structure of $\text{Cu}_{0.16}\text{Ta}_{1.08}\text{Se}_2$ (crystal B). Occ denotes the occupation fractional. Standard uncertainties in the last digit are given in parentheses.

Atom	x	y	z	U_{iso}^{eq}	Occ
Ta1	0.0	0.0	0.2500 (1)	0.0088 (1)	1
Se1	2/3	1/3	0.1201 (1)	0.0085 (2)	1
Se2	2/3	1/3	0.3800 (1)	0.0086 (2)	1
Ta2	0.0	0.0	0.0	0.0112 (9)	0.161 (8)
Cu2	0	0	0.5	0.0315 (28)	0.317 (26)

They are equal to the positions reported for 2H-TaSe₂ of NbS₂ structure type (Patel et al. (2009); Bjerkelund and Kjekshus (1967)). Intercalated copper and additional tantalum atoms are at partially occupied octahedral sites in the Van der Waals gaps. The best fit to the diffraction data was obtained by lowering the symmetry to $P\bar{3}m1$ [$R_F(\text{obs}) = 0.0578$, $wR_F(\text{obs}) = 0.0651$, $\text{GoF}(\text{all}) = 3.81$]. Different intercalation in alternating Van der Waals gaps has been found to be responsible for the lowering of symmetry from $P6_3/mmc$ to $P\bar{3}m1$. Inversion twinning has been found with a ratio of approximately 1 : 1. The chemical composition of $\text{Cu}_{0.16}\text{Ta}_{1.08}\text{Se}_2$ has been computed on the basis of the refined fractional occupancies of the Cu2 and Ta2 sites (Fig. 5.1). A reasonable fit to the diffraction data was also obtained for a structure model involving Cu on the Ta2 position and Ta on the Cu2 position [$R_F(\text{obs}) = 0.0585$, $wR_F(\text{obs}) = 0.0671$, $\text{GoF}(\text{all}) = 3.97$]. Assuming Cu as the only intercalant on all octahedral sites resulted in $R_F(\text{obs}) = 0.0591$, $wR_F(\text{obs}) = 0.0715$ and $\text{GoF}(\text{all}) = 4.23$. Assuming Ta as the only intercalant gives $R_F(\text{obs}) = 0.0595$, $wR_F(\text{obs}) = 0.0714$, $\text{GoF}(\text{all}) = 4.22$. Using hexagonal symmetry $P6_3/mmc$ and copper as the only intercalant resulted $R_F(\text{obs}) = 0.0644$, $wR_F(\text{obs}) = 0.0871$, $\text{GoF}(\text{all}) = 6.07$. The composition $\text{Cu}_{0.16}\text{Ta}_{1.08}\text{Se}_2$ is in fair agreement with the compositions of different crystals of the same batch, as they have been determined by electron microprobe experiments (Sections 5.3.1)

5.4 Discussion

The nominal composition is the same for batch I and II. However, different amounts of intercalated atoms have been found in single crystals extracted from the two batches, corresponding to compositions $\text{Cu}_{0.52}\text{TaSe}_2$ for batch I and $\text{Cu}_{0.16}\text{Ta}_{1.08}\text{Se}_2$

for batch II. These different compositions are in fair agreement with compositions determined by electron microprobe measurements (Sections 5.3.1). They will have been related to the different reaction conditions. In particular, the relative contributions of convection and diffusion to the mass transport will have depended on the different diameters of the ampoules and the different temperature gradients as used for growing crystals in the two batches (Section 5.3.1). This, in turn, might have lead to a different ratio of the amounts of transported Cu, Ta and Se, thus explaining the different compositions of the single crystals.

The compounds $2\text{H-Cu}_{0.52}\text{TaSe}_2$ and $2\text{H-Cu}_{0.16}\text{Ta}_{1.08}\text{Se}_2$ possess different structure types, *i.e.* they have stackings of TaSe_2 layers according to the MoS_2 and NbS_2 structure types, respectively (Sections 5.3.3 and 5.3.4). Although we do not have a definitive explanation for this difference, we do note that intercalated atoms are—on the average—farther away from the Ta atoms in the MoS_2 structure type than in the NbS_2 structure type. Since Coulomb repulsions are more important at higher fillings of the Van der Waals gap, this would explain why $2\text{H-Cu}_{0.52}\text{TaSe}_2$ possess the MoS_2 structure type, although this corresponds to a stacking of layers that is less favorable for pristine 2H-TaSe_2 . This interpretation is supported by the fact that the same two structure types have been found for $2\text{H-Cu}_x\text{TaS}_2$ at similar compositions (Van Arkel and Crevecoeur (1963); Bohnen (1995)).

The symmetries of both structure types of 2H-TaSe_2 are $P6_3/mmc$ (Brixner (1962); Bjerkelund and Kjekshus (1967)). The lower symmetries of the intercalated compounds is mainly related to unequal occupancies of different intercalated sites (Tables 5.3 and 5.4). Structural distortions (relative shifts of the atoms) are absent in $2\text{H-Cu}_{0.16}\text{Ta}_{1.08}\text{Se}_2$ and very small in $2\text{H-Cu}_{0.52}\text{TaSe}_2$. Instead, intercalation is expressed by a significant increase of the interlayer distance (c lattice parameter) by 0.185 Å for $2\text{H-Cu}_{0.16}\text{Ta}_{1.08}\text{Se}_2$ and by 0.83 Å for $2\text{H-Cu}_{0.52}\text{TaSe}_2$ as compared to 2H-TaSe_2 .

The fourfold superstructure of $2\text{H-Cu}_{0.52}\text{TaSe}_2$ is the result of partial vacancy ordering over the tetrahedral sites within the Van der Waals gaps (Table 5.3 and Fig. 5.2). The superstructure allows for a relaxation of the environments of the Cu atoms, as can be observed from the Cu–Se distances and the computed valencies (Table 5.5). The shortest Cu–Se distance, the highest valence and thus tightest environment is found for the empty site Cu2a, for which short distances are of no consequence. The observed tightness of the environment decreases upon increasing site occupancy factor, thus expressing the relaxation around the intercalation sites. The longest distances are close to the distance of 2.40 (2) Å between monovalent

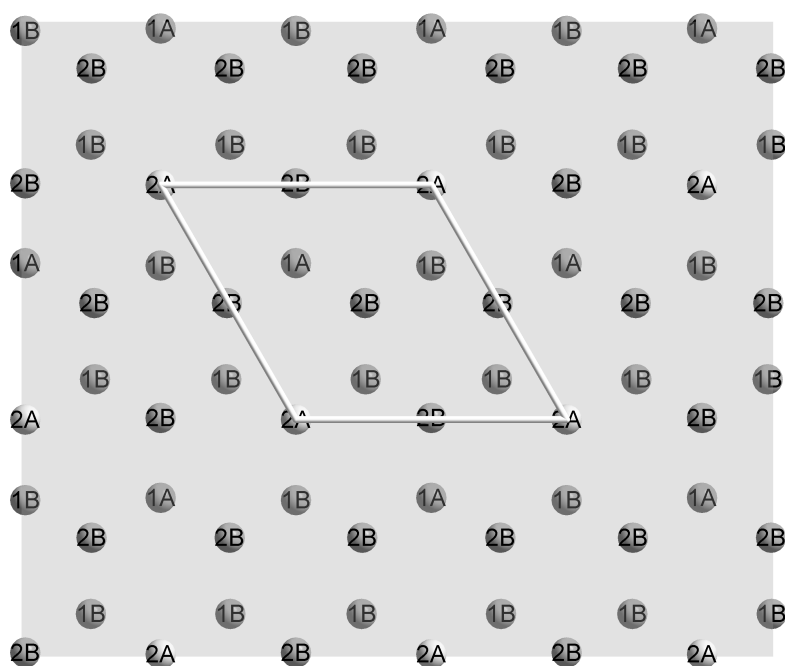


Figure 5.2: Double plane of intercalation sites Cu1 and Cu2 of $2\text{H-Cu}_{0.52}\text{TaSe}_2$. 1A = Cu1a and 1B = Cu1b are in one plane at $z \approx 0.21$, 2A = Cu2a and 2B = Cu2b are in the other plane at $z \approx 0.28$.

Table 5.5: Environment of the intercalation sites in the superstructure of $2H\text{-Cu}_{0.52}\text{TaSe}_2$. Atomic valences V have been obtained by the bond-valence method, Brown and Altermatt (1985) employing $R_0(\text{Cu-Se}) = 2.02 \text{ \AA}$. The site occupation fraction (Occ.) corresponds to Table 5.3. Distances between the site and the four neighboring Se atoms are given in Ångstrom.

Site	Occ	V	Cu-Se distance (Å)
Cu2a	0	2.16	(3×) 2.351 (1); (1×) 2.045 (1)
Cu1b	0.20	1.86	(1×) 2.356 (10); (2×) 2.343; (1×) 2.193 (10)
Cu2b	0.30	1.69	(1×) 2.251 (3); (2×) 2.348 (4); (1×) 2.435 (4)
Cu1a	0.58	1.53	(3×) 2.432 (2); (1×) 2.245 (4)

Table 5.6: Selected interatomic distances (Å) in the superstructure of $2H\text{-Cu}_{0.52}\text{TaSe}_2$

Atoms	Distance
Ta1a - Se2a	(6×) 2.599 (1)
Ta1b - Se2a	(4×) 2.605 (1)
Ta1b - Se2b	(2×) 2.635 (2)
Ta2a - Se1a	(2×) 2.575 (1)
Ta2a - Se1b	(4×) 2.604 (1)
Ta2b - Se1b	(6×) 2.593 (1)
Cu1b - Cu2a	(1×) 2.253 (10)
Cu1b - Cu2b	(2×) 2.175 (11)
Cu1a - Cu2b	(3×) 2.241 (4)

Cu and Se, as reported in the literature (Gulay et al. (2011); Berry (1954)). The displacements of the Se atoms have but a small influence on the Ta-Se distances, the latter which differ only slightly from the ideal value of 2.59 \AA as reported for $2H\text{-TaSe}_2$ (Table 5.6) (Brown and Beerntsen (1965)).

The crystal structure of $2H\text{-Cu}_{0.16}\text{Ta}_{1.08}\text{Se}_2$ comprises of a NbS_2 -type stacking of layers TaSe_2 , with Cu and Ta intercalated at octahedral sites in alternating Van der Waals gaps (Table 5.4 and Fig. 5.1). The absence of a superstructure can be nicely explained by the low concentration of intercalated atoms. The fully ordered crystal structure of $\text{Co}_{1/3}\text{NbS}_2$ on a $\sqrt{3}a_0 \times \sqrt{3}b_0$ supercell shows that an occupancy of $1/3$ is the maximum filling of the Van der Waals gaps at which each atom has vacant intercalation sites as nearest neighbors (Nakayama et al. (2006)). Higher occupancies x than this critical value of $x_{c1} = 1/3$ would require a different superstructure

and structural distortions in order to prevent unfavorable Cu–Cu contacts, as it is presently found for 2H-Cu_{0.52}TaSe₂. Lower concentrations do not require ordering of the intercalated atoms, while—on the average—each occupied site can still be surrounded by empty intercalation sites. For 2H-Cu_{0.16}Ta_{1.08}Se₂ the concentration of intercalated species is lower than the critical value of 1/3 (Table 5.4), thus explaining the absence of a superstructure.

5.5 Conclusions

Single crystals of Copper-intercalated TaSe₂ has been successfully synthesized for the first time. Crystals form towards the hotter zone of the ampoule up to a temperature of $T = 895$ K (Section 5.3.1). Depending on the subtle differences in the method of crystal growth, two different compounds have been obtained. 2H-Cu_{0.16}Ta_{1.08}Se₂ contains intercalated Cu and intercalated Ta in alternating Van der Waals gaps. The relatively small amounts of intercalate species explains the absence of superstructure formation, and it explains the preservation of the NbS₂ type of layer stacking as it also is found for pristine 2H-TaSe₂ (Section 5.3.4). 2H-Cu_{0.52}TaSe₂ forms a fourfold superstructure of the MoS₂ type of layer stacking. The switch of structure type may be the result of avoiding relatively close Cu–Ta contacts, while the formation of the superstructure is explained by the optimization of Cu–Cu contacts within single Van der Waals gaps. The different structure types for the two different compounds are consistent with the homogeneity ranges of these structure types as previously be established of Cu_{*x*}TaS₂ (Van Arkel and Crevecoeur (1963); Bohnen (1995)).

Acknowledgements

Single crystals were grown with assistance of Alfred Suttner at the Laboratory of Crystallography. The electron microprobe experiment was performed by Detlef Krause and Hubertat Schulze at the Bavarian Geoinstitute (BGI) in Bayreuth. Financial support was obtained from the German Science Foundation (DFG).

Chapter 6

Synthesis, single crystal X-ray structure of Cu_3TaSe_4 and comparative studies with other Cu_3MX_4 ($\text{M} = \text{V}, \text{Nb}, \text{Ta}; \text{X} = \text{S}, \text{Se}, \text{Te}$)¹

6.1 Abstract

Single crystals of Cu_3TaSe_4 were obtained by chemical vapor transport with iodine as transport agent. Cu_3TaSe_4 crystallizes in the sylvanite structure type with space group $P43m$ and $a=5.6613(3)$ Å at room temperature. Structure refinements against single crystal X-ray diffraction data result in a Cu-Se distance slightly longer than the Ta-Se distance, whereas previous Rietveld refinements obtained a Cu-Se distance shorter than the Ta-Se distance [G.E. Delgado et al., *J. Alloys Comp.* 439, 346 (2007)]. The structural variations of sylvanite type compounds Cu_3MX_4 ($\text{M} = \text{V}, \text{Nb}, \text{Ta}; \text{X} = \text{S}, \text{Se}, \text{Te}$) are discussed in view of small distortions of CuX_4 and MX_4 tetrahedra and the atomic valences.

¹This Chapter has been published as Synthesis, single crystal X-ray structure of Cu_3TaSe_4 and comparative studies with other Cu_3MX_4 ($\text{M} = \text{V}, \text{Nb}, \text{Ta}; \text{X} = \text{S}, \text{Se}, \text{Te}$). S. I. Ali, S. Van Smaalen. *Z. Anorg. Allg. Chem.*, **640**, 931-934, (2014).

6.2 Introduction

Sulvanite-type of compounds Cu_3MX_4 ($\text{M} = \text{V}, \text{Nb}, \text{Ta}$; $\text{X} = \text{S}, \text{Se}, \text{Te}$) are interesting materials due to their electronic structure and electro-optic properties (Nitsche and Wild (1967); Osorio-Guillén and Espinosa-García (2012); Espinosa-García et al. (2011)). The crystal structures of several of these compounds have been previously established by means of X-ray diffraction (Delgado et al. (2007); Trojer (1966); Kars et al. (2005); Delgado et al. (2011); Klepp and Gurtner (2000); Lu and Ibers (1993)). They are cubic with space group $P\bar{4}3m$. The crystal structures are completely characterized by the lattice parameter $a \approx 5.6 \text{ \AA}$ and a single coordinate x describing the position (x, x, x) of the X atom. The ideal sulvanite structure has $x = 1/4$, implying equal bond lengths $d(\text{M-X}) = d(\text{Cu-X}) = (\sqrt{3}/4)a$. For $x > 1/4$, both bonds become longer and $d(\text{M-X}) > d(\text{Cu-X})$. For $x < 1/4$, both bonds become shorter and $d(\text{M-X}) < d(\text{Cu-X})$. Recently, calculated electronic structures of the Cu_3MS_4 ($\text{M} = \text{V}, \text{Nb}, \text{Ta}$) have shown that these compounds are semiconductors with an indirect band gap (Osorio-Guillén and Espinosa-García (2012)).

A variety of synthetic methods has been employed for the synthesis Cu_3TaSe_4 . Initially, Cu_3TaSe_4 was prepared by sintering elements together at temperature gradient 873 / 1073 K, resulting in a microcrystalline powder. Only the lattice parameter was determined from X-ray diffraction (Hulliger (1961)). More recently, the same compound was prepared by heating a mixture of the elements at 623 K (Van Arkel and Crevecoeur (1963)). Single crystals of Cu_3TaSe_4 were first introduced by means of iodine vapor transport method in a temperature gradient of 873 / 1073 K (Nitsche and Wild (1967)). The single crystals of prismatic shapes and dimensions up to $1 \times 1 \times 3 \text{ mm}^3$ were used for the measurement of the refractive index, optical transmission and electro-optical effect, but not for X-ray diffraction. (Nitsche and Wild (1967)) A few years ago, the crystal structure of Cu_3TaSe_4 has been reported on the basis of X-ray powder diffraction (Delgado et al. (2007)). The latter work appears to be the only refinement of the crystal structure of Cu_3TaSe_4 published up to the present date.

Herein we report the successful synthesis of single crystals of Cu_3TaSe_4 . Single-crystal X-ray diffraction confirms the sulvanite structure type, but we find a small distortion out of the idealized crystal structure, which is of opposite sign than the distortion reported on the basis of X-ray powder diffraction that is of opposite sign than the the distortion reported on the basis of X-ray powder diffraction (Delgado et al. (2007)). We discuss distortions of Cu_3MX_4 ($\text{M} = \text{V}, \text{Nb}, \text{Ta}$; $\text{X} = \text{S}, \text{Se}, \text{Te}$)

in relation to their chemical compositions.

6.3 Experimental Section

6.3.1 Preparation of polycrystalline sample

The title compound was obtained during an attempt to synthesize copper-intercalated TaSe₂. In the first step the starting materials [Cu (99.99%, Alfa), Ta (99.97%, Alfa) and Se (99.99%, Alfa)] were mixed (Cu : Ta : Se = 0.21 : 1.15 : 2) in a quartz ampoule with a length of 205 mm and inner diameter of 20 mm. The ampoule was evacuated and purged by argon gas till the vacuum reach to 8×10^{-3} mbar. The sealed ampoule was placed in a two-zone furnace with temperature gradient of 1153 / 1193K for 52 h. Subsequently, the temperatures of both ends of the furnace were kept at 1153 K for 98 h. The result was a black polycrystalline powder that appeared homogenous under visual inspection, and that was grinded for further use.

6.3.2 Crystal growth

A quartz-glass ampoule with a length of 205 mm and inner diameter of 15 mm was filled with a mixture of polycrystalline powder (300 mg, Section 6.3.1), iodine (5 mg) and selenium (50 mg). The sealed evacuated ampoule was placed in a two zone furnace and kept at temperature gradient of 1163 / 1173 K for 15 h and subsequently at temperature gradient of 1163 K (starting compound) / 1073 K (product) for 5 d and 8 h. Finally we quenched the ampoule to the room temperature in oil bath. The ampoule appeared to contain two kinds of single crystals. Single crystals of Cu₃TaSe₄ were obtained at the colder (1073K) zone, and 1T-TaSe₂ was found at the hotter zone (1163K). An inhomogeneous chemical reaction is not an unusual. For example Li et al. (Li et al. (1995)) have reported the formation of both ternary (Cu₃TaTe₄) and quaternary (RbCu₂TaTe₄) compounds in a single batch of synthesis.

Inspection under an optical microscope has revealed that all crystals of Cu₃TaSe₄ show a cubic morphology and an orange yellow color (Fig. 6.1). The study by Nitsche et al. (Nitsche and Wild (1967)) reported a similar orange yellow color for crystals formed in the colder zone of ampoule.

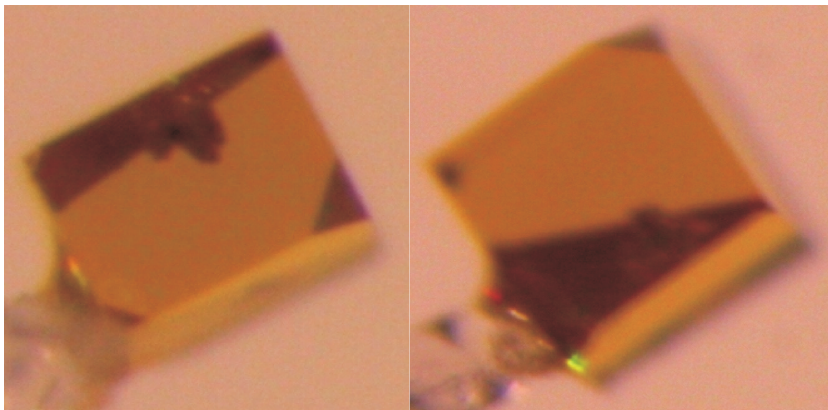


Figure 6.1: Two views of the single crystal of Cu_3TaSe_4 as employed for X-ray diffraction (Table 6.1).

6.3.3 X-ray diffraction experiment

A crystal of dimension $0.15 \times 0.14 \times 0.13 \text{ mm}^3$ was glued to a thin glass fiber for the X-ray diffraction experiments. A Mar345 Imaging plate diffractometer was used for measuring the diffracted intensity in a series of ϕ scans with a step-width of 0.5° . Two runs were measured with detector positions of $2\theta_{\text{offset}} = 0^\circ$, $2\theta_{\text{offset}} = 30^\circ$, respectively. Indexing and data integration, including the application of a correction for oblique incidence, were done with software package EVAL14 (Schreurs et al. (2010)). All diffraction maxima could be indexed on the basis of a primitive cubic lattice. Absorption correction was applied by the computer program SADABS (Sheldrick (2008)). Structure refinements were done by JANA2006 (Petricek, V. and Dusek, M. and Palatinus, L. (2006)). The initial model for the structure refinement was taken from Delgado et al. (Delgado et al. (2007)). Experimental data and crystallographic information of the structure are summarized in Table 6.1.

6.4 Results and discussion

We have successfully refined the sylvanite structure type against single-crystal X-ray diffraction data measured on Cu_3TaSe_4 . The high accuracy of the resulting structure model is demonstrated by the low R values on the extensive data set (Table 6.1) as well as by the small standard uncertainty (s.u.) of the single refinable atomic coordinate $x[\text{Se}] = 0.24899(3)$ (Table 6.2).

Table 6.1: Crystallographic data for Cu_3TaSe_4

	Cu_3TaSe_4
Temperature /K	298 K
Formula weight /g.mol ⁻¹	687.43
Crystal system	cubic
Space group	$P\bar{4}3m$
a /Å	5.6613 (3)
V /Å ³	181.45 (2)
ρ_{calc} /g cm ⁻³	6.2891
Z	1
Crystal size /mm ³	0.15 × 0.14 × 0.13
Radiation	Ag-K α
Wave length /Å	0.5608
$(\sin\theta/\lambda)_{max}$ / (Å) ⁻¹	1.08
Indices range	-12 ≤ h ≤ 12 -12 ≤ k ≤ 12 -7 ≤ l ≤ 7
Measured / unique reflection	10933 / 413
Observed [$I > 3\sigma(I)$] reflections	408
R_{int}	0.034
R_F / wR_F [$F > 3\sigma(F)$]	0.0121 / 0.0145
GoF (obs/all)	1.28 / 1.28

Table 6.2: Crystal structures of Cu_3MX_4 ($M = \text{V}, \text{Nb}, \text{Ta}; X = \text{S}, \text{Se}, \text{Te}$). X atoms are at (x, x, x) . $d[\text{X-X}]$ is the diameter of the channel; $d[\text{Cu-X}]^* = d[\text{M-X}]^*$ are distances in the idealized structure with $x = 1/4$. # indicates present study. Atomic valences V have been obtained with the bond-valence method (Brown and Altermatt (1985)), employing $R_0(\text{Cu-Se}) = 2.02\text{\AA}$, $R_0(\text{Ta-Se}) = 2.51\text{\AA}$, $R_0(\text{V-Se}) = 2.33\text{\AA}$, $R_0(\text{Nb-Se}) = 2.51\text{\AA}$, $R_0(\text{Cu-S}) = 1.86\text{\AA}$, $R_0(\text{Cu-Te}) = 2.27\text{\AA}$, $R_0(\text{Ta-S}) = 2.39\text{\AA}$, $R_0(\text{Ta-Te}) = 2.70\text{\AA}$, and $b = 0.37\text{\AA}$ (Brese and O’Keeffe (1991)). References of the ternary compounds are following: Cu_3VSe_4 (Klepp and Gurtner (2000)); Cu_3NbSe_4 (Lu and Ibers (1993)); Cu_3TaSe_4 (Delgado et al. (2007)); Cu_3TaS_4 (Delgado et al. (2011)); Cu_3TaTe_4 (Li et al. (1995))

	Cu_3VSe_4	Cu_3NbSe_4	Cu_3TaSe_4 (#)	Cu_3TaSe_4	Cu_3TaS_4	Cu_3TaTe_4
X-ray method	Single crystal	Single crystal	Single crystal	Powder	Powder	Single crystal
R_F or R_P	3.1%	2.1%	1.2%	12.2%	4.4%	2.4%
$(\text{Sin}\theta/\lambda)_{\text{max}} / (\text{\AA})^{-1}$	0.7	0.7	1.08	0.5	0.5	0.64
x	0.2554 (2)	0.25021 (5)	0.24899 (3)	0.2510 (5)	0.2475 (5)	0.2580 (1)
$a / \text{\AA}$	5.5636 (5)	5.638 (1)	5.6613 (3)	5.6600 (1)	5.5145 (1)	5.930 (2)
Volume / \AA^3	172.21 (3)	179.22 (6)	181.44 (2)	181.32 (2)	167.70 (1)	208.5 (1)
$d[\text{Cu-X}] / \text{\AA}$	2.392 (1)	2.442 (1)	2.4481 (2)	2.454 (3)	2.380 (1)	2.596 (1)
$d[\text{M-X}] / \text{\AA}$	2.357 (1)	2.443 (1)	2.4415 (2)	2.461 (3)	2.364 (1)	2.650 (1)
$d[\text{X-X}] / \text{\AA}$	3.8491	3.9833	4.019	3.986	3.9383	4.0589
$d[\text{Cu-X}]^* =$	2.4091	2.4413	2.4514	2.4509	2.3878	2.5678
$d[\text{M-X}]^* / \text{\AA}$						
$V(\text{Cu})$	1.46	1.28	1.26	1.24	0.98	1.24
$V(\text{M})$	3.72	4.28	1.26	4.57	4.29	4.58
$V(\text{X})$	2.03	2.03	2.15	2.07	1.81	2.08

A small but significant difference is found as compared to the previous study on Cu_3TaSe_4 , which employed X-ray powder diffraction, and arrived at a value of 0.2510(5) for $x[\text{Se}]$ (Table 6.2) (Delgado et al. (2007)). We believe that the present value is more accurate, not only for the smaller s.u. but also because the analysis on X-ray powder diffraction data employed a single isotropic ADP for all atoms (Delgado et al. (2007)), while the present analysis refined anisotropic ADPs (Supporting information).

The sulvanite structure can be considered as a three-dimensional packing of edge-sharing CuX_4 and MX_4 tetrahedra (Fig. 6.2). The X atom is in fourfold coordination by the metal atoms. Three Cu atoms occupy three corners of a tetrahedron, while Ta is at a position that is related to the fourth corner of this tetrahedron through application of an inversion operator located on the X atom. The detailed structure depends on the value of the single atomic coordinate x describing the position of the chalcogen atom at (x, x, x) . The ideal sulvanite structure type has $x = 1/4$. Then, distances Cu-X and M-X in Cu_3MX_4 are equal to each other and denoted by an asterisk (Table 6.2). For a given value of the lattice parameter and $x > 1/4$, both bonds are longer and the diameter [$d[\text{X-X}] = (1-2x)\sqrt{2}a$] of the channels is smaller than in the ideal structure, with $d(\text{M-X}) > d(\text{Cu-X})$. For $x < 1/4$, both bonds are shorter and $d[\text{X-X}]$ is longer than in the ideal structure, with $d(\text{M-X}) < d(\text{Cu-X})$. It appears that X-X distances possess similar values in the different selenides as well as in the sulfide and telluride. Together with the large value of about 4 Å this implies the absence of direct interactions between chalcogen atoms. The lattice parameter agrees well with that determined from powder diffraction (Delgado et al. (2007)) (Table 6.2). The refined value of $x[\text{Se}] < 1/4$ implies that we presently find a Ta-Se distance very close to the Nb-Se distance in Cu_3NbSe_4 (Lu and Ibers (1993)) and in better agreement with equal ionic radii (Shannon (1976)) of Ta^{5+} and Nb^{5+} than $d(\text{Ta-Se})$ obtained in (Delgado et al. (2007)). Observed lattice parameters increase for the series V-Nb-Ta and $d[\text{Cu-X}]$ increases accordingly (Table 6.2). The presently observed value of $x[\text{Se}] < 1/4$ implies that $d[\text{Cu-Se}]$ is smaller than in an ideal sulvanite structure with the same lattice parameter, and closer to the value found in Cu_3NbSe_4 .

The bond lengths $d(\text{Cu-X})$ and $d(\text{M-X})$ are shorter than the sum of their atomic radii (Shannon (1976)) (Table 6.2). This feature indicates that the sulvanite structures are strained. Short bonding distances imply a smaller diameter of the channels than would be present for longer bonds. Likely, the gain of Free Energy through higher packing density (smaller diameter of the channels) is responsible

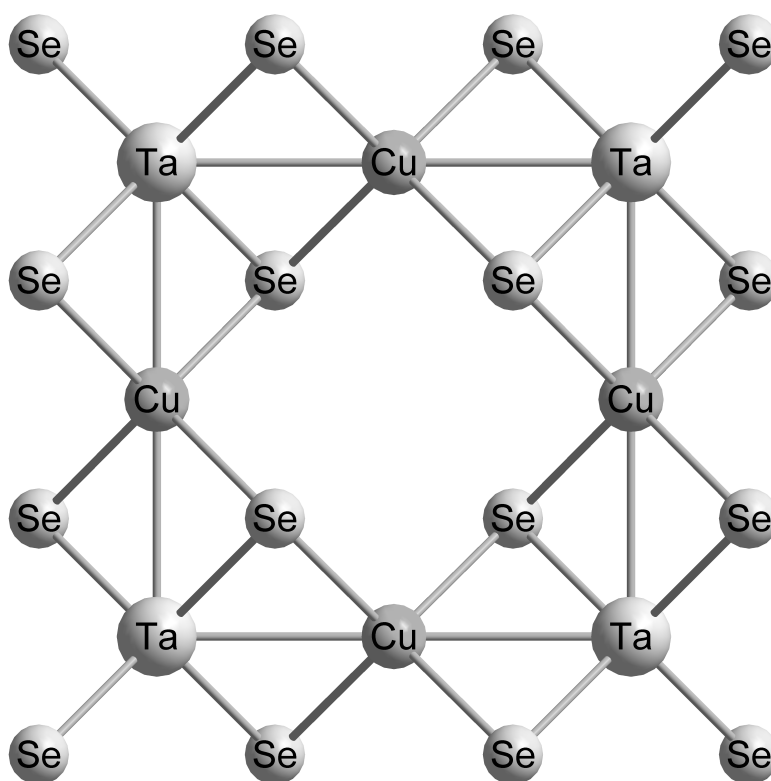


Figure 6.2: Crystal structure of Cu_3TaSe_4 projected along c -axis. Cu is at 3d: $(1/2 0 0)$, Ta is at 1a: $(0 0 0)$ and Se is at 4e: (x, x, x) , where $x \approx 1/4$.

for these short distances. The bond-valence method (BVS) has been used to compute atomic valences from the crystal structures (Brown and Altermatt (1985); Li et al. (1995))(Table 6.2). Formal valences of Cu_3MX_4 are Cu^{1+} and M^{5+} and X^{2-} . The computed valences are in reasonable agreement with these values, with slightly overbonded Cu cations and chalcogenide anions and underbonded M cations, thus illustrating strained character of the crystal structures. While keeping channels of equal diameter, the smaller S^{2-} ions result in underbonded atoms in Cu_3TaS_4 . On the other hand, the small V cations are responsible for a shrinkage of the lattice parameter, then leading to a mixed valence state of 1.5 of Cu and a valence state of V closer to 4+ than 5+. Bond lengths of similar magnitudes have been found in $\text{RbCu}_2\text{TaSe}_4$ and $\text{Rb}_2\text{CuTaSe}_4$, where Cu and Ta are also tetrahedrally coordinated with Se (Wu et al. (2004)). Cu-Se distances in Cu_3MSe_4 are very much consistent with the Cu-Se distances of CuSe_4 tetrahedron in both Cu_2Se (Gulay et al. (2011)) and Cu_2SnSe_3 (Delgado et al. (2003)) compounds.

6.5 Conclusion

Single crystals of Cu_3TaSe_4 have been grown by chemical vapour transport. An accurate crystal structure of this compound has been determined against single-crystal X-ray diffraction data. With respect to the previous structure refinement against X-ray powder diffraction (Delgado et al. (2007)), principal difference is the present refinement of anisotropic ADPs. Consequence of the improved description of thermal motion is a structure model that is in better agreement with the crystal chemical properties of Cu_3NbSe_4 and other related sylvanite compounds.

Acknowledgements

Single crystals were grown in Bayreuth with assistance of Alfred Suttner. Financial support by the Deutsche Forschungsgemeinschaft (DFG) is gratefully acknowledged.

Chapter 7

Summary

In this thesis, the synthesis and crystal structures are discussed of intercalated transition metal dichalcogenides (TMDCs) $6R-Cu_xTa_{1+y}S_2$ and $2H-Cu_xTa_{1+y}Se_2$, as well as the compound Cu_3TaSe_4 . Synthesis of these compounds has been performed by the method of chemical vapor transport, using iodine as a transporting agent. X-ray diffraction may reveal superlattice reflections, which then indicates the existence of a superstructure. An eightfold superstructure has been found for $6R-Cu_xTa_{1+y}S_2$ ($x = 0.237$, $y = 0$; $x = 0.23$, $y = 0.06$) and a fourfold superstructure has been found for $2H-Cu_{0.52}TaSe_2$. $2H-Cu_{0.16}Ta_{1.08}Se_2$ and Cu_3TaSe_4 do not form any superstructure.

$6R-Cu_xTa_{1+y}S_2$ compounds have been investigated by X-ray diffraction at different temperatures. $6R-Cu_xTa_{1+y}S_2$ form eightfold ($2a_0 \times 2b_0 \times 2c_0$) superstructures. It consists of TaS_2 layers with Ta in trigonal prismatic coordination by sulfur and the intercalated atoms in the Van der Waals gaps. Intercalated Cu in $6R-Cu_{0.237}TaS_2$ is present at octahedral and tetrahedral sites in alternating Van der Waals gaps, but for $6R-Cu_{0.23}Ta_{1.06}S_2$ tantalum occupies the octahedral sites in one interlayer space, while copper occupies the tetrahedral sites in the other Van der Waals gap. Doubling of the unit cell axes along a and b directions expresses vacancy ordering and doubling of the c axis is the result of complementary ordering in consecutive octahedral and tetrahedral layers in the Van der Waals gaps. The average maximum occupation ($x+y = 0.375$) of intercalated atoms is much smaller than the theoretical maximum occupation of $x+y = 1$. Inhomogeneity of the chemical reaction is established by single-crystal X-ray diffraction experiments. The temperature-dependent experiment confirmed the existence of eightfold superstructures at room temperature as well as at low temperatures, and eliminates the possibility of further ordering of intercalated atoms and possible CDWs phase transitions at low temperatures.

The chemical vapor transport (CVT) method has been employed for the first time for the synthesis of copper-intercalated TaSe_2 , $2\text{H-Cu}_x\text{Ta}_{1+y}\text{Se}_2$ compounds. Hexagonal-shaped crystals were formed towards the hotter zone of the ampoule up to $T \approx 895\text{K}$. The final compositions of crystals in two batches are found to be different, though the nominal composition was same for both batches. Different diameters of the ampoules and different temperature gradients may have affected the convection and diffusion in the vapor transport, which have influenced the relative amounts of Ta and Cu being transported in both batches. A fourfold ($2a_0 \times 2b_0 \times c_0$) superstructure has been found for $2\text{H-Cu}_{0.52}\text{TaSe}_2$. The superstructure is a result of vacancy ordering within the planes of intercalated atoms. In $2\text{H-Cu}_{0.52}\text{TaSe}_2$, the intercalated copper atoms occupy tetrahedral sites in the Van der Waals gaps between TaSe_2 layers, whereas for $2\text{H-Cu}_{0.16}\text{Ta}_{1.08}\text{Se}_2$ intercalated Cu and additional Ta occupy at the octahedral sites in alternating Van der Waals gaps. The total experimental average occupancy over all tetrahedral sites is 0.26, which is lower than the average theoretical occupancy of 0.50 for $2\text{H-Cu}_{0.52}\text{TaSe}_2$. The amount of copper in both the above mentioned compounds is consistent with the homogeneity ranges found for $2\text{H-Cu}_x\text{TaS}_2$ (MoS_2 structure type, $0.28 \leq x \leq 0.67$; NbS_2 structure type, $0.10 \leq x \leq 0.20$).

Single crystals of Cu_3TaSe_4 have been synthesized by CVT method, while attempting to synthesize copper-intercalated TaSe_2 compounds. The nominal composition was taken as $\text{Cu} : \text{Ta} : \text{Se} = 0.21 : 1.15 : 2$ for the synthesis. Cubic-shaped, orange-yellow-colored crystals were formed at the colder zone of the ampoule. The present single-crystal diffraction study provides a better and more accurate description of the crystal structure, with smaller s.u. of structural parameters and anisotropic ADPs, than in the previous study employing powder diffraction [G.E. Delgado et al., *J. Alloys Comp.* 439, 346 (2007)]. The present structure model is in better agreement with the crystal chemical properties of Cu_3NbSe_4 and other related sulvanite compounds Cu_3MX_4 ($M = \text{V}, \text{Ta}$; $X = \text{S}, \text{Se}, \text{Te}$). Bond valence sum (BVS) method is used for determining atomic valences of Cu, M and X in Cu_3MX_4 compounds.

Chapter 8

Zusammenfassung

In dieser Arbeit wurden die Synthesen und Kristallstrukturen von Übergangsmetall-dichalkogenide (*engl.*: Transition Metal Dichalcogenides, TMDCs) $6R-Cu_xTa_{1+y}S_2$ and $2H-Cu_xTa_{1+y}Se_2$, sowie von der Verbindung Cu_3TaSe_4 untersucht. Die Synthese dieser Verbindungen wurde mit Hilfe des chemischen Transports (*engl.*: chemical vapor transport, CVT) durchgeführt, wobei Jod als Transportmittel diente. Bei der Röntgenbeugung können Überstruktureffekte auftreten, was auf die Existenz einer Überstruktur hinweist. Für $6R-Cu_xTa_{1+y}S_2$ ($x = 0.237$, $y = 0$; $x = 0.23$, $y = 0.06$) wurde eine achtfache Überstruktur und für $2H-Cu_{0.52}TaSe_2$ wurde eine vierfache Überstruktur gefunden. $2H-Cu_{0.16}Ta_{1.08}Se_2$ und Cu_3TaSe_4 bilden keine Überstrukturen.

Die Verbindungen des Typs $6R-Cu_xTa_{1+y}S_2$ wurden bei verschiedenen Temperaturen mit Hilfe der Einkristallstrukturanalyse röntgenographisch untersucht. $6R-Cu_xTa_{1+y}S_2$ bildet achtfache ($2a_0 \times 2b_0 \times 2c_0$) Überstrukturen aus. Es besteht aus Tantal-sulfidschichten mit durch Schwefel trigonal prismatisch koordiniertem Tantal und in den sogenannten Van der Waals-Lücken befinden sich eingelagerte oder interkalierte Atome. Interkaliertes Kupfer besetzt in $6R-Cu_{0.237}TaS_2$ tetraedrische und oktaedrische Plätze in abwechselnden Van der Waals-Lücken, jedoch besetzt Tantal in $6R-Cu_{0.23}Ta_{1.06}S_2$ in der einen Zwischengitterschicht einen oktaedrischen Platz, während Kupfer einen tetraedrischen in der anderen besetzt. Da nicht alle Atomplätze in den Van der Waals-Lücken besetzt sind, und diese Teilbesetzung einem Muster folgt, ergibt sich eine Verdopplung der Gitterachsen a und b, die Verdopplung der c-Achse resultiert aus dem komplementären Besetzungsmuster von tetra- und oktaedrischen Schichten in den Van der Waals-Lücken. Die Maximalbesetzung ($x + y = 0.375$) der Atome auf Interkalationspositionen ist viel geringer

als die theoretische Maximalbesetzung von $x + y = 1$. Durch Einkristallbeugungsexperimente konnte die Inhomogenität der chemischen Reaktion gezeigt werden. Die Messung bei verschiedenen Temperaturen konnten die Existenz einer achtfachen Überstruktur sowohl bei Zimmertemperatur, als auch bei niedrigen Temperaturen nachweisen. Dadurch wurde auch gezeigt, dass es keine weiteren Ordnungseffekte, oder einen Phasenübergang zu einer Ladungsdichtewellenphase (*engl.*: Charge-Density-Wave CDW) bei tiefen Temperaturen gibt.

Der chemische Transport (CVT) wurde hier erstmalig zur Synthese von Kupferinterkalierten TaSe_2 , $2\text{H-Cu}_x\text{Ta}_{1+y}\text{Se}_2$ Verbindungen eingesetzt. In der wärmeren Zone (bis $T \approx 895\text{K}$) der Ampulle wurden sechseckige Kristalle gebildet. In zwei Ansätzen mit der gleichen Ausgangsstöchiometrie wurden Kristalle mit unterschiedlicher Zusammensetzung gefunden. Dies könnte durch unterschiedliche Ampulldurchmesser und andere Temperaturgradienten, und damit andere Konvektionsströme mit verschiedene relative Konzentrationen an Tantal und Kupfer, in beiden Ansätzen, verursacht worden sein. Eine vierfache ($2a_0 \times 2b_0 \times c_0$) Überstruktur wurde bei $2\text{H-Cu}_{0.52}\text{TaSe}_2$ gefunden. Die Überstruktur ist verursacht durch eine Besetzungsordnung innerhalb der Ebenen der interkalierten Atome. In $2\text{H-Cu}_{0.52}\text{TaSe}_2$, besetzen die interkalierten Kupferatome tetraedrische Plätze in den Van der Waals-Lücken zwischen TaSe_2 -Schichten, während bei $2\text{H-Cu}_{0.16}\text{Ta}_{1.08}\text{Se}_2$ interkalierte Kupfer- und Tantalatome auf oktaedrischen Lagen in abwechselnden Van der Waals-Lücken sitzen. Die gesamte Durchschnittsbesetzung ist mit 0.26 niedriger als die theoretisch mögliche von 0.5 bei $2\text{H-Cu}_{0.52}\text{TaSe}_2$. Die Menge an Kupfer in beiden Verbindungen ist konsistent mit den Bereichen für $2\text{H-Cu}_x\text{TaS}_2$ (MoS_2 Struktur-Typ, $0.28 \leq x \leq 0.67$; NbS_2 Struktur-Type, $0.10 \leq x \leq 0.20$).

Einkristalle von Cu_3TaSe_4 wurden durch CVT synthetisiert bei dem Versuch Kupferinterkalierte Tantal-selenidverbindungen herzustellen. Die Ausgangsstöchiometrie war: $\text{Cu} : \text{Ta} : \text{Se} = 0.21 : 1.15 : 2$. Würfelförmige gelborange gefärbte Kristalle wurden im kälteren Bereich der Ampulle gebildet. Die durchgeführte Einkristallstrukturstudie stellt eine Verbesserung der Pulverbeugungsstudie von [G.E. Delgado et al., J. Alloys Comp. 439, 346 (2007)] dar. Das Strukturmodell ist in besserer Übereinstimmung mit den kristallchemischen Eigenschaften von Cu_3NbSe_4 und anderen verwandten Sulvanit-Verbindungen Cu_3MX_4 ($M = \text{V}, \text{Ta}$; $X = \text{S}, \text{Se}, \text{Te}$). Die Bindungswertsummenmethode (*engl.*: Bond valence sum (BVS)) wurde zur Bestimmung der Valenzen von Cu, M und X in Cu_3MX_4 -Verbindungen verwendet.

Appendix A

Supplementary materials:



Table A.1: Structural parameters for the superstructure of $6R\text{-Cu}_{0.237}\text{TaS}_2$

Atom	Wyckoff site	x	y	z	$U_{equiv}/\text{\AA}^2$	Occ.
Taa	6c:3m	0	0	0.040324 (10)	0.001762 (68)	1
Tab	18h:m	0.343654 (65)	0.171827	0.206839 (5)	0.001762 (68)	1
Tac	18h:m	0.170806 (32)	0.341611	0.373620 (5)	0.001762 (68)	1
Tad	6c:3m	0	0	0.540197 (10)	0.001762 (68)	1
Cu1a	3a:-3m	0	0	0	0.003497 (561)	0
Cu1b	9d:.2/m	1/3	1/6	1/6	0.003497 (561)	0.02
Cu1c	9d:.2/m	1/6	1/3	1/3	0.003497 (561)	0.30
Cu1d	3b:-3m	0	0	1/2	0.003497 (561)	0.47
Cu2a	6c:3m	0	0	0.077300	0.001621 (444)	0
Cu2b	18h:m	0.365298 (5504)	0.182469	0.243622 (397)	0.001621 (444)	0.04
Cu2c	18h:m	0.164495 (385)	0.328991	0.411053 (79)	0.001621 (444)	0.22
Cu2d	6c:3m	0	0	0.577646 (62)	0.001621 (444)	0.40
S1a	6c:3m	0	0	0.105118 (61)	0.002957 (214)	1
S1b	18h:m	0.336671 (457)	0.168335	0.271880 (35)	0.002957 (214)	1
S1c	18h:m	0.168007 (229)	0.336105	0.438992 (35)	0.002957 (214)	1
S1d	6c:3m	0	0	0.606154 (60)	0.002957 (214)	1
S2a	6c:3m	0	0	0.147932 (56)	0.001708 (203)	1
S2b	18h:m	0.336121 (445)	0.168061	0.313755 (34)	0.001708 (203)	1
S2c	18h:m	0.168602 (223)	0.337204	0.480356 (34)	0.001708 (203)	1
S2d	6c:3m	0	0	0.646508 (56)	0.001708 (203)	1

Table A.2: Anisotropic ADPs for the superstructure of 6R-Cu_{0.237}TaS₂; (Ta* = Taa = Tab = Tac = Tad; Cu1* = Cu1a = Cu1b = Cu1c = Cu1d; Cu2* = Cu2a = Cu2b = Cu2c = Cu2d; S1* = S1a = S1b = S1c = S1d; S2* = S2a = S2b = S2c = S2d)

Atom	U_{11}	U_{22}	U_{33}	U_{12}	U_{13}	U_{23}
Ta*	0.001171 (100)	0.001171	0.002944 (153)	0.000585	0.0	0.0
Cu1*	0.002991 (761)	0.002991	0.004510 (1342)	0.001496	0.0	0.0
Cu2*	0.001415 (629)	0.001415	0.002033 (1037)	0.000708	0.0	0.0
S1*	0.002447 (269)	0.002447	0.003979 (534)	0.001223	0.0	0.0
S2*	0.000272 (249)	0.000272	0.004579 (511)	0.000136	0.0	0.0

Table A.3: Structural parameters for the superstructure of $6R-Cu_{0.23}Ta_{1.06}S_2$

Atom	Wyckoff site	x	y	z	$U_{equiv}/\text{\AA}^2$	Occ.
Ta1a	6c:3m	0	0	0.040310 (8)	0.003216 (134)	1
Ta1b	18h:m	0.342348 (66)	0.171174	0.206907 (5)	0.002669 (131)	1
Ta1c	18h:m	0.171368 (33)	0.342735	0.373546 (5)	0.002880 (131)	1
Ta1d	6c:3m	0	0	0.540227 (8)	0.003383 (135)	1
Ta2a	3a:-3m	0	0	0	0.008534	0
Ta2b	9d:.2/m	1/3	1/6	1/6	0.016183 (2584)	0.09
Ta2c	9d:.2/m	1/6	1/3	1/3	0.038018 (2832)	0.14
Ta2d	3b:-3m	0	0	1/2	0.004085 (511)	0.27
Cu2a	6c:3m	0	0	0.077300	0.004599	0
Cu2b	18h:m	0.331240 (1757)	0.165620	0.244357 (190)	0.026102 (4092)	0.16
Cu2c	18h:m	0.166739 (402)	0.333477	0.411077 (78)	0.012606 (1632)	0.30
Cu2d	6c:3m	0	0	0.577501 (38)	0.003467 (615)	0.47
S1a	6c:3m	0	0	0.105019 (52)	0.004391 (631)	1
S1b	18h:m	0.336428 (378)	0.168214	0.272098 (33)	0.003272 (565)	1
S1c	18h:m	0.168250 (198)	0.336499	0.439086 (33)	0.004809 (593)	1
S1d	6c:3m	0	0	0.606242 (50)	0.002779 (614)	1
S2a	6c:3m	0	0	0.147730 (51)	0.002471 (613)	1
S2b	18h:m	0.337207 (371)	0.168603	0.313978 (33)	0.002793 (565)	1
S2c	18h:m	0.168463 (188)	0.336926	0.480356 (33)	0.003023 (568)	1
S2d	6c:3m	0	0	0.646575 (51)	0.002189 (610)	1

Table A.4: Anisotropic ADPs for the superstructure of 6R-Cu_{0.23}Ta_{1.06}S₂

Atom	U_{11}	U_{22}	U_{33}	U_{12}	U_{13}	U_{23}
Ta1a	0.004538 (209)	0.004538	0.000571 (291)	0.002269	0.0	0.0
Ta1b	0.002170 (175)	0.003351 (170)	0.002093 (219)	0.001085	-0.000051 (99)	-0.000025
Ta1c	0.004288 (171)	0.001350 (174)	0.002023 (219)	0.000675	-0.000104 (50)	-0.000208
Ta1d	0.004884 (210)	0.004884	0.000382 (292)	0.002442	0.0	0.0
Ta2a	0.008008	0.008008	0.009586	0.004004	0.0	0.0
Ta2b	0.012810 (3564)	0.015860 (3074)	0.018862 (4365)	0.006405	-0.008830 (2397)	-0.004415
Ta2c	0.045939 (3724)	0.040161 (4213)	0.026029 (3999)	0.020080	0.003027 (1302)	0.006054
Ta2d	0.002430 (749)	0.002430	0.007395 (1161)	0.001215	0.0	0.0
Cu2a	0.005456	0.005456	0.002885	0.002728	0.0	0.0
Cu2b	0.019273 (5351)	0.0019010 (4214)	0.040110 (8260)	0.009637	0.013102 (4047)	0.006551
Cu2c	0.013216 (1869)	0.015277 (2489)	0.010014 (2597)	0.007639	-0.003053 (736)	-0.006105
Cu2d	0.002726 (937)	0.002726	0.004948 (1357)	0.001363	0.0	0.0
S1a	0.004858 (925)	0.004858	0.003458 (1436)	0.002429	0.0	0.0
S1b	0.003365 (835)	0.003062 (626)	0.003490 (967)	0.001682	0.000635 (690)	0.000317
S1c	0.006026 (670)	0.006194 (895)	0.002264 (973)	0.003097	-0.000746 (354)	-0.001493
S1d	0.002398 (870)	0.002398	0.003540 (1429)	0.001199	0.0	0.0
S2a	0.001768 (863)	0.001768	0.003876 (1435)	0.000884	0.0	0.0
S2b	0.002425 (843)	0.002208 (610)	0.003819 (974)	0.001212	0.000218 (691)	0.000109
S2c	0.002568 (614)	0.003809 (859)	0.003104 (961)	0.001905	0.000270 (350)	0.000541
S2d	0.001449 (861)	0.001449	0.003669 (1425)	0.000724	0.0	0.0

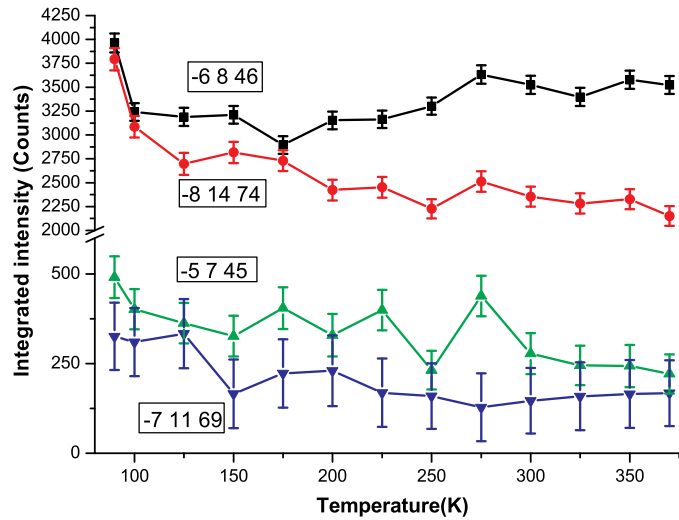


Figure A.1: Temperature dependence of the integrated intensities of selected superlattice reflections and main reflections.

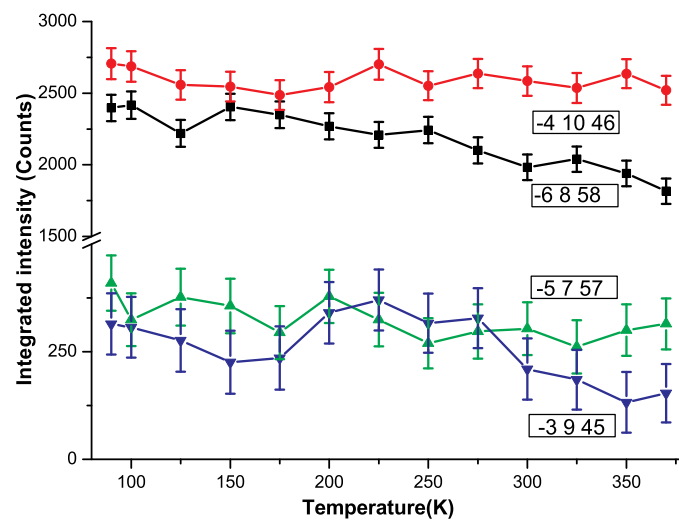


Figure A.2: Temperature dependence of the integrated intensities of selected superlattice reflections and main reflections.

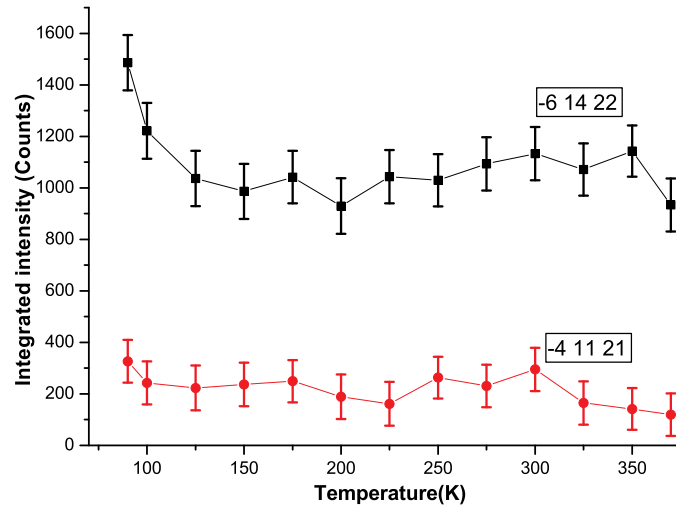


Figure A.3: Temperature dependence of the integrated intensities of selected superlattice reflections and main reflections.

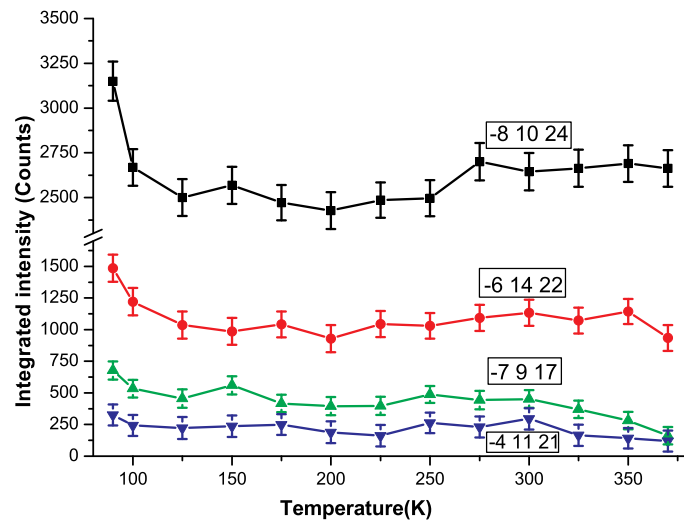


Figure A.4: Temperature dependence of the integrated intensities of selected superlattice reflections and main reflections.

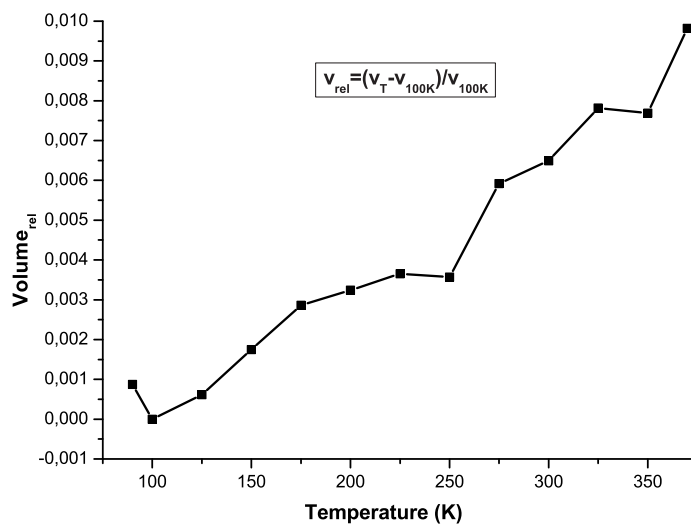


Figure A.5: Temperature dependence of relative volume against temperature.

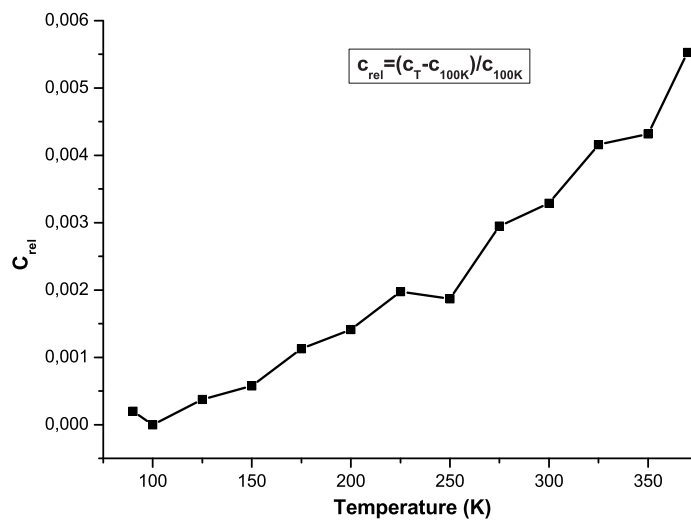


Figure A.6: Temperature dependence of relative cell parameters against temperature.

Appendix B

Supplementary materials:

2H-Cu_{0.52}TaSe₂ and

2H-Cu_{0.16}Ta_{1.08}Se₂

Table B.1: Structural parameters for the superstructure of 2H-Cu_{0.52}TaSe₂

Atom	Wyckoff site	x	y	z	$U_{equiv}/\text{\AA}^2$	Occ.
Ta1a	1b : -6m2	0	0	1/2	0.007913 (124)	1
Ta1b	3k : mm2	0.507401 (41)	0.014801	1/2	0.008457 (140)	1
Ta2a	3j : mm2	0.313178 (68)	0.156589	0.0	0.004802 (126)	1
Ta2b	1c : 6m2	1/3	2/3	0.0	0.007754 (150)	1
Se1a	2g : 3m.	0.0	0.0	0.129605 (99)	0.007812 (209)	1
Se1b	6n : .m.	0.502849 (65)	0.005699	0.118352 (77)	0.007817 (214)	1
Se2a	6n : .m.	0.327827 (116)	0.163913	0.374969 (84)	0.011709 (297)	1
Se2b	2h : 3m.	1/3	2/3	0.381816 (136)	0.012157 (299)	1
Cu1a	6n : .m.	0.343392 (1579)	0.171696	0.213485 (752)	0.048072 (5057)	0.20
Cu1b	2h : 3m.	1/3	2/3	0.216366 (244)	0.018254 (680)	0.60
Cu2a	2g : 3m.	0.0	0.0	0.280310	0.005718	0
Cu2b	6n : .m.	0.503445 (276)	0.006889	0.284244 (218)	0.006452 (843)	0.30

Table B.2: Anisotropic ADPs for the superstructure of 2H-Cu_{0.52}TaSe₂

Atom	U11	U22	U33	U12	U13	U23
Ta1a	0.009776 (222)	0.009776	0.004186 (223)	0.004888	0.0	0.0
Ta1b	0.011818 (225)	0.007690 (179)	0.004486 (169)	0.003845	0.0	0.0
Ta2a	0.003584 (157)	0.004559 (203)	0.005937 (160)	0.001792	0.0	0.0
Ta2b	0.005683 (247)	0.005683	0.011896 (309)	0.002842	0.0	0.0
Se1a	0.008996 (375)	0.008996	0.005503 (378)	0.004883	0.0	0.0
Se1b	0.007449 (324)	0.009254 (282)	0.007348 (288)	0.004627	0.001622 (125)	0.003244
Se2a	0.011499 (346)	0.015692 (511)	0.006537 (343)	0.005749	0.000315 (204)	0.000158
Se2b	0.014334 (562)	0.014334	0.007803 (491)	0.007167	0.0	0.0
Cu1a	0.025347 (1271)	0.025347	0.004062 (1137)	0.012675	0.0 (125)	0.0
Cu1b	0.054357 (6394)	0.079884 (9127)	0.001490 (3061)	0.027179	0.006169 (2418)	0.003084
Cu2a	0.008523	0.008523	0.000107	0.004262	0.0	0.0
Cu2b	0.009663 (1180)	0.008133 (1172)	0.001053 (1213)	0.004067	-0.000326 (458)	-0.000652

Table B.3: Structural parameters of 2H-Cu_{0.16}Ta_{1.08}Se₂.

Atom	Wyckoff site	x	y	z	$U_{equiv}/\text{\AA}^2$
Ta1	2c : 3m.	0.0	0.0	0.250027 (34)	0.008755 (111)
Se1	2d : 3m.	2/3	1/3	0.120107 (84)	0.008498 (176)
Se1	2d : 3m.	2/3	1/3	0.380002 (83)	0.008557 (176)
Ta2	1a : -3m.	0.0	0.0	0.0	0.011227 (847)
Cu2	1b : -3m.	0.0	0.0	0.5	0.031507 (2781)

Table B.4: Anisotropic ADPs of 2H-Cu_{0.16}Ta_{1.08}Se₂

Atom	U_{11}	U_{22}	U_{33}	U_{12}	U_{13}	U_{23}
Ta1	0.010358 (185)	0.010358	0.005548 (224)	0.005179	0.0	0.0
Se1	0.009265 (273)	0.009265	0.006964 (383)	0.004632	0.0	0.0
Se2	0.009528 (274)	0.009528	0.006615 (380)	0.004764	0.0	0.0
Ta2	0.015319 (1602)	0.015319	0.003043 (1376)	0.007659	0.0	0.0
Cu2	0.042239 (5569)	0.042239	0.010042 (3808)	0.021119	0.0	0.0

Appendix C

Supplementary materials:



Table C.1: Structural parameters of Cu_3MX_4 at room temperature.

Atom	Wyckoff site	x	y	z	$U_{equiv}/\text{\AA}^2$
Cu	3d : -42.m	1/2	0.0	0.0	0.015037 (49)
Ta	1a : -43m	0.0	0.0	0.0	0.005146 (13)
Se	4e : .3m	0.248989 (34)	0.248989	0.248989	0.010014 (16)

Table C.2: Anisotropic ADPs for $6\text{R-Cu}_{0.23}\text{Ta}_{1.06}\text{S}_2$

Atom	U_{11}	U_{22}	U_{33}	U_{12}	U_{13}	U_{23}
Cu	0.007816 (96)	0.018647 (110)	0.018647	0.0	0.0	0.0
Ta	0.005146 (38)	0.005146	0.005146	0.0	0.0	0.0
Se	0.010014 (48)	0.0010014	0.0010014	-0.001394 (29)	-0.001394	-0.001394

Publications

Parts of this thesis published in the international scientific literature or will be submitted for publication:

Chapter 4:

S. I. Ali, S. Mondal, S. J Prathapa, S. van Smaalen, S. Zörb, B. Harbrecht
Self-Intercalation and Vacancy-Ordering in 6R-Cu_xTa_{1+y}S₂ ($x \approx 0.23$, $y = 0, 0.06$),
Z. Anorg. Allg. Chem., (2012), 638, 2625–2631.

Chapter 6:

S. I. Ali, S. van Smaalen.
Synthesis, single crystal X-ray structure of Cu₃TaSe₄ and comparative studies with other Cu₃MX₄ (M = V, Nb, Ta; X = S, Se, Te),
Z. Anorg. Allg. Chem., (2014), 640, 931–934.

Chapter 5 work will be submitted as,

S. I. Ali, S. Mondal, S. van Smaalen.
Synthesis, Superstructure and Vacancy-Ordering in 2H-Cu_xTa_{1+y}Se₂ (MoS₂-type and NbS₂-type),
Z. Anorg. Allg. Chem., (2014).

Bibliography

- Ali, M. N., Ji, H., Hirai, D., Fucillo, M. K. and Cava, R. (2013). Synthesis and characterization of two crystallographic forms of $\text{Ag}_{0.79}\text{VS}_2$, *J. Solid State Chem.* **202**: 77–84.
- Ali, S. I., Mondal, S., Prathapa, S. J., van Smaalen, S., Zörb, S. and Harbrecht, B. (2012). Self-Intercalation and Vacancy-Ordering in $6\text{R-Cu}_x\text{Ta}_{1+y}\text{S}_2$ ($x \approx 0.23$, $y = 0, 0.06$), *Z. Anorg. Allg. Chem.* **638**: 2625–2631.
- Aslanov, L. A., Ukrainski, Y. M. and Simanov, Y. P. (1963). Tantalum diselenide and triselenide, *Russ. J. Inorg. Chem.* **8**: 937–939.
- Benavente, E., Ana, M. A. S., Mendiza, F. and Gonza, G. (2002). Intercalation chemistry of molybdenum disulfide, *Coord. Chem. Rev.* **224**: 87–109.
- Berry, L. G. (1954). Tunable band gaps in bilayer transition-metal dichalcogenides, *Am. Mineral.* **39**: 504–509.
- Binnewies, M., Glaum, R., Schmidt, M. and Schmidt, P. (2012). *Chemical Vapor Transport Reactions*, De Gruyter, 2012, Berlin.
- Binnewies, M., Glaum, R., Schmidt, M. and Schmidt, P. (2013). Chemical vapor transport reactions a historical review, *Z. Anorg. Allg. Chem.* **639**: 219–229.
- Bjerkelund, E. and Kjekshus, A. (1967). On the structural properties of the $\text{Ta}_{1+x}\text{Se}_2$, *Acta Chem. Scand.* **21**: 513–526.
- Böhm, M. C., Schulte, J. and Schlögl, R. (1996). Solid state electronic structure of potassium graphite intercalation compounds; the systems KC_{24} and KC_8 , *Phys. Status Solidi B* **196**: 131–144.

- Bohnen, K. (1995). *Schichtartig aufgebaute Kupfer-tantal-sulfide, Ausgangssubstanzen für die Darstellung neuer Tantal-sulfide*, PhD thesis, Bonn University, Bonn, Germany.
- Brauer, H. E., Starnberg, H. I., Holleboom, L. J., Hughes, H. P. and Strocov, V. N. (2001). Na and Cs intercalation of 2H-TaSe₂ studied by photoemission, *J. Phys.: Condens. Matter* **13**: 9879–9895.
- Breese, N. E. and O’Keeffe, M. (1991). Bond-Valence Parameters for Solids, *Acta Cryst.* **B47**: 192–197.
- Brixner, L. H. (1962). Preparation and properties of the single crystalline AB₂ type selenides and tellurides of Niobium, Tantalum, Molybdenum and Tungsten, *J. Inorg. Nucl. Chem.* **24**: 257–263.
- Brouwer, R. and Jellinek, F. (1980). The low-temperature superstructures of 1T-TaSe₂ and 2H-TaSe₂, *Physica* **99B**: 51–55.
- Brown, B. E. and Beerntsen, D. J. (1965). Layer structure polytypism among niobium and tantalum selenides, *Acta Cryst.* **18**: 31–36.
- Brown, I. D. (2009). Recent Developments in the Methods and Applications of the Bond Valence Model, *Chem. Rev.* **109**: 6858–6919.
- Brown, I. D. and Altermatt, D. (1985). Bond-Valence Parameters Obtained from a Systematic Analysis of the Inorganic Crystal Structure Database from the Inorganic Crystal, *Acta Cryst.* **B41**: 244–247.
- Brown, I. D. and Shannon, R. D. (1973). Empirical Bond-Strength-Bond-Length Curves for Oxides, *Acta Crystallogr., Sect. A* **29**: 266–282.
- Bunsen, R. (1852). Chemical vapor transport reactions : A historical review, *J. Prakt. Chem.* **56**: 53.
- Castro Neto, A. H. (2001). Charge Density Wave, Superconductivity, and Anomalous Metallic Behavior in 2D Transition Metal Dichalcogenides, *Phys. Rev. Lett.* **86**: 4382–4385.
- Chen, Y. L., Feng, X. Y., Ouyang, B. Z. and Wang, C. L. (1992). Mössbauer effect of iron-57 intercalated in layered compound 2H-Fe_{0.5}TaSe₂, *Hyperfine Interact.* **71**: 1375–1378.

- Crawack, H. J. and Pettenkofer, C. (2001). Calculation and XPS measurements of the Ta4f CDW splitting in Cu, Cs and Li intercalation phases of 1T-TaX₂ (X = S,Se), *Solid State Commun.* **118**: 325–332.
- Dai, Z., Xue, Q., Gong, Y., Slough, C. G. and Coleman, R. V. (1993). Scanning-probe-microscopy studies of superlattice structures and density wave structures in 2H-NbSe₂, 2H-TaSe₂ and 2H-TaS₂ induced by Fe doping, *Phys. Rev. B.* **48**(19): 14543.
- Del Rio, M. and Dejeus, R. (1998). *XOP 2.0 software online reference manual*, 2nd edn, European Synchrotron Radiation Facility (ESRF), Grenoble, France.
- Delgado, G. E., Contreras, J. E., Mora, A. J., Durán, S., Muñoz, M. and Grima-Gallardo, P. (2011). Structure Refinement of the Semiconducting Compound Cu₃TaS₄ from X-Ray Powder Diffraction Data, *Acta. Phys. Pol. A* **120**: 468–472.
- Delgado, G. E., Mora, A. J., Durán, S., Muñoz, M. and Grima-Gallardo, P. (2007). Structural characterization of the ternary compound Cu₃TaSe₄, *J. Alloys Compd.* **439**: 346 – 349.
- Delgado, G., Mora, A., Marcano, G. and Rincón, C. (2003). Crystal structure refinement of the semiconducting compound Cu₂SnSe₃ from X-ray powder diffraction data, *Mater. Res. Bull.* **38**: 1949 – 1955.
- Du, C.-H., Lin, W. J., Su, Y., Tanner, B. K., Hatton, P. D., Casa, D., Keimer, B., Hill, J. P., Oglesby, C. S. and Hohl, H. (2000). X-ray scattering studies of 2H-NbSe₂, a superconductor and charge density wave material, under high external magnetic fields, *J. Phys.: Condens. Matter* **12**: 5361–5370.
- Espinosa-García, W., Ruiz-Tobón, C. and Osorio-Guillén, J. (2011). The elastic and bonding properties of the sulvanite compounds: A first-principles study by local and semi-local functionals, *Physica B* **406**: 3788 – 3793.
- Fang, C. M., Wieggers, G. A., Meetsma, A., de Groot, R. A. and Haas, C. (1996). Crystal structure and band structure calculations of Pb_{0.33}TaS₂ and Sn_{0.33}NbS₂, *Physica B* **226**: 259–267.
- Figuroa, E., Brill, J. W. and Selegue, J. P. (1996). New intercalation compounds of transition metal dichalcogenides, *J. Phys. Chem. Solids* **57**: 1123–1127.

- Friend, R. H. and Yoffe, A. D. (1987). Electronic properties of intercalation complexes of the transition metal dichalcogenides, *Adv. Phys.* **36**: 1–94.
- Fung, K. K., Steeds, J. W. and Eades, J. A. (1980). Application of convergent beam electron diffraction to study the stacking of layers in transition-metal dichalcogenides, *Physica* **99B**: 47–50.
- Gotoh, Y., Akimoto, J. and Oosawa, Y. (1998). Crystal structure of 3R-Ta_{1.08}S₂, *J. Alloys Compd.* **270**: 115–118.
- Gulay, L., Daszkiewicz, M., Strok, O. and Pietraszko, A. (2011). Crystal structure of Cu₂Se, *Chem. Met. Alloys* **4**: 200–205.
- Gunst, S., Kleint, A., Jaegermann, W., Tomm, Y., Crawack, H. J. and Jungblut, H. (2000). Intercalation and Deintercalation of Transition Metal Dichalcogenides : Nanostructuring of Intercalated Phases by Scanning Probe Microscopy, *Ionics* **6**: 180–186.
- Harbrecht, B. and Kreiner, G. (1989). Syntheses and Crystal Structures of the Phases 6R-Cu_xM_{1+y}S₂ (M = Nb, Ta), *Z. Anorg. Allg. Chem.* **572**: 47–54.
- Henderson, M. J. and White, J. W. (2011). An X-ray diffraction and small angle X-ray scattering study of solvated Li-graphite intercalation compounds, *Int. J. Energ. eng.* **1**: 19–26.
- Herrendorf, W. and Bärnighausen, H. (1997). *HABITUS*, University of Karlsruhe, Giessen, Germany.
- Hillenius, S. J., Coleman, R. V., Domb, E. R. and Sellmyer, D. J. (1979). Magnetic properties of iron-doped layer-structure dichalcogenides, *Phys. Rev. B.* **19**: 4711–4722.
- Huisman, R., Kadijk, F. and Jellinek, F. (1970). The non-stoichiometric phases Nb_{1+x}Se₂ and Ta_{1+x}Se₂, *J. Less-Common Met.* **21**: 187–193.
- Hulliger, F. (1961). Neue halbleitende verbindungen vom sulvanit-typ, *Helv. Phys. Acta* **34**: 379–382.
- Inoue, M., Hughes, H. P. and Yoffe, A. D. (1989). The electronic and magnetic properties of the 3d transition metal intercalates of TiS₂, *Adv. Phys.* **38**: 565–604.

- Jellinek, F. (1962). The system tantalum-sulfur, *J. Less-Common Met.* **4**: 9–15.
- Jellinek, F., Brauer, G. and Müller, H. (1960). Molybdenum and Niobium Sulphides, *Nature* **185**: 376–377.
- Kadijk, F., Huisman, R. and Jellinek, F. (1964). Niobium and tantalum diselenides, *Recl. Trav. Chim. Pays-Bas* **83**: 768–775.
- Kalikhman, V. L. and Umanskii, Y. S. (1973). Transition-metal chalcogenides with layer structures and features of the filling of their berrilium zones, *Soviet Phys. Uspekhi* **728**: 728–740.
- Kars, M., Rebbah, A. and Rebbah, H. (2005). Cu_3NbS_4 , *Acta Crystallogr. Sect. E* **61**: i180–i181.
- Katzke, H., Tolédano, P. and Depmeier, W. (2004). Phase transitions between polytypes and intralayer superstructures in transition metal dichalcogenides, *Phys. Rev. B* **69**: 1–8.
- Kertesz, M. and Hoffmann, R. (1984). Octahedral vs. trigonal-prismatic coordination and clustering in transition-metal dichalcogenides, *J. Am. Chem. Soc.* **106**: 3453–3460.
- Klepp, K. O. and Gurtner, D. (2000). Crystal structure of tricopper tetrase-lenidovanadate(V), Cu_3VSe_4 , *Z. Kristallogr. New Cryst. Struct.* **215**: 4–8.
- König, A., Koepernik, K., Schuster, R., Kraus, R., Knupfer, M., Büchner, B. and Berger, H. (2012). Plasmon evolution and charge-density wave suppression in potassium intercalated 2H-TaSe₂, *EPL* **100**: 27002.
- Kordyuk, A. A., Evtushinsky, D. V., Zabolotnyy, V. B., Haenke, T., Hess, C., Yaresko, A. N., Berger, H. and Borisenko, S. V. (2010). Chiral honeycomb superstructure, parquet nesting, and Dirac cone formation in Cu-intercalated 2H-TaSe₂, *ArXiv* **1003.1976**.
- Kracht, K. (2013). *Online : A Program Package for Data Acquisition and Beamline Control*, HASYLAB (DESY), Hamburg, Germany.
- Kumakura, T., Tan, H., Handa, T., Morishita, M. and Fukuyama, H. (1996). Charge density waves and superconductivity in 2H-TaSe₂, *Czech. J. Phys.* **46**: 2611–2612.

- Li, J., Guo, H., Proserpio, D. and Sironi, A. (1995). Exploring tellurides: Synthesis and characterization of new binary, ternary, and quaternary compounds, *J. Solid State Chem.* **117**: 247–255.
- Li, L. J., Lu, W. J., Liu, Y., Qu, Z., Ling, L. S. and Sun, Y. P. (2013). Influence of defects on chargedensitywave and superconductivity in 1T-TaS₂ and 2H-TaS₂ systems, *Physica C* **492**: 64–67.
- Li, L., Sun, Y., Zhu, X., Wang, B., Zhu, X., Yang, Z. and Song, W. (2010). Growth and superconductivity of 2H - Ni_{0.02}TaSe₂ single crystals, *Solid State Commun.* **150**: 2248–2252.
- Lu, Y. J. and Ibers, J. A. (1993). Synthesis and characterization of Cu₃NbSe₄ and KCu₂TaSe₄, *J. Solid State Chem.* **107**: 58–62.
- Lüdecke, J., van Smaalen, S., Spijkerman, A., Boer, J. L. D. and Wiegers, G. A. (1999). Commensurately modulated structure of 4H_b - TaSe₂ determined by x-ray crystal-structure refinement, *Phys. Rev. B.* **59**: 6063–6071.
- Malliakas, C. D. and Kanatzidis, M. G. (2013). Nb-Nb interactions define the charge density wave structure of 2H-NbSe₂, *J. Am. Chem. Soc.* **135**(5): 1719–1722.
- Marseglia, E. A. (1983). Transition metal dichalcogenides and their intercalates, *Int. Rev. Phys. Chem.* **3**: 177–216.
- Monceau, P. (2012). Electronic crystals: an experimental overview, *Adv. Phys.* **61**: 325–581.
- Moret, R. and Tronc, E. (1980). CDW induced atomic shifts in 4H_b-TaSe₂, *Physica* **99B**: 56–58.
- Mori, M., Moss, S. C. and Jan, Y. M. (1983). Order-disorder in higher-stage (n =3, 4) potassium graphites, *Phys. Rev. B.* **27**: 6385–6394.
- Morosan, E., Zandbergen, H. W., Li, L., Lee, M., Checkelsky, J. G., Heinrich, M., Siegrist, T., Ong, N. P. and Cava, R. J. (2007). Sharp switching of the magnetization in Fe_{0.25}TaS₂, *Phys. Rev. B.* **75**: 104401.
- Moroson, E., Zanderbargen, H. W., Dennis, B. S., Bos, J. W. G., Onose, T., Klimczuk, T., Ramirez, A. P., Ong, N. P. and Cava, R. J. (2006). Superconductivity in Cu_xTiSe₂, *Nature Phys.* **2**: 544–550.

- Mulazzi, M., Chainani, A., Katayama, N., Eguchi, R., Matsunami, M., Ohashi, H., Senba, Y., Nohara, M., Uchida, M., Takagi, H. and Shin, S. (2010). Absence of nesting in the charge-density-wave system 1T-VS₂ as seen by photoelectron spectroscopy, *Phys. Rev. B* **82**: 075130.
- Nakashizu, T., Sekine, T., Uchinokura, K. and Matsuura, E. (1986). Raman study of CDW phase transition in 4H_b-TaSe₂, *J. Phys. Soc. Jpn.* **55**: 672–682.
- Nakayama, M., Miwa, K., Ikuta, H., Hinode, H. and Wakihara, M. (2006). Electronic Structure of Intercalation Compounds of Co_xNbS₂, *Chem. Mater.* **18**: 4996–5001.
- Nitsche, R. and Wild, P. (1967). Crystal Growth and Electrooptic Effect of CopperTantalumSelenide, Cu₃TaSe₄, *J. Appl. Phys.* **38**: 5413–5414.
- O’Keeffe, M. and Brese, N. E. (1992). Bond-valence parameters for anion-anion bonds in solids, *Acta Cryst. B* **48**: 152–154.
- Osorio-Guillén, J. and Espinosa-García, W. (2012). A first-principles study of the electronic structure of the sulvanite compounds , *Physica B* **407**: 985 – 991.
- Palatinus, L. and Chapuis, G. (2007). SUPERFLIP - a computer program for the solution of crystal structures by charge flipping in arbitrary dimensions, *J. Appl. Cryst.* **40**: 786–790.
- Pandey, D. and Krishna, P. (2006). *Layer stacking in close-packed structures, International Tables for Crystallography (2006). Vol. C, ch. 9.2.1, pp. 752-760*, Kluwer academic, London.
- Papageorgopoulos, C. A., Kamaratos, M., Saltas, V., Jaegermann, W., Pettenkofer, C. and Tonti, D. (1998). Na and Cl₂ intercation on 1T and 2H-TaSe₂(0001) surfaces , *Surf. Rev. Lett.* **5**(5): 997–1005.
- Patel, A. J., Bhayani, M. K. and Jani, A. R. (2009). Growth and surface microtopography of 2H-TaS_xSe_{2-x} single crystals, *Chalcogenide Lett.* **6**: 491–502.
- Pauling, L. (1929). The principles determining the structure of complex ionic crystal, *J. Am. Chem. Soc.* **51**: 1010–1026.
- Pervov, V. S., Volkov, V. V., Falkengof, A. T., Makhonina, E. V. and Elizarova, N. V. (1996). Origin of structural instability in metal-intercalated layered dichalcogenides, *Inorg. Mater.* **32**: 597–600.

- Petricek, V. and Dusek, M. and Palatinus, L. (2006). Jana2006. The crystallographic computing system, Institute of Physics, Praha, Czech Republic.
- Rajora, O. (2006). Thermally activated diffusion of indium into layered materials 2H-TaSe₂ and TaS₂, *Phys. Status Solidi A* **203**: 493–496.
- Salvo, F. J. D., Maines, R. G. and Waszczak, J. V. (1974). Preparation and properties of 1T-TaSe₂, *Solid State Commun.* **14**: 497–501.
- Schreurs, A. M. M., Xian, X. and Kroon-Batenburg, L. M. J. (2010). Eval15-suite, *J. Appl. Cryst.* **43**: 70–82.
- Shannon, R. D. (1976). Revised effective ionic radii and systematic studies of interatomic distances in halides and chalcogenides, *Acta Cryst.* **A32**: 751–767.
- Sharma, S., Auluck, S. and Khan, M. A. (2000). Optical properties of 1T and 2H phases of TaS₂ and TaSe₂, *Pramana – J. Phys.* **54**: 431–440.
- Sheldrick, G. M. (2008). SADABS, Version 2008/1, University of Göttingen, Germany.
- Sipos, B., Kusmartseva, A. F., Akrap, A. and Berger, H. (2008). From Mott state to superconductivity in 1T-TaSe₂, *Nat. Mater.* **7**: 960–965.
- Spijkerman, A., de Boer, J. L., Meetsma, A., Wiegers, G. A. and van Smaalen, S. (1997). X-ray crystal-structure refinement of the nearly commensurate phase of 1T-TaS₂ in (3+2) dimensional superspace, *Phys. Rev. B.* **56**: 13757–13767.
- Stoltz, S., Starnberg, H. and Holleboom, L. (2003). Rb intercalation of 1T-TaSe₂ studied by photoelectron spectroscopy, *Phys. Rev. B.* **67**: 125107.
- Tonti, D., Pettenkofer, C., Jaegermann, W., Papageorgopoulos, D. C., Kamaratos, M. and Papageorgopoulos, C. A. (1998). Alkali Displacements in Intercalated 1T-TaSe₂ Binding Energy (eV) Binding Energy (eV), *Ionics* **4**: 93–100.
- Trojer, F. J. (1966). Refinement of the structure of sylvanite, *Am. Mineral.* **51**: 890 – 894.
- Tsang, J. C. and Shafer, M. W. (1978). Raman spectroscopy of intercalated layered structure compounds, *Solid State Commun.* **25**: 999–1002.

- Van Arkel, A. E. and Crevecoeur, C. (1963). Quelques sulfurs et seleniures complexes, *J. Less-Common Met.* **5**: 177–180.
- van Arkel, A. E. and de Boer, J. H. (1925). Darstellung von reinem titanium-, zirkonium-, hafnium- und thoriummetall, *Z. Anorg. Allg. Chem.* **148**: 345–350.
- van der Lee, A., van Smaalen, S., Wieggers, G. A. and de Boer, J. L. (1991). Order-disorder transition in silver-intercalated niobium disulfide compounds. I. Structural determination of $\text{Ag}_{0.6}\text{NbS}_2$, *Phys. Rev. B.* **43**: 9420–9431.
- van Smaalen, S. (2007). *Incommensurate Crystallography*, International Union of Crystallography Monographs on Crystallography, Oxford University Press, Oxford.
- Verma, A. R. and Krishna, P. (1966). *Polymorphism and Polytypism in Crystals*, New York: Wiley. Russian translation, (1969). Edited by A. S. Povarennykh, MIR: Moscow., New York.
- Wagner, K., Morosan, E., Hor, Y., Tao, J., Zhu, Y., Sanders, T., McQueen, T., Zandbergen, H., Williams, A., West, D. and Cava, R. (2008). Tuning the charge density wave and superconductivity in Cu_xTaS_2 , *Phys. Rev. B.* **78**: 1–6.
- Weil, K. G. (1962). H. Schäfer: Chemische Transportreaktionen. Der Transport anorganischer Stoffe über die Gasphase und seine Anwendung., *Zeitschrift für Elektrochemie, Berichte der Bunsengesellschaft für physikalische Chemie* **66**: 885–885.
- Whittingham, M. S. (1978). Structure and bonding in the pyridine intercalates of tantalum disulfide, *Mater. Res. Bull.* **13**: 775 – 782.
- Whittingham, M. S. and Jacobson, A. J. (1982). *Intercalation chemistry*, Academic press, INC, New York.
- Wieggers, G. A. (1980). Physical properties of first-row transition metal dichalcogenides and their intercalants, *Physica* **99B**: 151–165.
- Wieggers, G. A., Boer, J. L. D., Meetsma, A. and van Smaalen, S. (2001). Domain structure and refinement of the triclinic superstructure of 1T-TaSe₂ by single crystal X-ray diffraction, *Z. Kristallogr.* **216**: 45–50.

- Wilson, J. A., Salvo, F. J. D. and Mahajan, S. (1975). Charge-density waves and superlattices in the metallic layered transition metal dichalcogenides, *Adv. Phys.* **24**: 117–201.
- Wondratschek, H. and Müller, U. (1991). International Tables for Crystallography, Vol. A1, Kluwer Acad. Publ., Dordrecht - Boston - London.
- Wu, X., Tao, Y., Li, L., Zhai, T., Bando, Y. and Golberg, D. (2011). Preparation and Field-Emission of TaSe₂ Nanobelt Quasi-Arrays, and Electrical Transport of Its Individual Nanobelt, *J. Nanosci. Nanotechnol.* **11**: 10123–10129.
- Wu, Y., Nther, C. and Bensch, W. (2004). Low Dimensional Materials: Syntheses, Structures, and Optical Properties of Rb₂CuTaS₄, Rb₂CuTaSe₄, RbCu₂TaSe₄, K₃Ag₃Ta₂Se₈, and Rb₃AgTa₂Se₁₂, *Z. Naturforsch.* **59b**: 1006–1014.
- Yang, D., Westreich, P. and Frindt, R. F. (1999). Transition metal dichalcogenides / polymer nanocomposites, *Nanostruct. Mater.* **12**: 467–470.
- Yoffe, A. D. (1990). Electronic properties of low dimensional solids: The physics and chemistry of layer type transition metal dichalcogenides and their intercalate complexes, *Solid State Ionics* **39**: 1–7.
- Zahurak, S. M. and Murphy, D. W. (1987). A Method for Controlled Stoichiometry intercalation of Alkali Metals in Layered Metal Dichalcogenide crystal, *J. Sol. State Chem.* **70**: 137–140.
- Zhu, Xand Sun, Y., Zhang, S., Wang, J., Zou, L., Delong, L. E., Zhu, X., Luo, X., Wang, B., Li, Gand Yang, Z. and Song, W. (2009). Anisotropic intermediate coupling superconductivity in Cu_{0.03}TaS₂, *J. Less-Common Met.* **21**: 1–6.

Acknowledgements

Apart from the efforts of me, the success of any project depends largely on the encouragement and guidelines of many others. I take this opportunity to express my gratitude to the people who have been instrumental in the successful completion of this project. After Allah (SWT), I would like to show my greatest appreciation to my PhD supervisor Prof. dr. Sander van Smaalen. I can't say whether thanking him is enough for his tremendous support and help. I feel motivated and encouraged every time I discuss with him. Without his encouragement and guidance this project would not have materialized.

I wish to express my sincere thanks to Prof. dr. Bernd Harbrecht, department of Inorganic Chemistry, Philipps University, Marburg for his collaboration and allowance to work in his laboratory. I am grateful to Mr. Alfred Suttner, Dipl.Ing. (FH), Laboratory of Crystallography, University of Bayreuth, Bayreuth for his constant assistance during synthesis.

My sincere thanks are due to Dr. Swastik Mondal for giving me time whenever I required some suggestions and discussions in all aspect. He and his wife Ms. Aditi Dhar welcomed me in a homely environment from the first day. I am also thankful to PD Dr. Andreas Schönleber for his contribution to teach Aperiodic crystallography in his theoretical classes. I admire his willingness to pursue better research or so. A special thank goes to Dr. Christian Hübschle for his help to translate English summary into the Zusammenfassung of my PhD thesis.

The atmosphere in the team of the Laboratory of Crystallography is friendly and welcoming. Thanks to all who helped and supported me in daily life, technical issues, official issues: To name a few, Ms. Denise Kelk-Huth, Mr. Franz Fischer, Dr. Joachim Angelkort, Dr. Jeanette Held, Dr. Liang Li, Dr. Prathapa Siriya Jagannatha, Dr. Alexander Wölfel, Mr. Jian Zhang, Mr. Guoming Hao, Ms. Leila Noohinejad, Mr. Maxim Bykov, Mr. Somnath Dey, Ms. Wil Meijer.

Outside my group, I would like to thank some of the BGI group members namely, Mr. Detlef Krauß, Mr. Raphael Njul and Mr. Hubert Schulze for performing electron microprobe experiment of my sample. My special thank goes to Dr. Yamini Avadhut and Kedar kolharkar, who have helped me during the final stages of my PhD life in Bayreuth.

Of course, no acknowledgments would be complete without giving thanks to my parents. I am grateful to them for their patient encouragement throughout my career. Both of them have instilled many admirable qualities in me and have given me a good foundation to meet life as it comes. Maa (Mother), especially, is a great role model of resilience, strength and character to me. Special thanks to my little brother and sisters for their big support in all aspect, I wish my younger brother to finish his PhD study with dazzling brilliance.

Erklärung

Ich versichere hiermit eidesstattlich, dass ich diese Dissertation selbstständig und nur unter Verwendung angegebener Quellen und zulässiger Hilfsmittel erstellt habe. Ich habe bisher keine Promotionsversuche unternommen. Ich habe bisher weder die Hilfe von gewerblichen Promotionsberatern bzw. -vermittlern in Anspruch genommen, noch werde ich sie künftig in Anspruch nehmen.

Sk Imran Ali

Bayreuth, den 09.07.2014